## ALMA MATER STUDIORUM - UNIVERSITÀ DI BOLOGNA

---

**SCUOLA DI INGEGNERIA E ARCHITETTURA**

*DIN*

***CORSO DI LAUREA IN INGEGNERIA ENERGETICA***

**MASTER THESIS**

in

INGEGNERIA DEI SISTEMI SUPERCONDUTTIVI M

# LOSSES IN ELECTRODYNAMIC TRANSIENT IN SUPERCONDUCTING RUTHERFORD CABLES

*Author:*

Andrea Musso

*Supervisors:*:

Prof. Marco Breschi

Dr. Luca Bottura

Academic year 2015/2016

Session III

# *Sommario*

Il CERN (*Centro Europeo per la Ricerca Nucleare*) rappresenta il più grande laboratorio al mondo nel campo della fisica delle particelle. Nelle sue strutture si cerca di far luce sulle leggi fondamentali della natura tuttora inspiegate e di realizzare le dimostrazioni pratiche necessarie a validare le supposizioni teoriche.

Per esplorare le nuove frontiere della fisica delle alte energie si compiono esperimenti in condizioni particolarmente estreme, che necessitano di un livello tecnologico molto elevato [1]. Il cuore della tecnologia presente al CERN è costituito dalla catena di acceleratori di particelle che si conclude con LHC (*Large Hadron Collider*), il quale con i suoi 27 chilometri di circonferenza rappresenta il più grande e potente acceleratore di particelle del mondo, nonché una straordinaria opera scientifica, frutto del lavoro congiunto di scienziati ed ingegneri provenienti da oltre 60 paesi nel mondo. Scopo di questi dispositivi è l'accelerazione di fasci di particelle sino a velocità prossime a quelle della luce, da far collidere tra loro per analizzarne le interazioni e i prodotti delle collisioni. Per mantenere le particelle lungo la traiettoria circolare richiesta sono impiegati campi magnetici molto intensi, generati da elettromagneti.

Per motivi tecnici ed economici non sarebbe possibile utilizzare normali materiali conduttori per i cavi che costituiscono gli avvolgimenti. Vengono pertanto utilizzati materiali chiamati superconduttori, i quali se mantenuti entro certe condizioni d'esercizio si presentano in uno stato chiamato superconduttivo. In tale stato questi materiali esibiscono una resistenza elettrica praticamente nulla anche quando in essi viene fatta scorrere una grande corrente e sono pertanto ideali per applicazioni nel campo degli acceleratori di particelle. La superconduttività è pero uno stato che dipende dalle condizioni del sistema: al di sopra di certi limiti il materiale transisce allo stato normale perdendo le sue proprietà superconduttive. È indispensabile impedire la situazione per cui questa transizione diviene irreversibile e coinvolge tutto il magnete (fenomeno del *quench*) per evitare danni strutturali all'intera macchina. Questo richiede un'accurata stima a monte di tutti i termini di perturbazione dello stato di un magnete. Potendo prevedere le perdite a cui un magnete è soggetto, è possibile regolare i sistemi criogenici deputati al controllo e al ripristino delle condizioni operative del sistema.

Questa tesi illustra lo sviluppo e l'implementazione di un modello numerico per simulare nel dettaglio uno di questi meccanismi di perdita all'interno di cavi superconduttori per acceleratori di particelle (chiamati cavi *Rutherford*). Tale termine di disturbo è generato durante fenomeni transitori, come ad esempio un campo magnetico variabile nel tempo, che induce lo scorrimento di correnti (le cosiddette *interstrand coupling currents*) tra un filamento e l'altro (chiamati *strands*) di cui è costituito il cavo, richiudendosi nei punti di contatto tra di essi [2]. Tali correnti costituiscono una sorgente di perdite AC, oltre a limitare la densità di corrente massima sovrapponendosi alla corrente di trasporto e causare problemi di distorsione del campo magnetico.

Data la natura “a corto raggio” di queste correnti e la complessità della geometria di un cavo *Rutherford*, occorre che il modello descriva le caratteristiche dei singoli strand e dei loro contatti con un opportuno livello di dettaglio.
In letteratura sono presenti diversi modelli per calcolare la distribuzione delle *interstrand coupling currents* indotte all’interno di cavi superconduttori e delle perdite ad esse associate, la maggior parte dei quali mostra limiti riguardo il livello di precisione ottenibile o un eccessivo onere computazionale quando impiegati per simulare reali geometrie di cavi. In questa tesi vengono illustrati il modello a rete [3 - 6] e due approcci del modello continuo [7 - 10], spiegandone potenzialità e limiti. La trattazione si concentra quindi sul secondo approccio del modello continuo che permette di ottenere il livello di dettaglio necessario ai fini del calcolo delle perdite [10].

Questo nuovo approccio del modello è stato implementato attraverso il codice CryoSoft THEA [11] per simulare il comportamento elettrico di cavi con geometrie e condizioni di campo magnetico vari. Il cavo scelto come “caso base” per le simulazioni è un cavo in $Nb_3Sn$ usato nei nuovi magneti quadrupolari *MQXF* per il progetto *High-Luminosity* [12]; il modello viene quindi descritto e validato confrontando i risultati delle simulazioni con le formule analitiche per il calcolo delle perdite presenti in letteratura [13]. È inoltre effettuato uno studio di convergenza per le simulazioni.
Vengono presentati i risultati ottenuti in termini di distribuzione di corrente e di perdite per i singoli fili; alcune conclusioni sono tratte dalla variazione di parametri geometrici, elettrici e di campo magnetico dei cavi. Vengono discusse le scelte della lunghezza del cavo campione e delle condizioni al contorno usate per le simulazioni, in termini di correttezza nell'approssimazione di cavi di lunghezza reale.

Successivamente viene analizzata una delle principali strategie per ridurre le *interstrand coupling currents* e conseguentemente le perdite: l’introduzione di uno strato, chiamato *core*, di materiale ad elevata resistenza elettrica (in questo caso acciaio inossidabile), tra i due strati di *strands* che compongono il cavo [14-15]. Sono riportate le conseguenti modifiche al modello e le distribuzioni di corrente e perdite ottenute a seguito della sua introduzione nel cavo. Sono ricavate conclusioni riguardo la geometria, le proprietà elettriche e il posizionamento del core all’interno del cavo, al fine di ridurre il più possibile le perdite AC.

Il modello presentato può essere utilizzato per simulare la distribuzione delle correnti indotte e delle relative perdite in cavi *Rutherford* di ogni geometria e materiale, sottoposti ad un campo magnetico variabile nel tempo e può pertanto essere impiegato come strumento di previsione di perdite in cavi esistenti o per studi di progetto riguardo cavi futuri o in fase di studio con la possibilità di inserimento del core. Infine, il modello può essere facilmente accoppiato con il modello termo-idraulico già implementato in THEA, per un’analisi multifisica dei transitori elettrodinamici e termoidraulici sui cavi superconduttori per acceleratori di particelle.

# *Abstract*

CERN (*European Organization for Nuclear Research*) is the largest laboratory in the world in the field of particle physics. Among its facilities, scientists are trying to shed light on the fundamental laws of nature and to realize practical demonstrations necessary to validate the theoretical assumptions.

To explore the new frontiers of high-energy physics, experiments are performed in extreme conditions that require a very high level of technology to be maintained [1]. The heart of the scientific life at CERN is constituted by its chain of particle accelerators, that ends with the LHC (*Large Hadron Collider*) which with its 27 kilometres in circumference represents the largest and most powerful particle accelerator in the world, as well as an extraordinary technical work, result of the joint work of scientists and engineers from more than 60 countries worldwide. The purpose of these devices is the acceleration of particle beams approaching the speed of light, making them collide with each other in order to analyse the interactions and the products of these collisions. To keep particles inside the correct circular trajectory, magnetic fields with high intensity are used, generated by electromagnets.

For technical and economic reasons it is not possible to use normal conducting materials for the cables that constitute the windings. Therefore, different materials are adopted, called superconductors, which if maintained within certain operating conditions exhibit the superconducting state. In such condition, these materials offer virtually no electrical resistance when even a high current flows through them; thus, they are ideal for applications in the field of particle accelerators. However, superconductivity is a phenomenon that is based on system conditions: above certain limits, the material transits to the normal state losing its superconducting properties. It is essential to prevent the situation where this transition is irreversible and involves the whole magnet (phenomenon of *quench*) to avoid structural damage to the entire machine. This requires an accurate estimate upstream of all the disturbance terms of the state of a magnet. Being able to predict the losses to which a magnet is subjected, it is possible to optimize the cryogenic systems, responsible for control and restoring of the operating conditions.

This thesis illustrates the development and the implementation of a numerical model to simulate in detail one of these loss mechanisms within the superconducting cables (called *Rutherford* cables). Such disturbance term is generated during transients, such as in presence of a time-varying magnetic field, which induces currents (the so-called *interstrand coupling currents*) among different filaments (called *strands*) that constitute the cable, flowing through the strands contact points [2]. These currents represent a source of AC losses; besides, they superimpose to the transport current limiting the maximum current density of the cable and causing magnetic field distortion problems.

Given the "short-range nature" of these currents and the complexity of the geometry of a *Rutherford* cable, it is required that the model describes the characteristics of individual strand and the electrical parameters of each contact point with an appropriate level of detail. In literature, different models are proposed to calculate the distribution of *interstrand coupling currents* induced in superconducting cables and of the corresponding losses. However, they show limitations regarding the precision level achievable or an excessive computational burden when they are used to simulate cables with realistic geometries. A chapter of this thesis describes the network model [3 - 6] and two approaches of the continuum model [7 - 10], explaining their potential and limits. The discussion then focuses on the second approach of the continuum model that allows to get the necessary level of detail for the calculation of losses [10].

This new model approach is implemented through the *CryoSoft THEA* code [11] to simulate the electrical behaviour of cables with various geometries and magnetic field conditions. The cable chosen as baseline case study for the simulations is the $Nb_3Sn$ cable utilized in the new quadrupole magnets (*MQXF*) for the *High-Luminosity* project [12]. The model is then described and validated by comparing the simulation results with the analytical results obtained using formulae present in the literature for the calculation of losses [13]. Moreover, a convergence study is performed for simulations.
Results obtained are presented in terms of current and loss distribution; conclusions are deduced from the variation of geometric, electric and magnetic parameters of the cables. The choices of the sample length and the boundary conditions used for the simulations are discussed, in terms of accuracy in the approximation of real cable lengths.

Subsequently, it is analysed one of the main strategies to reduce *interstrand coupling currents* and consequently losses: the introduction of a strip, called *core*, a resistive strip of various width, thickness and material (stainless steel, in this case), inserted inside the Rutherford cable, which separates the top layer of strands from the lower [14-15]. The consequent modifications of the model and the current and loss distributions obtained as a result of its introduction into the cable are reported. Conclusions are drawn about the geometry, the electrical properties and the positioning of the core within the cable, in order to minimize the AC losses.

The model presented can be applied to simulate the distribution of induced currents and the corresponding losses in *Rutherford* cables of any geometry and material, subjected to a magnetic field variable in time, and it can thus be used as a predictive tool of losses in existing cables or for project studies regarding new developing cables with the possibility of insertion of a core. Finally, the model can be easily coupled with the thermo-hydraulic model, already implemented in THEA, for a multi-physic analysis of electrodynamic and thermo-hydraulic transient in superconducting cables for particle accelerators.

# *CONTENTS:*

## Chapter 1

# Superconductivity

## 1.1 The discovery

In 1908 at Leiden University laboratories (Netherlands), the physicist Heike Kamerlingh Onnes (awarded with Nobel Prize in 1913) was able to liquefy helium, the last of the inert gas to be condensed, reaching the temperature of 4.2 K: it was the lowest temperature value ever reached at that time [16]. Thanks to this milestone, a whole new field of experiments at temperatures previously unattainable was opening; Onnes himself began to study the behaviour of various materials in low-temperature conditions.

Then in 1911, three years after helium liquefaction, the scientist was "surprisingly" protagonist of the discovery of superconductivity. It was already noted that decreasing the temperature of any material, a lowered electrical resistance would have been achieved, but during the experiment "*something unexpected occurred"*. Onnes, cooling down mercury at temperature of liquid helium reported that: *"... as far as the accuracy of measurement went, the resistance of mercury disappeared. At the same time, however, the disappearance did not take place gradually, but abruptly. ... Thus the mercury at 4.2 K has entered a new state, which, owing to its particular electrical properties, can be called the state of superconductivity*" [17].

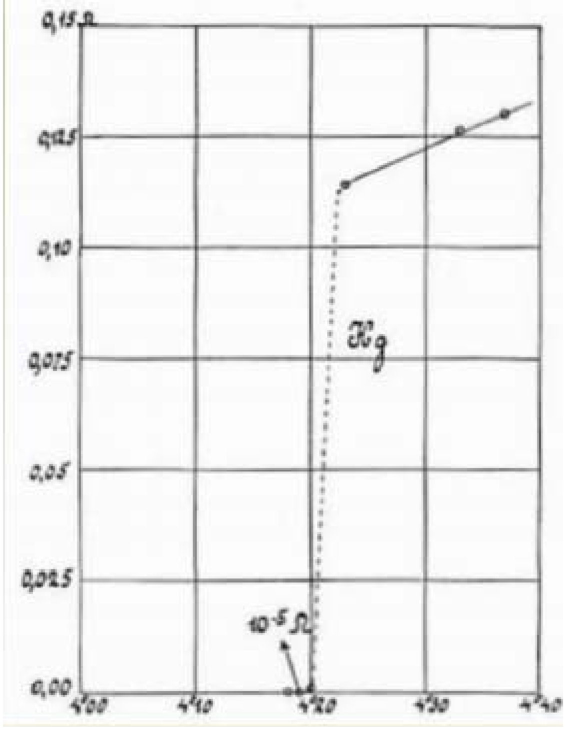

*Fig. 1. Behaviour of the electrical resistance of mercury as a function of the temperature, as directly reported by Onnes in 1911 [18].*

## 1.2 Properties

Nowadays it is known that the ideal superconducting state is a phenomenon exhibited by certain materials, called superconductors, which if kept within certain limits of temperature, magnetic field and current density show two main properties [19]:

### 1.2.1 Low Resistivity

The classical theory of electromagnetism explains that when the temperature of a material is reduced, its electrical resistance lowers due to the decrease of the vibration amplitude of the crystal lattice ions [20]. For a real conductor, resistance do not nullify completely in correspondence of the absolute zero (besides, a temperature never achieved in practice), but tends to a very small limit value, caused by the presence of defects in the crystal lattice. This relation is expressed by the following rule:

$$\rho = \rho_t + \rho_r$$

It is called Matthiessen's rule: the electrical resistivity of any material is formed by two components, $\rho_t$ and $\rho_r$. When temperature tends to absolute zero, thermal resistivity $\rho_t$ tends to nullify while resistivity $\rho_r$, which depends on the degree of purity of the crystal lattice, persists.

Instead, the characteristic curve of a superconductor resistivity is different: when these materials are cooled under a certain temperature $T_c$, called *critical temperature*, their resistivity falls sharply under detection limit, regardless of their degree of purity (Fig. 2).

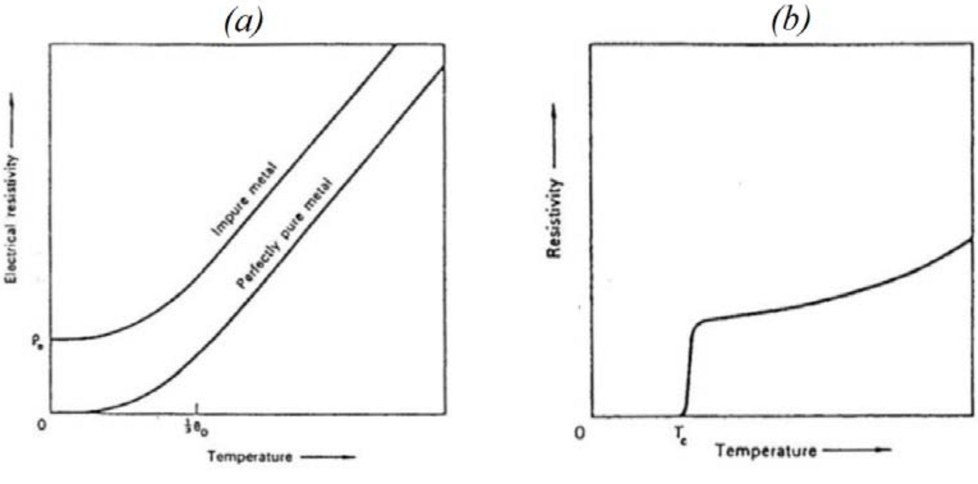

*Fig. 2. Characteristic curves of resistivity for real and ideal non-superconductors materials (a), and for superconductor materials (b) [20].*

This propriety alone is not sufficient to define a material as a superconductor because ideal normal conductors too, without defects in the crystal lattice, tend to have a null value of resistivity when their temperature tends asymptotically to absolute zero (see the lower curve in Fig. 2 (a) ). The macroscopic feature that distinguishes superconductors is their magnetic behaviour that differs from classical electromagnetism.

### 1.2.2 Meissner-Ochsenfeld effect

Superconductor materials exhibit a perfect diamagnetism, or rather the capability to eject an external applied magnetic field from its interior since such field do not exceed the critical value $B_c$ ; this property is called Meissner-Ochsenfeld effect named after the two researchers who first discovered the phenomenon.

This behaviour is due to the spontaneous formation of superficial super-currents (Fig. 3) which give rise to an internal magnetic induction field, equal and opposite to the one applied from the outside.

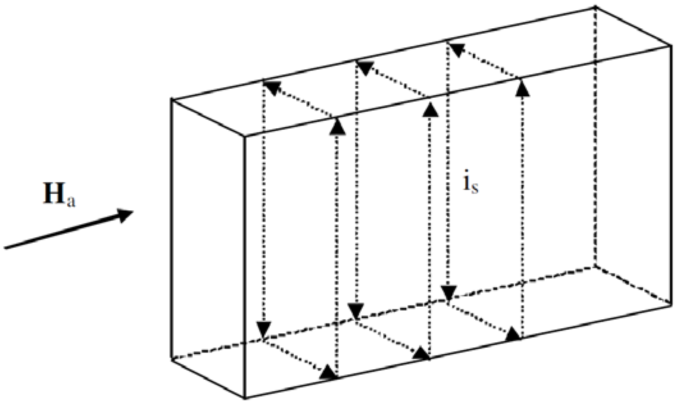

*Fig. 3. Supercurrents due to an external induction field $H_a$ [20].*

In real terms, there is a small portion of conductor within which the magnetic field can penetrate. Given that the super-currents cannot flow on a perfectly two-dimensional plane they penetrate to a certain depth in the superconducting material, called depth of penetration λ, within which the field is attenuated exponentially to zero starting from the material surface, as it is possible to understand from Fig. 4.

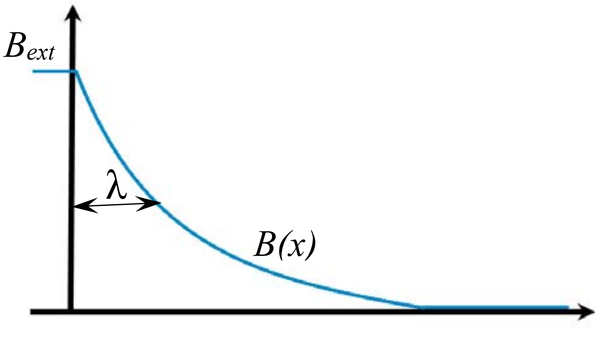

*Fig. 4. Penetration of a magnetic field inside a material [20].*

Even an ideal conductor cooled at a temperature at which $\rho = 0$, and subsequently immersed in a stationary magnetic field is able to expel this field from its interior; however, they do not show such property if this sequence of events is not respected. In fact, if the external magnetic field is applied before cooling under $T_c$, the induced vector $B$ remains constant and different from zero even after the removal of the external field [20]. Instead, for a superconducting material the magnetization state is independent of the external conditions and therefore it does not depend on the moment at which the external field is applied. See Fig. 5 for an explanation of the sequence of events.

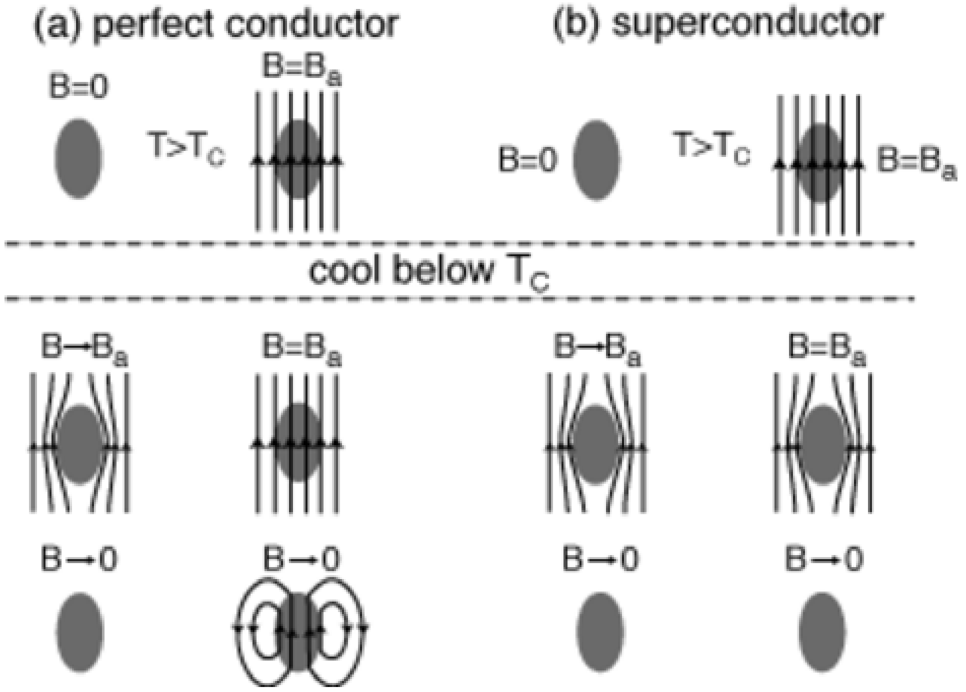

*Fig. 5. Behaviour of a perfect conductor material (a) and of a superconducting material (b). In each case, pictures on the left describe the application of an external field after cooling, while pictures on the right describe the application of the same field before cooling (Copyryight Philip Hofmann, 2009/03/12).*

## 1.3 Critical surface

In order to exhibit and maintain the superconducting state, superconductor conditions must be within defined limits of temperature, magnetic field and current density ($T_c$, $B_c$ and $J_c$ respectively). Temperature and critical magnetic field are intrinsic characteristics of the material, while the current density depends on the thermo-mechanical treatments to which it was subjected: these three quantities are closely related.

Once a material is chosen and the history of its treatments is known, it is possible to obtain the so-called *critical surface* which defines the transition from the superconducting state to the normal state: when even only one of the three conditions is not fulfilled and the operating point exits the 3-D curve the material loses its properties and transits to the normal state (see Fig. 6).

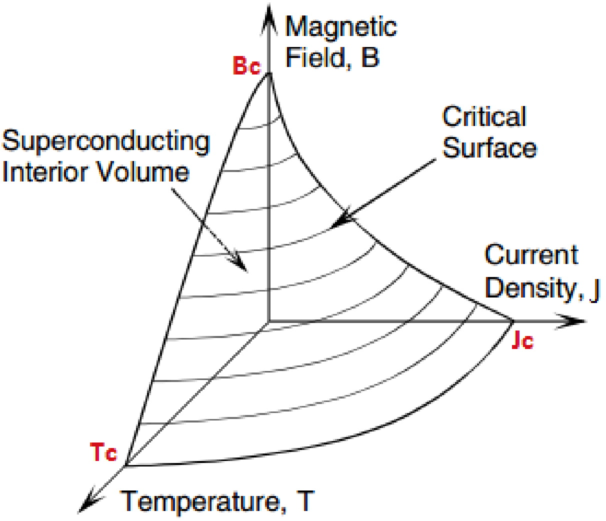

*Fig. 6. General representation of a critical surface [19].*

## *1.4 Type I and Type II superconductors*

Superconductors can be distinguished into two classes based on their response to a magnetic field (see Fig. 7 for a classification of the superconducting elements on the periodic table):

I. Superconductors of Type I:

These materials perfectly reflect the superconducting properties that have described so far. Many elements and some metal alloys belong to this type of superconductors.

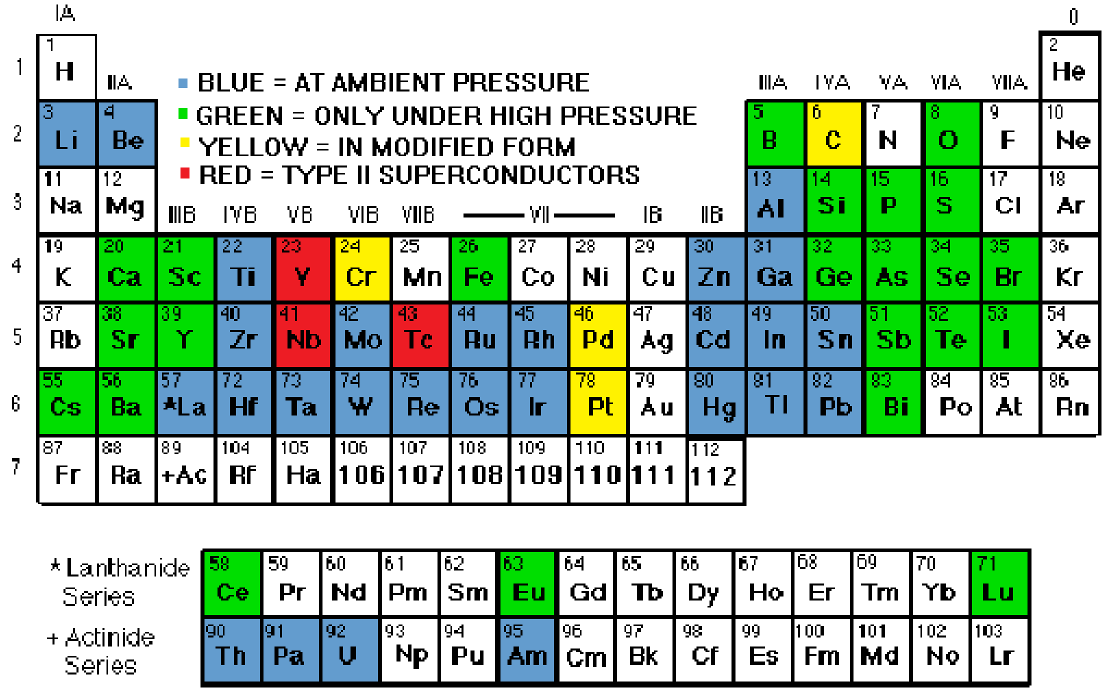

🟦 BLUE = AT AMBIENT PRESSURE
🟩 GREEN = ONLY UNDER HIGH PRESSURE
🟨 YELLOW = IN MODIFIED FORM
🟥 RED = TYPE II SUPERCONDUCTORS

| | IA | IIA | IIIB | IVB | VB | VIB | VIIB | VII | VII | VII | IB | IIB | IIIA | IVA | VA | VIA | VIIA | 0 |
|---|---|---|---|---|---|---|---|---|---|---|---|---|---|---|---|---|---|---|
| 1 | 1 H | | | | | | | | | | | | | | | | | 2 He |
| 2 | 🟦 3 Li | 🟦 4 Be | | | | | | | | | | | 🟩 5 B | 🟨 6 C | 7 N | 🟩 8 O | 9 F | 10 Ne |
| 3 | 11 Na | 12 Mg | | | | | | | | | | | 🟦 13 Al | 🟩 14 Si | 🟩 15 P | 🟩 16 S | 17 Cl | 18 Ar |
| 4 | 19 K | 🟩 20 Ca | 🟩 21 Sc | 🟦 22 Ti | 🟥 23 V | 🟨 24 Cr | 25 Mn | 🟩 26 Fe | 27 Co | 28 Ni | 29 Cu | 🟦 30 Zn | 🟦 31 Ga | 🟩 32 Ge | 🟩 33 As | 🟩 34 Se | 🟩 35 Br | 36 Kr |
| 5 | 37 Rb | 🟩 38 Sr | 🟩 39 Y | 🟦 40 Zr | 🟥 41 Nb | 🟦 42 Mo | 🟥 43 Tc | 🟦 44 Ru | 🟦 45 Rh | 🟨 46 Pd | 47 Ag | 🟦 48 Cd | 🟦 49 In | 🟦 50 Sn | 🟩 51 Sb | 🟩 52 Te | 🟩 53 I | 54 Xe |
| 6 | 🟩 55 Cs | 🟩 56 Ba | 🟦 57 *La | 🟦 72 Hf | 🟦 73 Ta | 🟦 74 W | 🟦 75 Re | 🟦 76 Os | 🟦 77 Ir | 🟨 78 Pt | 79 Au | 🟦 80 Hg | 🟦 81 Tl | 🟦 82 Pb | 🟩 83 Bi | 84 Po | 85 At | 86 Rn |
| 7 | 87 Fr | 88 Ra | 89 +Ac | 104 Rf | 105 Ha | 106 106 | 107 107 | 108 108 | 109 109 | 110 110 | 111 111 | 112 112 | | | | | | |

| | | | | | | | | | | | | | | |
|---|---|---|---|---|---|---|---|---|---|---|---|---|---|---|
| * Lanthanide Series | 🟩 58 Ce | 59 Pr | 60 Nd | 61 Pm | 62 Sm | 🟩 63 Eu | 64 Gd | 65 Tb | 66 Dy | 67 Ho | 68 Er | 69 Tm | 70 Yb | 🟩 71 Lu |
| + Actinide Series | 🟦 90 Th | 🟦 91 Pa | 🟦 92 U | 93 Np | 94 Pu | 🟦 95 Am | 96 Cm | 97 Bk | 98 Cf | 99 Es | 100 Fm | 101 Md | 102 No | 103 Lr |

*Fig. 7. Elements of the periodic table that can reach the superconducting state under certain conditions; red elements are Type II, all others are Type I [21].*

They present the following limits:

- Their $T_c$ is very low;

- Their penetration depth is small (from 20 to 50 nm); this means they can curry very small current density since the current is restricted to a thin surface layer (current density is the electric current per unit area of cross-section);

- Their critical field $B_c$ is low (dozens of mT).

It is easy to understand why it is not convenient to adopt these materials in high-field magnetic systems such as in particle accelerators systems: their use would require too expensive cryogenic systems and in any case they still would not be able to handle the extremely high magnetic fields and current densities involved, without having a sharply transition to the normal state.

### I. Superconductors of Type II:

A variety of alloy and compounds are Type II superconductors, they are characterized by a different magnetic behaviour depending on field conditions:

- For magnetic fields lower than $B_c$, these materials exhibit all properties of superconductors of Type I: they are in the so-called *Meissner state* (Fig. 8 (a)). However, their $B_c$ value is limited and for most of their usages they do not work in this area;

- For magnetic fields between fields $B_{c1}$ (lower critical field) and $B_{c2}$ (upper critical field) these materials are in the so-called *mixed state* (Fig. 8 (b)). In this state, the material as a whole is no longer perfectly diamagnetic and the magnetic flux begins to penetrate inside the material in regions of space that transit to the normal state (called *fluxoids*): in these conditions the superconducting state and normal state coexist [20].

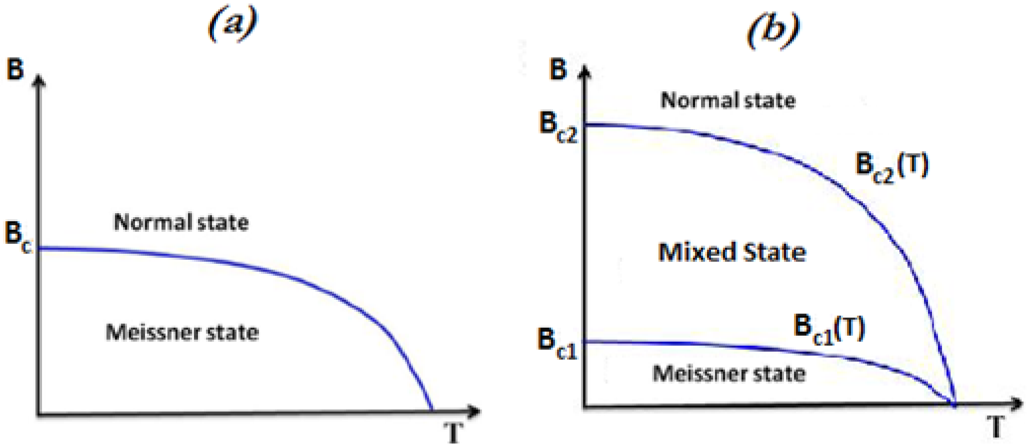

*Fig. 8. Magnetic behaviour of superconductors of Type I (a) and Type II (b). The scale does not represent the real differences between magnetic fields $B_c$, $B_{c1}$ e $B_{c2}$ [20].*

The separation between these two zones takes place due to the spontaneous formation of super-currents, which cause a decay of the field from its maximum value at the center of fluxoid to a zero value in a radius equal to the penetration depth starting to its center. Given that the most part of the material remains in the superconducting state, the material can globally preserve its property of null resistivity even if the field exceeds the field $B_{c1}$ (Fig. 9).

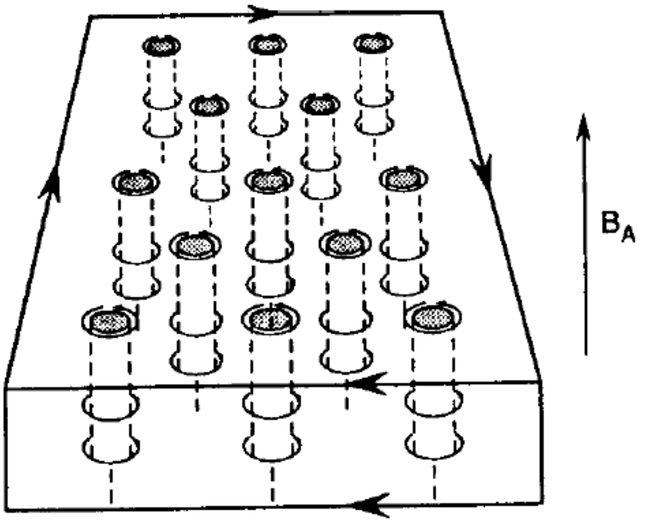

*Fig. 9. Schematic representation of fluxoids and super-currents generated by a transverse magnetic field, which penetrates a type II superconducting material* [22].

Increasing the external magnetic field, the number of fluxoids increases: once the upper critical magnetic field is reached, the material is completely saturated by the field lines that cross it and it can no longer be considered a superconductor.
The value of the upper field $B_{c2}$ may reach tens of Tesla, allowing type II superconductors to be used in the high-field applications.

## *1.5 Evolution of Superconductors*

Since Onnes discovery in 1911, superconductivity has become a fertile ground for researches by the scientific community, which has put great effort driven by the enormous potentials that this phenomenon presents. In recent years, 13 scientists have earned the Nobel Prize for their discoveries in this field.

Regarding to the study of materials, in subsequent decades other superconducting metals, alloys and compounds were discovered with higher and higher performances. Particularly in magnets field, it was crucial the discovery of peculiar Type II superconductor material that can handle great fields and current densities and transit at $T_c$ high enough to reduce costs and logistical problems.

In 1961, John E. Kunzler identifies a group of superconducting compounds and alloys capable of carrying extremely high currents ($10^6$ A/cm$^2$) at high-intensity fields (30 T)

[20]; in 1962, scientists at Westinghouse developed the first commercial superconducting wire, an alloy of niobium and titanium (NbTi), thus starting the studies for superconducting cables for magnets.

NbTi is the first and most used superconducting cable in actual particle accelerators (LHC included); NbTi and $Nb_3Sn$ constitute basically the only two materials that are commercially available for large scale magnet production nowadays. See Fig. 10 for a comparison of their critical surfaces.

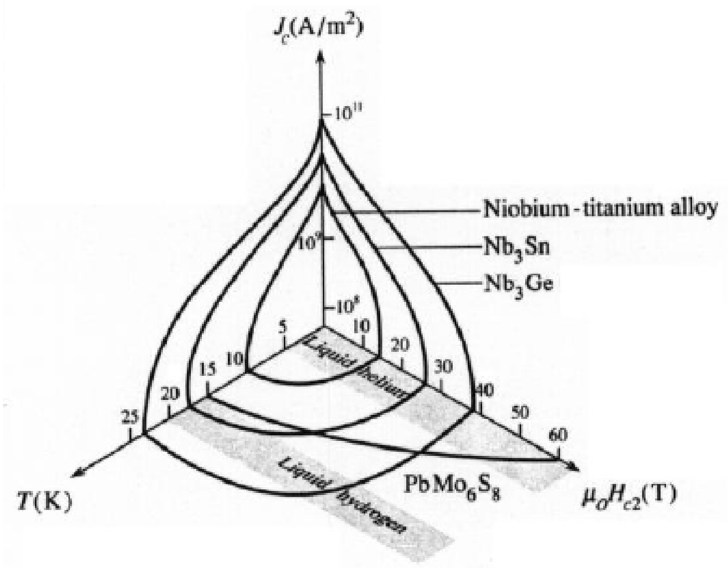

*Fig. 10. Comparison between the critical surface of NbTi and $Nb_3Sn$ [20].*

NbTi is primarily adopted for its ductility, which allows fabricating it in easier methods: the technique is called "*powder in tube*" with a synthesis that can be done "*ex situ*". At temperature of 4.2 K (liquid helium) its upper critical magnetic field reaches "only" 10 T; cooling with superfluid helium at 2 K increases the field level to about 9 T, as needed in the LHC [23].

$Nb_3Sn$ can reach upper critical fields of about 20 T at 4.2 K; this makes it interesting for developping applications at higher fields. $Nb_3Sn$ performance as a function of the magnetic field are superior compared to NbTi, but there are also some drawbacks. Because of its brittleness, it is not possible to wrap $Nb_3Sn$ wires in coils after they are transited to the superconducting state, in fact, their performance degrades significantly with the mechanical deformation showing an important reduction of their current-carrying capacity. This means that producing a $Nb_3Sn$ coil requires special techniques, such as "*wind and react*" technique: that impose to all the magnet in its final form to undergo to the thermal processes needed, requiring the utilization of large dimensions furnaces and subjecting all magnet components (supports, insulations etc.) to elevate temperatures for times of hours scale [20].

Then in 1986, Georg Bednorz and Alex Müller obtained the transition of ceramic materials (the family called *cuprates*) to the superconducting state at temperatures greater than 30 K, pioneering to a new class of superconductors called HTS (High Temperature

Superconductors). Over the years, new HTS materials have been developed, where the most promising are YBCO and BSCCO families, with $T_c$ that can exceed 100 K. See Fig. 11 for a brief evolution of the materials.

These materials can significantly reduce the cost of the cooling system as they can be maintained in the superconducting state without requiring the use of liquid helium or liquid nitrogen, but using liquid hydrogen, which is much less expensive and easier to retrieve. Notwithstanding this, the applicability of such materials remains limited by their cost due to complex manufacturing. By the way, in 2001 it was found the superconducting state of $Mg_2B_2$, which has a $T_c$ of 39 K: it has properties of HTS materials but it has a simple and consolidated method of production.

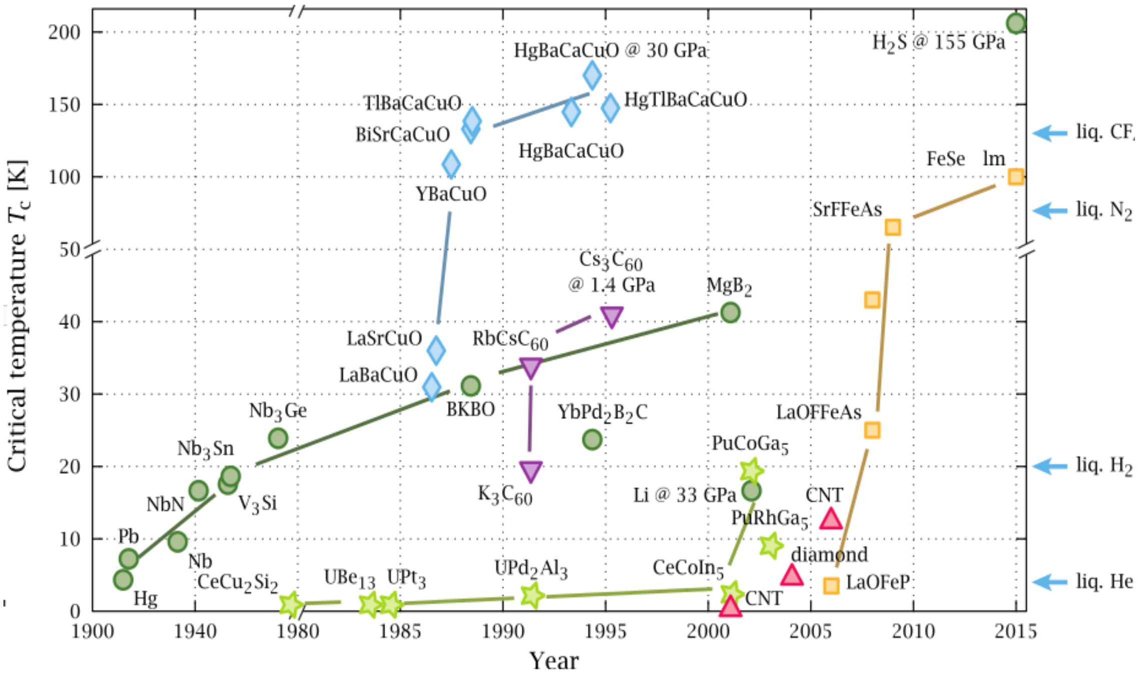

*Fig. 11. Evolution through the years of the superconducting materials based on their critical temperature. Colours indicate the superconductor families [23].*

## *Chapter 2*

# *CERN*

CERN, French acronym for "*Conseil européen pour la recherche nucléaire*" is an international organization, which manages the world's largest laboratory for studies on particle physics.

The laboratory is located in the northwest area of Geneva on the Franco–Swiss border (Fig. 12).

*Fig. 12. Aerial view of the CERN area [23].*

The agreement among the first 12 member states for the establishment of this organization dates back to September 29, 1954; from this date, the collaboration network has expanded from year to year: today the community counts 22 member states to which must be added several "*observer states*" from outside Europe. Being a reference point for physics research, CERN also cooperates with a large amount of states around the world.

Many discoveries took place here, the most recently celebrated are the detection of the Higgs boson and discoveries on penta-quarks; numerous awards are won by scientists who conducted experiments here and/or have deduced their theories.

## 2.1 CERN studies

The heart of the laboratory is constituted by its particle accelerators: the primary purpose of these devices is to investigate many aspects of particle physics; without such means it would be impossible to reproduce certain events in the laboratory and analyse them with an appropriate level of accuracy.

One of the most ample and important investigation concerns the validation of the so-called "*Standard Model*": the physical theory through which it is possible to describe all the elementary particles of matter and the forces that govern their interactions allowing to understand the fundamental laws that regulate nature; this theoretical model needs experimental verification to validate its predictions. These validations can be carried out only in extreme and strictly controlled conditions, for example, reaching very high levels of kinetic energy of particles, involving high magnetic fields (and thus equally large currents) and working at very low temperatures.

Particle accelerators are fundamental tools to achieve such conditions: they accelerate beams of ions or subatomic particles until they reach the higher possible speed (or accordingly, energy); once the required energies are attained, these beams are collided with each other or with a fixed target.

When two particles having high speed collide with each other a new particle is obtained as a product, which for the well-known law that link mass and energy, $E = mc^2$, will have an energy, and therefore a mass, greater than the energy of the two particles that generated it. Then, this new particle can decay, giving rise to other particles in precise *radioactive cascades*; usually because of the rapidity of such decays it is not possible to detect directly the "*parent particle*", but it is possible to extrapolate its properties from the analysis of the "*daughter particles*" characteristics. Studying these interactions, theoretical physicists get material to be able to draw important conclusions.

## 2.2 From larger to smaller

### 2.2.1 The acceleration chain

When people thinks about devices to accelerate particles used at CERN, the most mentioned it is definitely the LHC (*Large Hadron Collider*), which with its 27 kilometres in circumference is the largest accelerator in the world. However, this is not the only particle accelerator at CERN and it represents "only" the last stage of the "*acceleration chain*" that the particles carry out during their life in the laboratory.

The idea is to use accelerators in sequence: a particle beam is initially accelerated in less powerful accelerators and then it is transferred towards ever more powerful accelerators, where it undergoes a gradual increase of energy; the maximum speed, near to the speed of light, are reached at the last stage of this chain: the LHC.

The operations that take place inside an accelerator can be divided into three phases [24]:

- *Injection:* during which the beam of particle is prepared by the various pre-accelerators and injected into the first accelerator of the chain;

- *Acceleration:* during which the beam is accelerated to the nominal energy of the accelerator;

- *Sending or Storage:* during which the beam is sent to the next accelerator in the chain or, if it has already been reached the maximum energy required for that specific experiment, this level of energy is maintained for as long as possible and it is made available for physics experiments.

Particle accelerators can be classified according to various principles, one of these is based on their shape from which it depends the number of times that the same particle beam cross it. In linear accelerators particles pass through it only one-time from input to output (they constitute the first stages of the acceleration chain), while in circular accelerators a particle beam travels repeatedly around its loops in order to achieve higher energies.

CERN accelerator system comprises 7 major accelerators to which several experiments are connected [25] (Fig. 13):

- Two linear accelerators that are at the beginning of the acceleration chain:

  LINAC2: it accelerates protons up to energy of 50 MeV;

  LINAC3: it generates heavy ions (usually lead) to 4.2 MeV/nucleon;

- LEIR (Low Energy Ion Ring): circular accelerator where heavy ions produced by LINAC 3 arrive and are then accelerated up to 72 MeV;

- PSB (Proton Synchrotron Booster): circular accelerator consisting of 4 overlapping synchrotrons with a circumference of 50 meters; it accelerates the protons coming from LINAC2 to energy up to 1.4 GeV. It is also used in separate experiments such as ISOLDE;

- PS (Proton Synchrotron): circular accelerator having a circumference of 628.3 meters, it accelerates protons up to 28 GeV; is the most "ancient" accelerator still in operation at CERN;

- SPS (Super Proton Synchrotron): circular accelerator with a 2 km diameter which accelerates protons up to 450 GeV;

- LHC (Large Hadron Collider): circular accelerator having a circumference of 27 km; it accelerates protons up to 6.5 TeV (higher value ever achieved by an accelerator:

record obtained in May 2015). For the work presented in this thesis, references will be done to cables used for this accelerator.

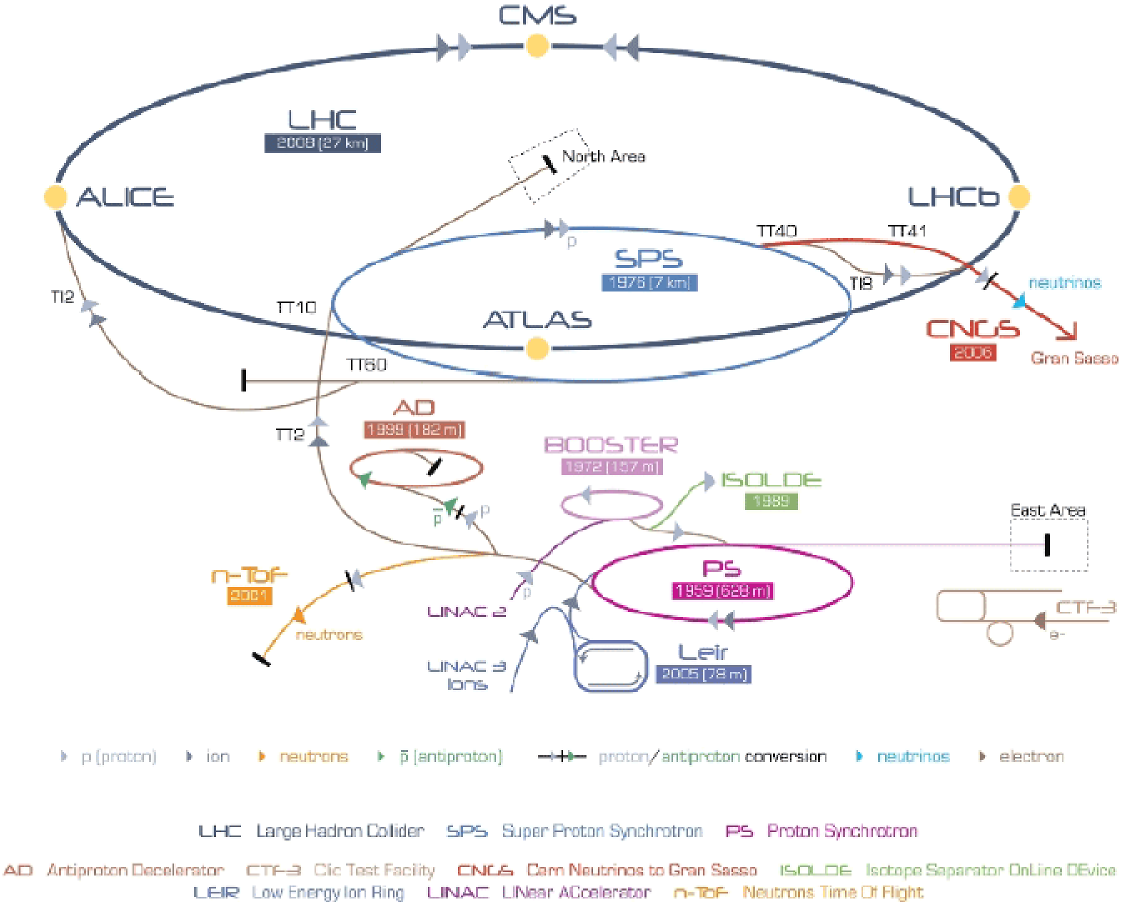

*Fig. 13 CERN accelerators system and experiments [25].*

The achievement of the highest energies possible is not the principle aim of the acceleration chain. In fact, it can be considered a necessary preparatory step for the following studies (whose quality, however, depends on the acceleration performance), which constitute the “real scope” of the experiment: analyse events of collision between two particle beams traveling in opposite directions and most of all investigate about new particles that result from such impacts. The revelation of particles produced by the impact between beams is a complex and delicate operation as much as that which allows their acceleration.

In LHC two particle beams are made to collide in four points on the accelerator circumference, corresponding to the four main experiments of its scientific program: ATLAS, CMS, LHCb and ALICE (see Fig. 13). Fulcrum of such experiments are huge particle detectors that allow to obtain a great number of information regarding these collision phenomena.

### *2.2.2 LHC*

In this thesis will be only presented a brief description on the structure of LHC, avoiding details of many components that make up its 27 km length. It will be sufficient to understand its fundamental elements, that allow reaching and maintaining unique conditions in the world.

In LHC, two particle beams are driven from the input speed (at which they arrive from the previous sections of the acceleration chain) up to speed close to the speed of light: the nominal speed is equal to 99.9999991% of its value. At the same time it is crucial that these beams remain confined within the magnet cavities and maintain unaltered their orbit.

To modify the speed ($v$) and the trajectory of particles (with charge $q$) electromagnetic fields are used ($E$, $B$): they generate a Lorentz force on charges that can be expressed through this formula:

$$F = q\,(E + v \times B)$$

A particle undergoes an acceleration in its motion direction due to the electric field $E$, while the magnetic field $B$, perpendicular to the velocity vector $v$, does not vary the kinetic energy of the particle but it is adopted to change its trajectory.

Therefore, it is possible to distinguish two main elements in LHC [25]:

I. Radiofrequency (RF) cavities: through an alternating electrical potential, particles increase their kinetic energy whenever they pass through these elements. It is necessary that the frequency of potential variation is exactly synchronized with the passage of the bunch of particles at every turn, in order to achieve the desired effect (the so-called "kick"). This requires an extremely high level of precision, since the particles pass through each cavity 11245 times per second. In Fig. 14 a model of their structure is shown;

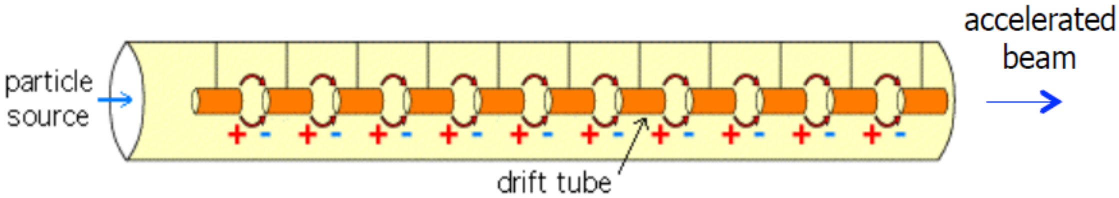

*Fig. 14. Schematic representation of a radiofrequency cavity [20].*

II. Magnets: the 1600 superconducting magnets of LHC can be further divided between:

- Dipole Magnets (MB): they generate the magnetic field necessary to keep the two particle beams traveling in opposite directions in their proper trajectories.
- Quadrupole Magnets (MQ): they generate the magnetic field necessary to focus the particles: beams are composed by electrically charged particles (protons) that naturally tend to diverge from their selves. A single quadrupole is able to focus the beam in just one direction ($x$ or $y$), defocusing the beam in the other direction at the

same time: in order to get the correct result it is indispensable to couple two quadrupoles which act in directions perpendicular to each other.

- Corrector Magnets: many other high order magnets are placed along the ring to correct the magnetic field errors of the larger main magnets [24].

LHC magnets are organized in 23 regular cells that are repeated along the length of the accelerator (described in Fig. 15), the so-called "*FODO cell*s".

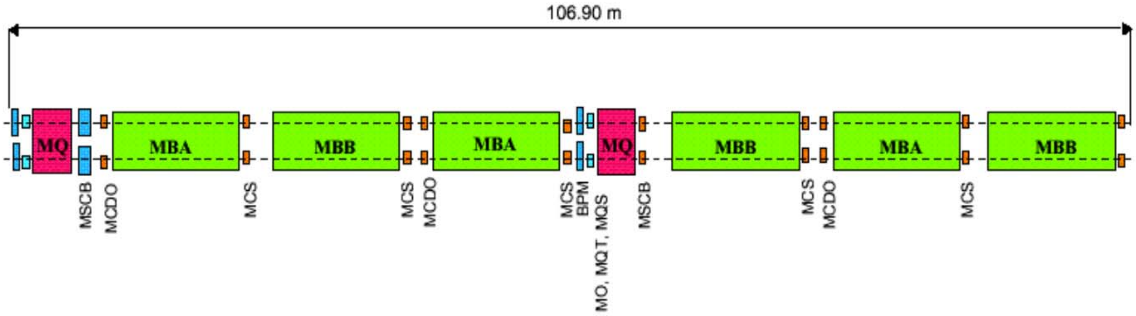

*Fig. 15 A schematic layout of a FODO cell (F and D letters are for Focalization in one direction and De-focalization in the other, while O is a space or a deflection magnet): MB are main dipole magnets while MQ are main quadrupoles, the other terms are for corrector magnets [26].*

Actual LHC dipoles produce a field equal to 8.3 T, while new high-field magnets that will be soon installed will reach 11-13 T. Note that to reach the actual 8.3 T magnetic fields, a current of 11850 A in the magnet coils is needed. At the same time, studies for even more powerful magnets are carried out. In Table 1 a summary of LHC MB parameters is displayed.

| Parameter | unit | value |
|---|---|---|
| Magnetic length | $m$ | 14.3 |
| Operating temperature | $K$ | 1.9 |
| Current at injection (0.45 $TeV$) | $A$ | 739 |
| Bending radius | $m$ | 2803.928 |
| Number of beams per magnet | | 2 |
| Nominal current | $A$ | 11850 |
| Bending angle per magnet | $mrad$ | 5.1000 |
| Peak field in coil | $T$ | 8.76 |
| Field at injection | $T$ | 0.535 |
| Field @7 TeV | $T$ | 8.33 |
| Inductance per magnet | $H$ | 0.108 |
| Mass of cold mass | $t$ | 23.8 |

*Table 1. Summary of LHC MB main parameters [1].*

It was mentioned the fact that particles "life" within an accelerator needs to proceed in extremely controlled conditions and it is therefore mandatory to minimize all disturbance phenomena for detectors. For example, to avoid that particles collides with other gas molecules present in the pipe, thus deviating from their predetermined trajectory, beams flows within a "beam pipe" which is maintained in ultrahigh vacuum conditions. Furthermore, the entire collider and its experiments are placed inside a tunnel at a depth ranging from 50 to 175 meters: this configuration avail to increase the shielding against cosmic radiation that can interact with the particles and alter the experimental results.

### *2.2.2.1 Why Superconductors?*

Having a picture of the quantities involved, is easy to understand why superconductivity has been the most influential technology in the field of accelerators in the last 30 years, preferring these materials than ordinary wires, although the latter have a smaller cost for meter. To get the same results obtained for LHC using ordinary wires, it should require:

- The use of much more normal material.
- The construction of wider and longer tunnels (if normal magnets were used instead of superconducting magnets, the final accelerator would have to be 120 km long to reach the same energy level of LHC) thus having a higher capital cost.
- The installation of a greater power (900 MW of power installed would be needed, equal to the power output of a large nuclear power plant).
- Cope with the huge amount of losses and the removal of the heat produced by Joule effect (normal conductors have higher electrical resistance than superconductors).

Consequently, without superconductivity it would not be possible to operate LHC.

### *2.2.2.2 LHC upgrade projects*

#### *High-Luminosity LHC*

It is possible to increase performances of an accelerator not only increasing the kinetic energy of particles, but acting on different parameters; luminosity, for example, is extremely important.

Luminosity represents the number of collisions per cross-section, occurring in the unit of time. As in the case of LHC, where collisions happens between particle beams splitted into different bunch of particles, the luminosity is given by:

$$L = \frac{N_1 \cdot N_2}{A} f$$

Where $N_1$ e $N_2$ are the number of particles present in the colliding bunches, $A$ is the average cross-section of the beams and $f$ is the frequency with which two bunches collide.

Some of the events that the LHC detectors investigate occur in such a small number during operation, that even long investigation times may not be sufficient to obtain a significant sample of data that can be used as a statistical base for deducing any conclusion.

By increasing the luminosity, it is possible to extend the number of such rare events that are inaccessible at the LHC's current sensitivity level. For example, after the High-Luminosity implementation, LHC will be able to produce up to 15 million Higgs bosons per year, compared to the 1.2 million produced in 2011 and 2012.

High-Luminosity LHC project aims to increase tenfold the actual luminosity value (bringing it from the value of $10^{34}$ $\text{cm}^{-2}\text{s}^{-1}$ to the value of $10^{35}$ $\text{cm}^{-2}\text{s}^{-1}$) for observations that will start after 2025.

To perform this upgrade, changes on LHC are planned for the next future; some of them require the overcome of considerable technological step and thus the development of innovative technologies for which many efforts and resources are currently spent.

A very important modification involves the replacement of some magnets with a new magnetic system, actually in development. For High-Luminosity LHC project it is necessary the inclusion of additional collimators in the accelerator; that on the other hand, introduce the problem about how to find the space to add new elements within the LHC ring that is already full [25]. To overcome this issue, some of actual dipoles will be replaced with shorter but more powerful magnets, which will be able to reach a magnetic field of 11 T instead of the current 8.3 T [27]. At the same time, 16 new quadrupoles (called *MQXF*) will be installed in the proximity of the two main experiments to produce magnetic fields greater than the current ones (about 12 T) in order to provide the final beam focusing. It would not be possible to obtain these results using NbTi coils actually in use, therefore it will be necessary to use $Nb_3Sn$ for coils, a superconducting material with higher performance; that material, however, requires the solution of other technological problems, as already introduced in Chapter 1.5.

### *Very Large Hadron Collider*

Why is the size of an accelerator so important? Particles traveling within the accelerator with high energies require a high magnetic field in order to be bended and confined inside the beam pipe; without its effect, particles could bump the accelerator walls and would be lost. As seen for the High-Luminosity project, modifications are performed to increase the magnetic field produced by LHC magnets, however, at the current state of the art it is not feasible to go beyond certain field values. This problem can be solved by increasing the size of the circular accelerator, following this simple rule:

$$\rho\ [\text{m}] = \frac{E\ [\text{GeV}]}{0.3\ q \cdot B\ [\text{T}]}$$

Where $\rho$ is the radius of curvature that a magnetic field $B$ applies on a particle having charge $q$ and an energy $E$. Once the nature of particles is set (fixing $q$), it is possible to

bend particles of greater energy by increasing the radius (and thus the size) of the accelerator without necessarily increasing its magnetic field.
Hence, in the last years a project has been proposed about the design and build of a new particle accelerator of around 100 km in circumference (*VLHC: Very Large Hadron Collider*) that exceeds the capabilities of LHC. This project is still under discussion and there is no detailed plan or schedule for the *VLHC* for the moment.

## *2.2.3 Magnets*

Going deeper inside LHC, it is useful to outline the design of the magnets in order to understand in more detail the technological context in which superconductivity is used.

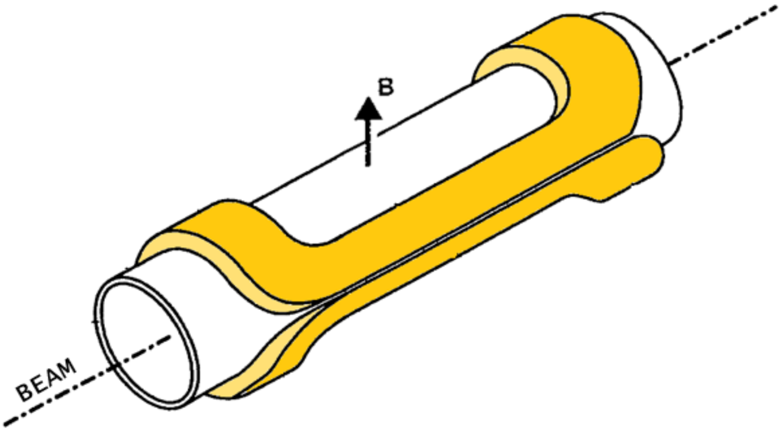

*Fig. 16. Racetrack configuration for a dipole magnet*

The superconducting magnets tasks are the bending (dipoles) and the focusing (quadrupoles) of particle beams during their path; note that a magnetic field is able to provide an adequate force only if it is perpendicular to the particle trajectory. To achieve this result, a coil realized with highly compacted superconducting cables, in a characteristic shape called *racetrack,* is arranged around the beam pipe in which particles flow (Fig. 16). In fact, the magnetic field in a superconducting accelerator magnet is mainly produced by the current in the conductors, rather than the magnetization of an iron yoke [28].

Looking at the section of a magnet as in Fig. 17 (in the case of a dipole, but equivalent can be found into a quadrupole), it is possible to describe the main magnet components.

Very schematically, the two beams that travel into the accelerator in clockwise and counterclockwise directions are contained within the same magnet into separated *beam pipes* in ultrahigh vacuum conditions. Tightly packed superconducting cables are wrapped around pipes to produce the magnetic field. *Austenitic steel collars* hold the coils in place against the strong magnetic forces that arise when the coils are at full field (the Lorentz forces produced in 1 meter of dipole corresponds at about 400 tons); then an *iron yoke* sorrounds this assembly closing the magnetic field lines. Electrical bus connection called *bus-bars* provide the transfer of current between different magnets. Thus, the structure is inserted into a complex *cryostatic system*: thermal shields and vacuum help to minimize convection and radiation exchanges and, most important, all the system is crossed by superfluid liquid helium at temperature of 1.9 K, which dissipates the input heat by means of heat exchanger tubes, providing cooling to the temperature required for superconductivity. Finally, *supports* sustain the weight of the magnet: a dipole of a length of 15 meters weighs about 35 tons.

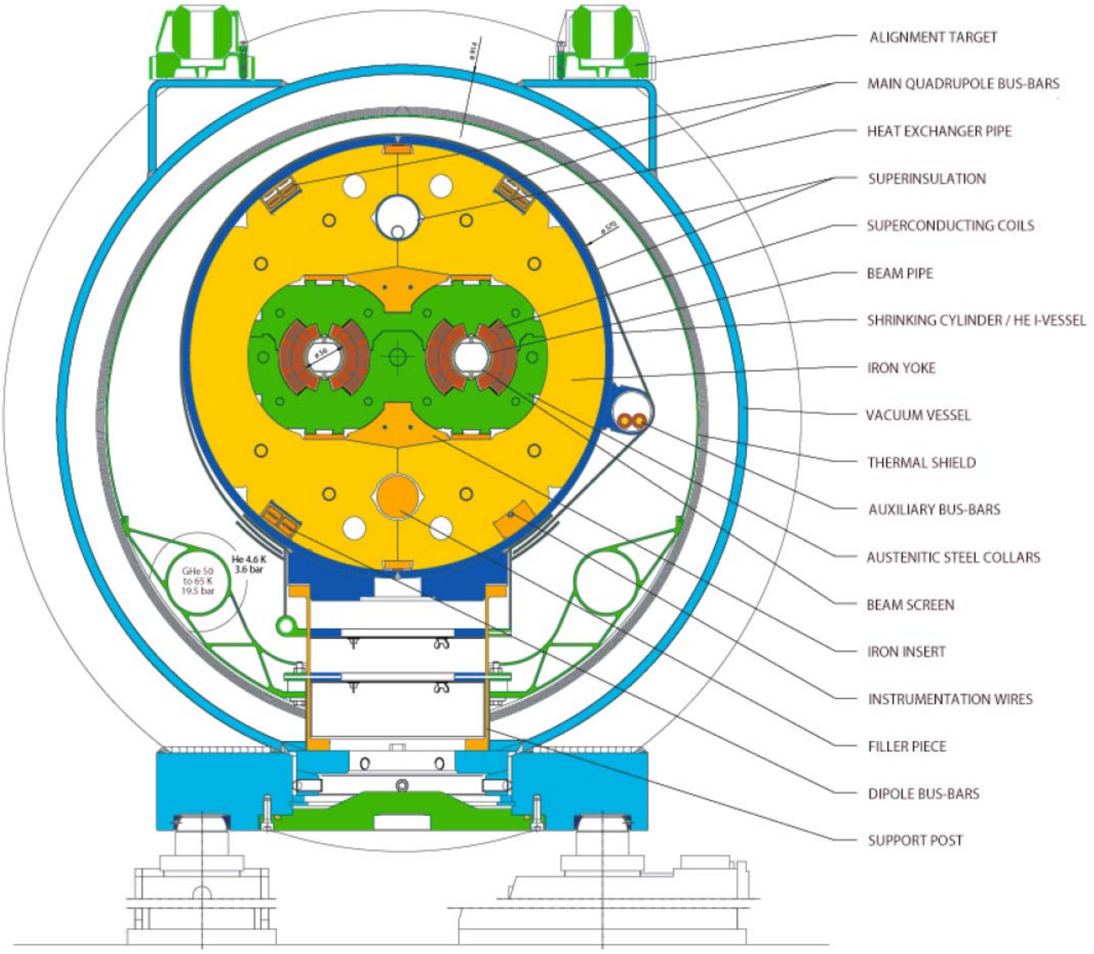

*Fig. 17. LHC Dipole cross-section [28].*

## 2.2.4 Blocks and windings

In order to generate perfect dipole and quadrupole fields transvers to the beam pipe, it is necessary to obtain current distributions as the ones schematically shown in Fig. 18. In real terms, it is not possible to realize this geometry using a coil, due to the size and rigidity of the cables and the need to use a single long cable around the magnet (joints would create huge losses).

The best approximation of the ideal geometry is obtained by two layers of superconducting cables with rectangular section (with a slight keystone angle), divided in blocks and separated by copper wedges to give to the coil a circular-like shape [12]. See Fig. 19.

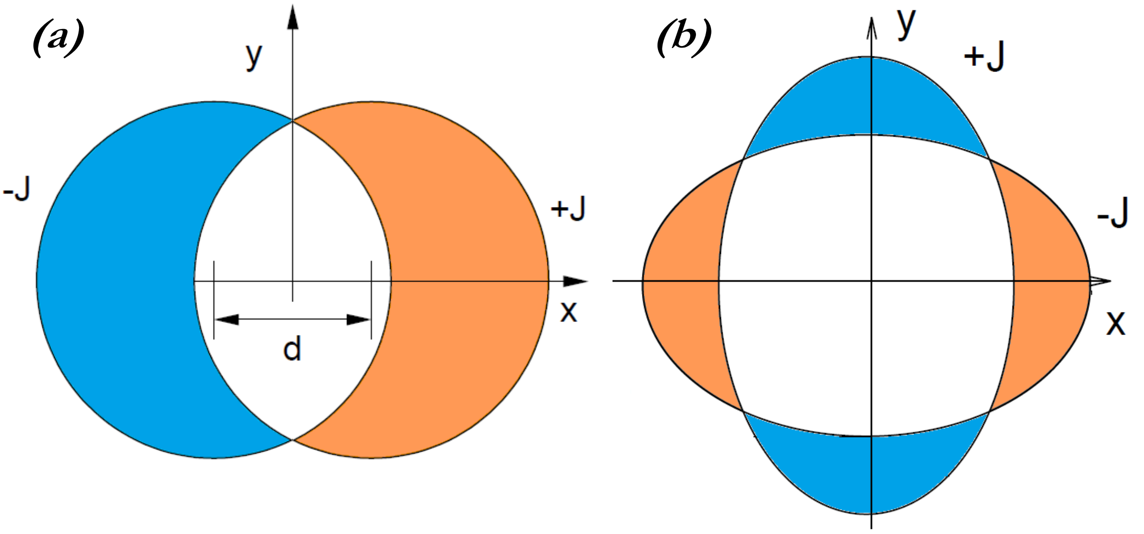

*Fig. 18. Ideal current densities to reproduce perfect dipole (a) and quadrupole (b) fields in the centre of the pipes [20].*

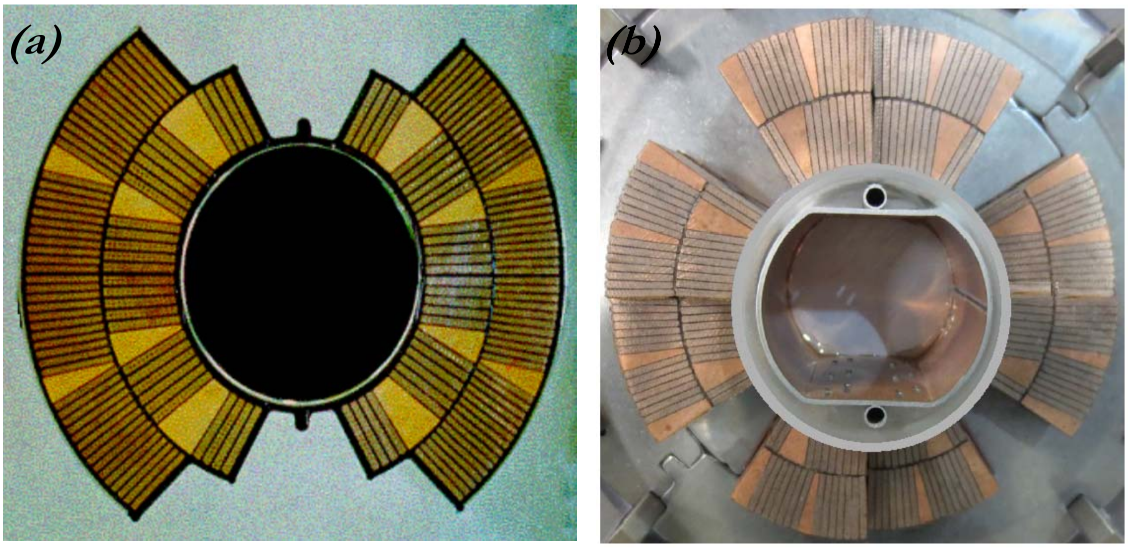

*Fig. 19. Real configurations of dipole (a) and quadrupole (b) coil geometries used to approximate the ideal ones.*

These limitations cause the presence of non-allowed harmonics in magnet bore, which reduce the quality of the resulting field; thus, corrector magnets of highest order are inserted to minimize these field distortions.

The magnetic field obtained with this current density configuration is not constant but variable along the width of the coil, as shown in Fig. 20; anyway, inside the cavity where the field must act properly, it reaches the quality demanded by beam physics requirements.

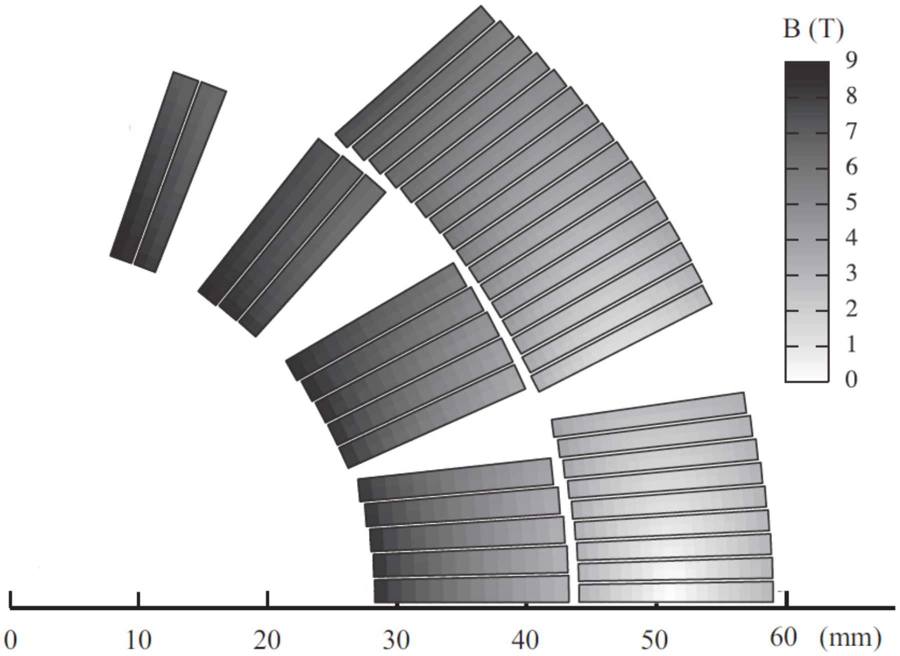

*Fig. 20. The magnetic field in one quadrant of LHC dipole magnets with a central field equal to 8.33 T at nominal current. Darker areas represents a higher magnetic field [12].*

### *2.2.5 Rutherford Cables*

As explained, superconducting cables have the role of carrying the current needed to produce the required magnetic field. Considering the 27 km of LHC, it may seem that the superconductivity takes place only in a small part of the device (a cable has only few $mm^2$ of section); in real terms, the whole length of superconducting cables needs to be considered, which is actually extremely long: considering all magnets, superconducting cables of 7600 km long are used, with the characteristics that are described below.

“Since the first superconducting accelerator magnets started operation in 1983, only Rutherford type cables are used in the design of all superconducting accelerators” [24]. Rutherford cables are flat cables consisting of multi-filament wires, called *strands*, arranged to obtain a rectangular section, and then twisted with a specific *twist pitch*. A twist pitch is the distance after which, looking at the cable main face, one strand returns to its original position. Strands are superconducting filaments formed in turn, by several thousands of micro-filaments of dimensions of few µm (see Fig. 21). The strand fabrication technique is a multi-step process that starts from the insertion of unreacted powder of superconducting material (NbTi, for example) inside a cylindrical matrix of normal material, to favour the phenomenon of *current sharing* (described in Chapter 3.2.5). As a result of extrusion and swaging processes, the diameter of the micro-filaments is reduced; then, more filaments are coupled together and the process is repeated several times until the number of micro-filaments and the size reach the desired values.

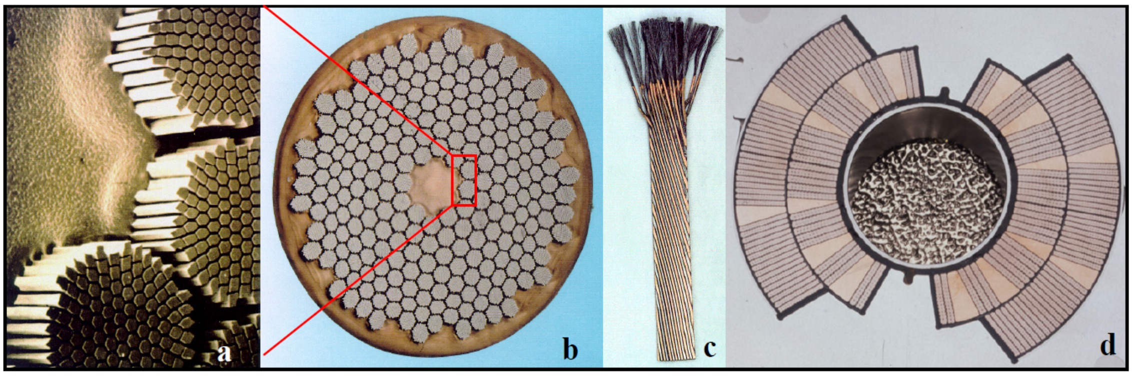

*Fig. 21. (a) A cross-section of NbTi filaments. (b) A cross-section of a multi-filament strand. (c) A Rutherford cable. (d) LHC dipole cross-section.*

Cable stability increases as the conductor cross-section decreases, for this reason superconductors are made of multi-filament wires with very small dimensions: this help to reduce the *flux-jump* problem. "This phenomena arises from current induced in the conductor by the presence of a changing magnetic field (for example the magnetic field ramping during charging operations)… These circulating currents extend for a finite length along the conductor, flowing in one direction on one side of the conductor and returning on the other side to complete the circuit" [29]. These currents are superimposed to the transport current, and they can cause a sudden movement of fluxoids, which causes the release of a lot of energy. If the heat generated does not quickly reaches the surface of the filament, in order to be dissipated by the normal material (which has good heat capacity), it can drive an increase of wire temperature that may be irreversible. Reducing the size of the filament allows the reduction of the distance that the heat generated inside the filament has to pass to reach its surface, minimizing the flux jump phenomenon.

Unfortunately, this is not sufficient because these coupling currents tend to interact within the cable when two filaments run in parallel; in this case currents create anyway closed paths, passing through the higher resistive normal matrix, causing diamagnetism and unequal distribution of currents in the strands. Twisting filaments (and strands too), forces the flux deriving from the external magnetic field to be alternated through successive short-dimension loops, reducing the effects of the flux jump and allowing a more rapid charge of the magnet.

Moreover, strands are compressed into a flat two layers structure with a trapezoidal shape, slightly keystoned to facilitate the winding into a cylindrical shape around the beam pipe. This configuration allows the highest current densities due to a very high packing factor and their mechanically stable structure [12]. See Fig. 22 to understand the structure.

Rutherford cables can differ depending on their use: modifying the geometrical parameters, the number of strands and the materials involved, cables with different properties can be obtained. According to [12], two different types of cables are used inside LHC:

- LHC 01 is utilized for the internal layer of main dipole magnets;

- LHC 02 is utilized for the external layer of main dipole magnets and for both layers of main quadrupole magnets;

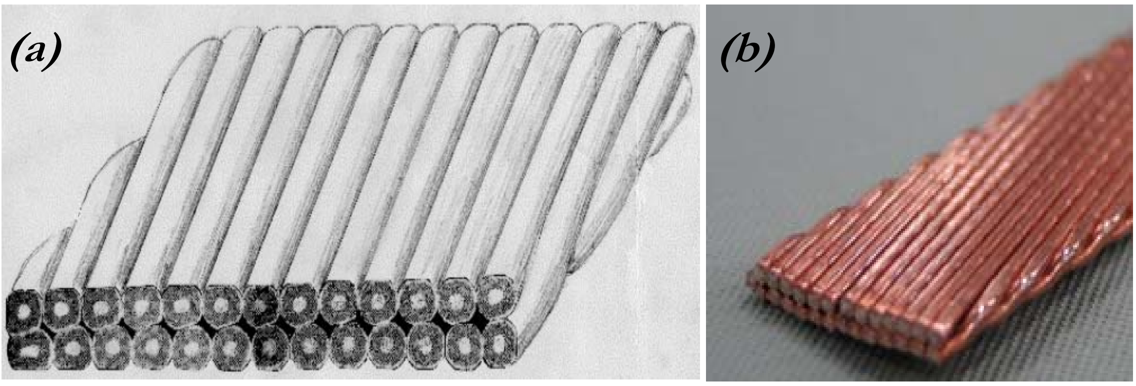

*Fig. 22. (a) Drawing of a Rutherford cable and (b) a real photo.*

All LHC cables are built using NbTi. Considering the magnetic field distribution plotted in Fig. 20, it is possible to explain the purpose of different cables within the same magnet: since the field in the outer layer is considerably lower than in inner one, the critical current density that these zones of the winding can support is greater. Thus, it is possible to reduce the superconductor cross-section of cables in the outer layer (LHC 02) hence reducing costs.

| | $Nb_3Sn$ | NbTi |
|---|---|---|
| *Cable data* | | |
| Strand diameter $[mm]$ | 0.850 | 0.825 |
| Number of strands | 40 | 36 |
| **Cu/nonCu** | **1.20** | **1.95** |
| Transposition pitch $[mm]$ | 109 | 100 |
| Width $[mm]$ | 18.15 | 15.1 |
| *Operating conditions* | | |
| Total current $[kA]$ | 16.47 | 11.87 |
| Current density $[kA/mm^2]$ | 1.6 | 1.8 |
| Peak magnetic field $[T]$ | 11.4 | 6.85 |
| Temperature $[K]$ | 1.9 | 1.9 |

*Table 2. Comparison between High-Luminosity MQXF Nb3Sn cables and actual MQ NbTi cables [1].*

The High-Luminosity project, as explained in Chapter 3.2.2.2, requires the replacement of some quadrupoles with more powerful magnets called MQXF; this modification makes it necessary to involve different material for Rutherford cables, such as $Nb_3Sn$, to substitute NbTi, used nowadays (see Tab. 2 for a comparisons of the main characteristics of NbTi and $Nb_3Sn$ cables). Following past studies [1] [1 - 30], this thesis will make reference at these new $Nb_3Sn$ Rutherford cables utilized for MQXF, considering their geometric parameters.

### *3.2.5 The current sharing phenomenon*

As already mentioned, the reason why the strands that constitutes a superconductive Rutherford cable are designed by coupling superconducting material with normal material is to favour the current sharing: it is useful to describe briefly this phenomenon.

The material can transit even when the temperature does not exceed the $T_c$, but for example, when its current density exceeds its critical value $J_c$. From the definition of critical surface (see Chapter 1.3) is known that the three parameters involved ($T, J, B$) are each one a function of the others: setting the magnetic field $B$ as a fixed value, if the temperature increases the critical current density falls. If the field is set, then the current able to generate it is fixed as well. Therefore, it can be expected that an increase in temperature, even very limited, can cause the approaching of current density to its critical value up to its overcoming. In all cases, a transition to the normal state produces an increase in superconductor material resistivity, which it is usually higher than normal materials resistivity. This can generate a relevant amount of heat by Joule effect.

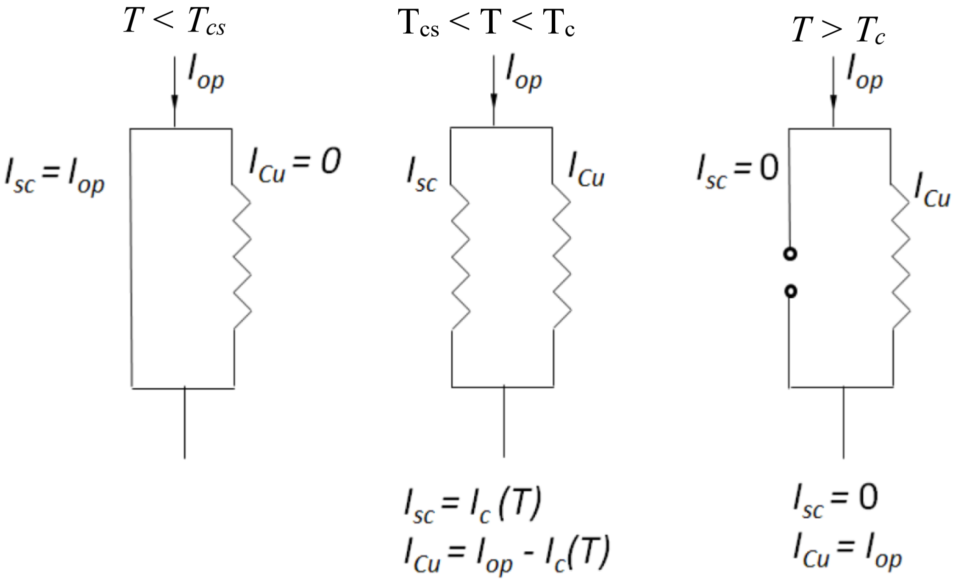

*Fig. 23. Schematic representation of the current sharing phenomenon depending on the evolution of the temperature [*20*].*

To prevent material damaging due to heat, the superconducting strands are manufactured in composite form: superconducting filaments are immersed in a matrix of copper or another normal metal characterized by a lower resistivity than that of the superconductor in its normal state. In this way, when the temperature exceeds the $T_{cs}$ value (called *current sharing temperature*), the current sharing phenomenon takes place: in the superconducting material flows a current equal to the maximum current density $J_c$ without being exceeded, while in the normal conductive material flows the remaining current that could not be handled by the superconductor without undergoing transition. Once the temperature surpasses the $T_c$ value, $J_c$ is equal to zero and all current flows in the normal conductor, realizing a shunt for the superconductor and preventing its damage (see Fig.

23 for an operative scheme). This situation can last only for few moments because losses produced in the normal conductor by Joule effect are huge and difficult to handle; therefore, it is fundamental that the system which has to detect and control all sources of heat into the system acts extremely fast.

## *Chapter 3*

# *Interstrand coupling currents induced by time-varying magnetic field*

Superconducting cables for accelerator magnets can be subjected to a variety of perturbations involving the release of energy into the system. Not all these disturbances are sources of heat coming directly from outside the system, but in many cases the heat (or better: the *losses*) originates internally to the cable as a result of phenomena induced by external causes. One of these causes is represented by a magnetic field variable in time.

In LHC, during operations of injection of particles and of beam dump at the end of the survey period, the magnetic field is ramped up or down at speeds that vary according to the needs, thus creating magnetic field cycles variable in time, that repeat several times during the life of a magnet.
A variation of the magnetic field induces an electromotive force ($\varepsilon$) on a conductor loop (superconductive or not), which corresponds to an electric field that forces the charges to flow around the wire: thus, currents are induced inside the conductor. According to the Faraday's law, the induced electromotive force in a coil (thus the intensity of the induce currents) is proportional to the opposite of the rate of change of magnetic flux $\Phi_B$:

$$\varepsilon = - \frac{d\Phi_B}{dt}$$

For this study, only variations in $B\perp$ (the field normal to the cable main face) will be considered, since the magnitude of the induced eddy currents is mainly affected by this component.

In a Rutherford cable, these currents can be induced on more "levels": in fact, *intra*strands (or interfilament) eddy currents and *inter*strand eddy currents coexist. The first ones originates at the level of filaments that constitute strands, mostly in the normal resistive matrix that surrounds the individual superconducting filaments (introduced to reduce the problem of the flux-jump). The second ones flow and connect the various strands that compose the cable. It is possible to study these current distributions separately in consequence of their different time constants [7]. This thesis is focused on the latter, which are here described.

Interstrand eddy currents can be distinguished between:

- Interstrand Coupling Currents (also called ISCCs [2])

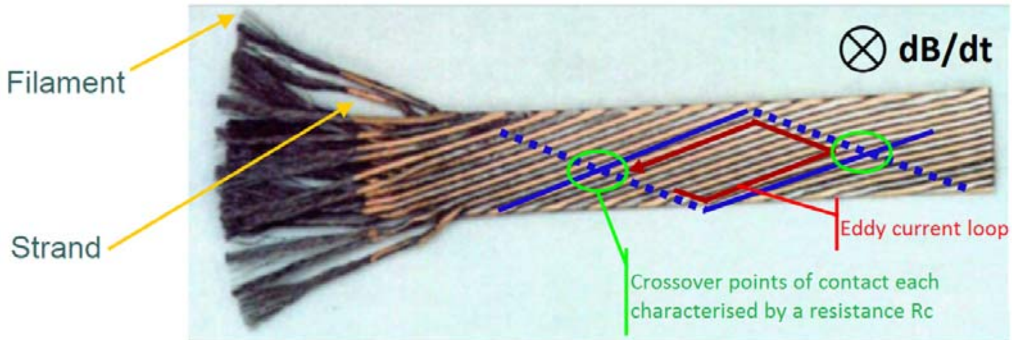

*Fig. 24. Rutherford cable with the highlight of a typical current loop induced by a normal magnetic field variation in a cable [31].*

They circulate between the various strands creating loops, which close flowing through the points of contact between strands. Their form depends on the particular geometry of Rutherford cables (several strands twisted and not isolated with each other). Depending on the position of one strand over another, they can circulate around two different paths [32]:

- Diamond-shaped loops, which connects one strand of the upper layer and one of the lower layer, by cross-over points of contact characterised by a resistance *Rc*.
- Parallel-strand loops in which the current flows between adjacent strands and where contact points are characterized by a resistance *Ra*.

It is possible to refer at *Ra* and *Rc* together, calling them *ICRs* (interstrand contact resistances); see a representation of *ICRs* and current loops on a cable in Fig. 24 – 25 - 26. The greater is the area of the loop and the higher is the intensity of the current flowing in it; twisting strand can be useful to reduce these areas.

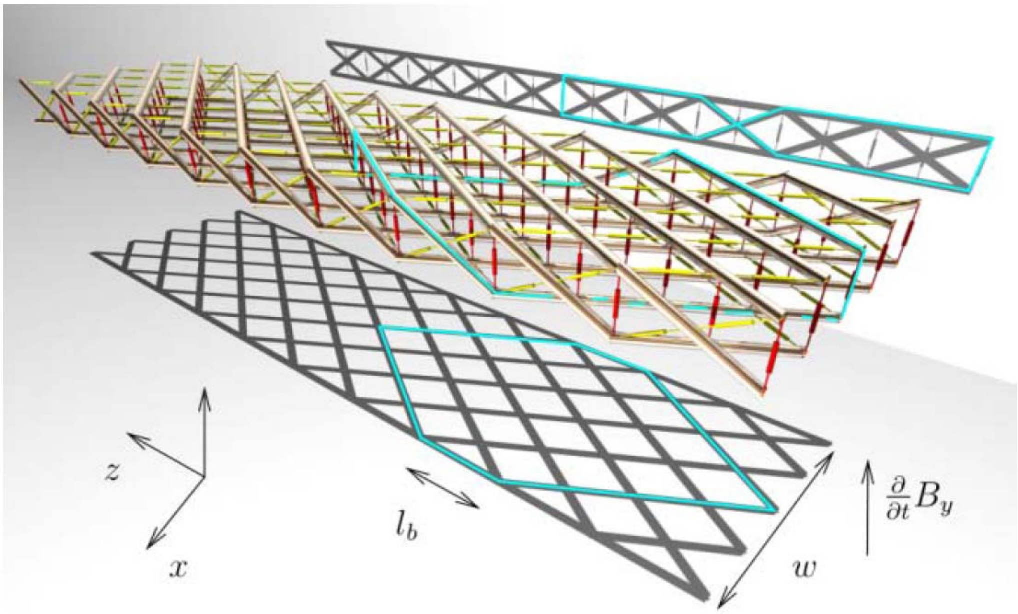

*Fig. 25. 3D representation of a Rutherford cable with 10 strands, with the highlight of a typical current loop induced by a normal magnetic field variation in a cable. Adjacent resistances Ra are displayed in yellow and cross-over resistances Rc in red [33].*

These currents exhibit time constants of typically 0.01 to 10 seconds and have a characteristic loop length of one twist pitch [2]. For this reason, they are also referred as short-range coupling currents.
The model presented on this thesis focuses on ISCCs distribution.

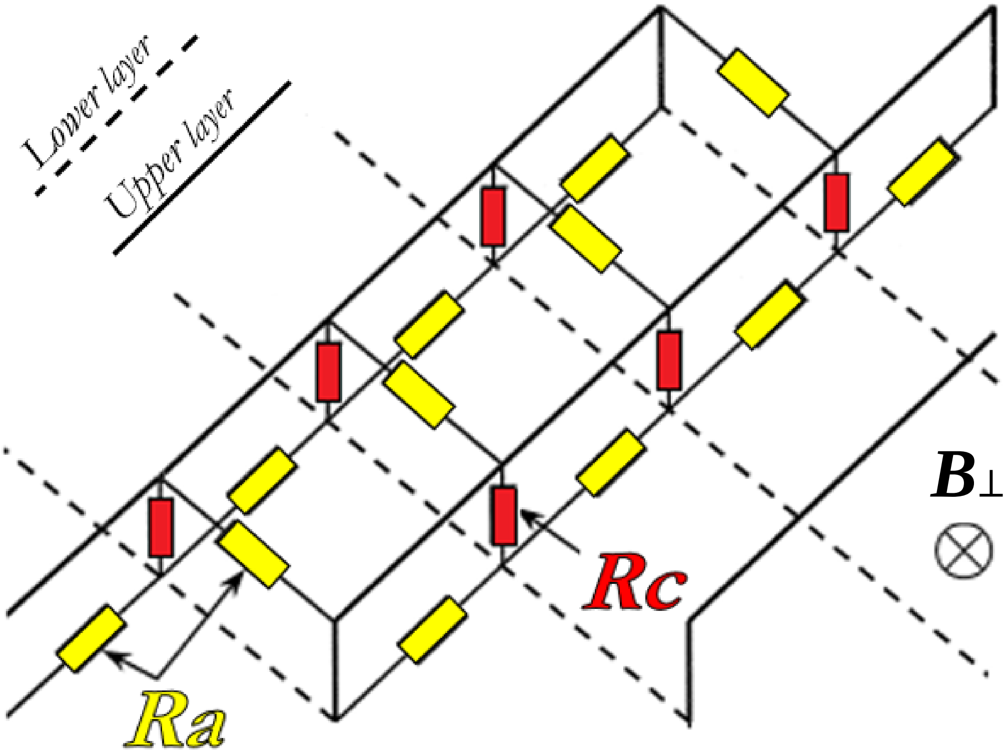

*Fig. 26. Schematic representation of a portion of the cable length with resistances Rc and Ra represented as lumped parameters.*

- Boundary-induced coupling currents (also called BICCs or “supercurrents” [2])

They are caused by inhomogeneities (intended as "boundaries" between two areas with different characteristics, hence their name) along the length of the cable, such as magnetic field B⊥ or *ICRs* (i.e. at joints, coil ends, or for manufacturing errors etc.). BICCs differ from ISCCs because they flow into strands over distances of 10-$10^3$ times the cable pitch, for this reason they are also referred as long-range coupling currents.

Following the scheme of Fig. 27, in a cable consisting of only 2 strands, a magnetic field variable in time and space is applied. On the right of the point $z = 0$, the cable is subjected to a field variation $dB/dt$ that induces ISCCs circulating in each loop at $z > 0$, while on the left of the point $z = 0$, the field is constant and at the initial time no current is induced. “However, the current in circuit 5 generates a voltage in circuit 4 which has to be compensated for since $dB/dt = 0$ in circuit 4. This is achieved by an additional current with alternating direction being generated in all contacts. This results finally in a large current loop where one strand carries positive current and the other negative current” [2]: these are the BICCs.

They exhibit large characteristic times of $10^2 \div 10^5$ s (for practical cables) which are several orders of magnitude larger than the time constant of the interstrand coupling currents [2]. Furthermore, their amplitude can be orders of magnitude higher than short-range coupling currents [7], and it increases strongly if the lengths of the $B\perp$ variations are of the same order or smaller than the cable twist pitch.

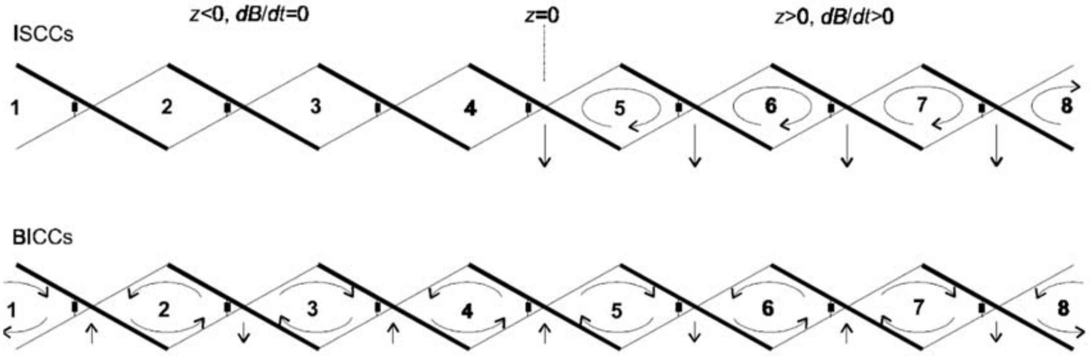

*Fig. 27. Representation of ISCCs and BICCs generated in a 2 strands cable due to magnetic field varying in time and space* [2].

Despite the intensity of these currents is generally not high, BICCs and ISCCs are the source of several problems:

- They compete with the transport current reducing the $I_c$, thus affecting the cable stability [2].
- Even when they are too weak to cause reductions of $I_c$, they are responsible for the so-called "*dynamic magnetization*" that induces multipolar harmonics in the dipole and quadrupole bore field, causing their distortion [34].
- They cause the introduction of power in the system. For ISCCs, the current flowing from one strand to another pass through *ICRs* dissipating heat, while BICCs "stay in the strands and that implies that they generate almost no heat compared to the inter-strands coupling losses" [3]. To ensure the stability of a magnet, it is very important to estimate the value of these losses; the aim of this thesis is precisely to analyse their magnitude and distribution in cables and how they change varying several parameters.

Since operation of field ramping cannot be avoided, a way to reduce ISCCs and BICCs and the corresponding losses is to act on resistances *Rc* and *Ra*, ensuring that they are kept within certain "compromise ranges". These resistances should be sufficiently high in order to suppress or reduce the coupling currents, but still enough low to guarantee a proper current sharing between strands and not affect stability [14 - 15]. In Chapter 5 a methodology to work in this direction is introduced and discussed.

Since the term stability has already been introduced, it may be useful to explain it briefly: despite not pertaining to the objectives of this thesis it is related the importance of calculation of losses due to electrodynamic transient.

“In applied superconductivity the terms “*instability*" and “*stability*" are used to describe the capacity of a system to remain in- or to recover to its nominal operating conditions after an internal or external perturbation” [35]. The temperature of a region of a superconducting wire may rise due to an introduction of heat into the system (internal or external); once the critical temperature is overcome, the material undergoes transition.

*Fig. 28. Heat balance that a superconductor cable has to sustain when its condition is perturbed, in order to maintain the correct operation* [36].

The control systems ensures that the refrigeration system removes all the heat generated by the various sources in the most rapid way, reducing the temperature and returning to an “equilibrium condition” between heat inserted and heat removed (see Fig. 28). If that happens, the material returns to its starting conditions and maintains a correct operation (this situation is called *recovery*), but if this is not possible the system temperature can keep growing, degenerating in the phenomenon called *quench*. This phenomenon occurs very rapidly ($10^{-4} \div 10^{-1}$ s) and due to the heat propagation the initial normal zone may extend up in the whole superconductor, resulting an increasing of resistance of the entire winding [20].

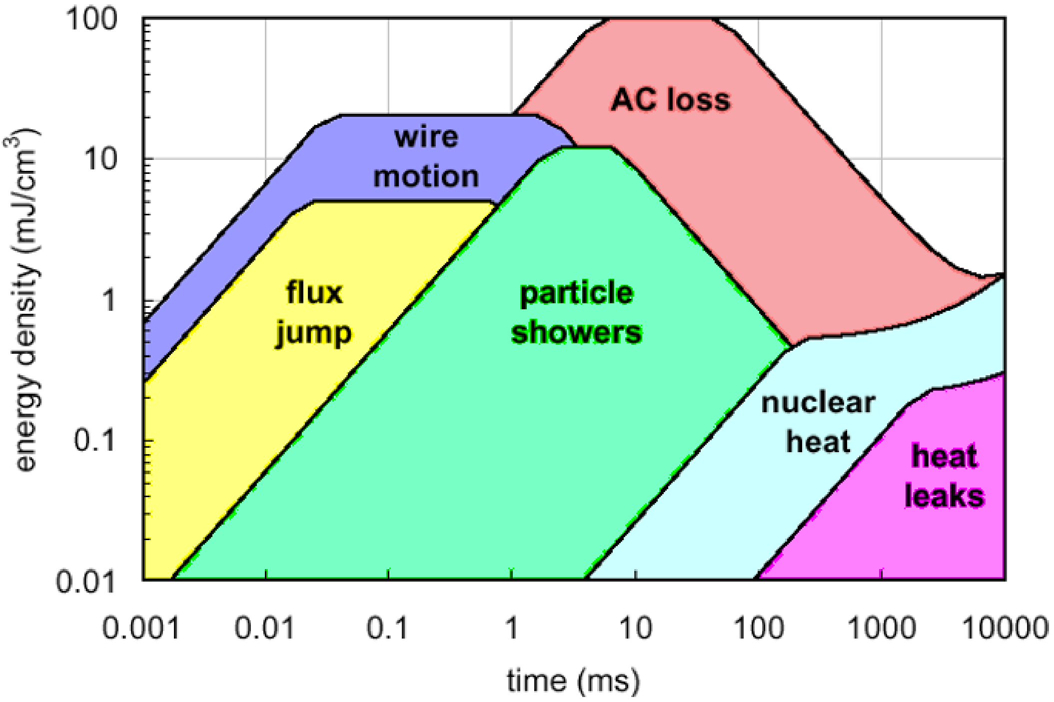

*Fig. 29. The perturbation spectrum [36]*

In Fig. 29 a perturbation spectrum is shown: it represents a summary of the main energy inputs that can be deposited by various mechanisms in a superconducting magnet, as a function of the characteristic time for the energy deposition. It is necessary to predict and estimate the amplitude of all possible sources of losses to which a magnet can be subjected to carry out a complete study of stability. This work focuses on a specific type of loss: the one due to electrodynamic transient, which can be included within the category of AC losses. Data extrapolated from the model can then be used to realize more complete stability analysis.

## *3.1 Modelling interstrands coupling currents*

Over the years, several models were proposed for the study of coupling currents and the corresponding AC losses. A couple of them will be briefly described to understand how the approach followed in this thesis differs from previous ones.

### *3.1.1 The network model*

The earliest presentation of this model was given by Morgan in 1973 [37], afterwards several authors have used it to elaborate more advanced versions [3 - 6]; their basis, however, remain always very similar.

It approximates the cable as a lumped parameters circuit, where strands of a Rutherford cable belonging to one of the two layers are assumed to have electrical contacts with the strands of the other layer but not between themselves (resistance *Ra* is considered higher than resistance *Rc*). The elementary cell of the model is constituted by the simplest loop formed due to the twisting of the strands: when two adjacent strands from one layer intersects two adjacent strands of the other layer, the loop is formed.

As it is possible to see from Fig. 30, all loops include four resistances, except those at the cable edges which have three, and all cross-over resistances are assumed to be the same along the cable length and may vary just along the cable width. Each loop is characterised by an external time-dependent magnetic flux $\Phi$, uniform along the cable length; it penetrates loops inducing cross-over currents $i$ to flow through the contacts. These currents are equivalent to ISCCs, but through this method it is also possible to estimate the behaviour of BICCs, which flows directly inside each straight segment of the loop. With these assumptions, there are only $N-1$ (where $N$ is equal to the number of strands) independent loops in the cable, whose values are to be found.

To solve those loops a matrix approach is used: $N-1$ horizontal rows and a number of zigzag columns $k$ (that depends on the cable length) are considered. Applying Faraday's law to the $N-1$ loops of a generic column a system of equations is obtained, from which calculate interstrand eddy currents in every point of contact.

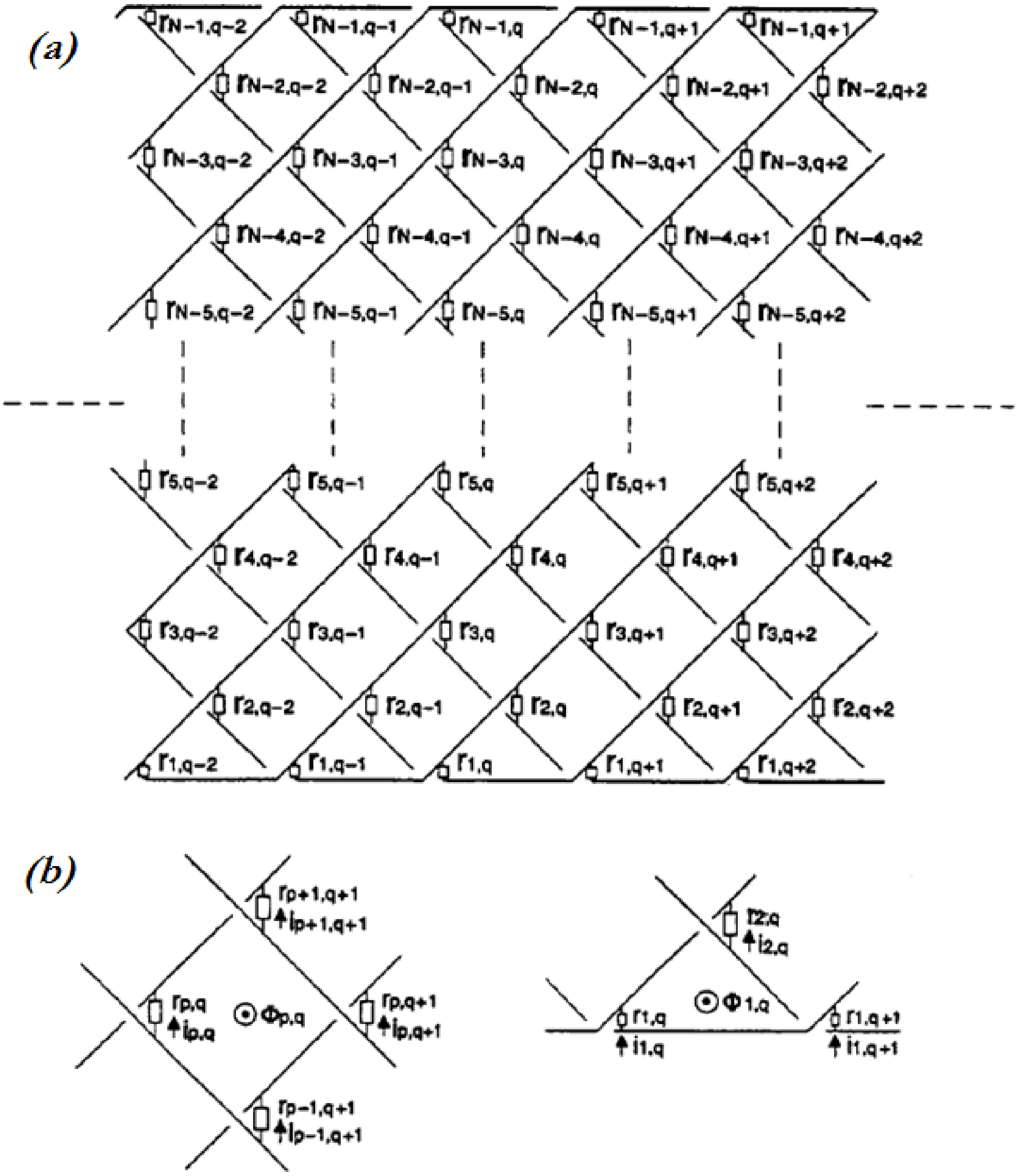

*Fig. 30. (a) Equivalent scheme of a Rutherford cable considering the network model, and (b) an highlight of a elementary loop placed inside the cable and one located at the cable edges [6].*

More recent developments of the network model, demonstrate that it is possible to use the same approach, also considering longitudinal variations of the cross-over resistances and of the changing magnetic field. Applying Kirchhoff's equation on each row of the matrix it allows to calculate the cross-over currents by a step by step process from the knowledge of the currents in the previous column. An important result found, is that cross-over currents of the *(k+N)*$^{th}$ column are equal to those of the *k*$^{th}$ column; this means that cross-over currents between any two strands of the cable repeats equally after every twist pitch length [6]. See Fig.31 for a schematic explanation of this concept.

Once the currents are note, it is then possible to calculate losses in W per meter of cable.

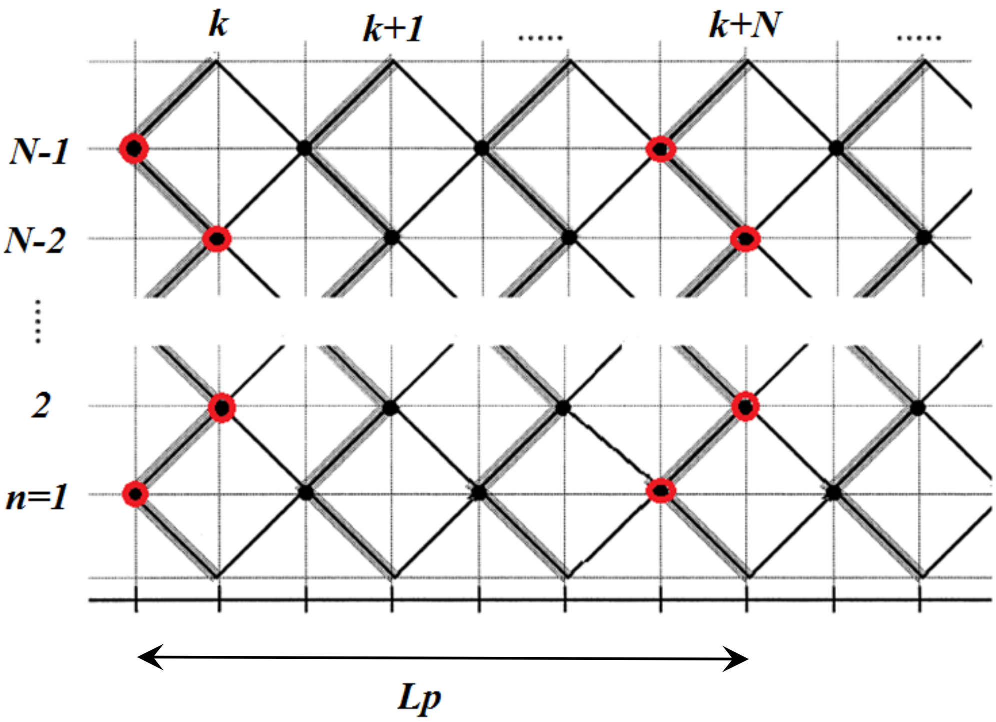

*Fig. 31. Matrix representation of the cross-contacts of a cable with N-1 rows, considering the network model. The red dots means that contacts are equal: the column k which describes cross-over currents repeats itself equally after one twist pitch length at column k+N [4].*

The network model is widely used because it allows to obtain fine information about ISCCs and BICCs (and their corresponding losses) in Rutherford cables, with the possibility of varying value of *Rc* and *dB/dt* along the width and the length of the cable. This approach is however limited by the rapid growth of computational size when the number of unknowns is very high or when the size of the matrix becomes large; this unfortunately is what occurs simulating real long cables made of some tens of strands used in superconducting accelerator magnets, and makes it difficult to implement this method to practical cases.

### *3.1.2 The continuum model*

A different model is developed to overcome the limits mentioned above, called "continuum model" [7 - 9] to underline its differences from Morgan’s approach: it represents the cable using a distributed parameters circuit.

This model considers each strand as a distinct electric element, and it assumes that strands can carry a current distributed in a uniform way in their cross-section, neglecting the influence of intrastrand coupling currents between filaments. Furthermore, it considers that the current transfer between different strands happens along the length of the cable in a continuous manner [7].

Parameters are introduced in this model as uniform quantities smeared over the length *dx* of an “elemental mesh” which describes the connection between strands. A conclusion established in the network model is that multistrand superconducting cables have an intrinsic periodicity related to the twist pitch length, thus an appropriate value for the length *dx* is a multiple or a fraction of the twist pitch.

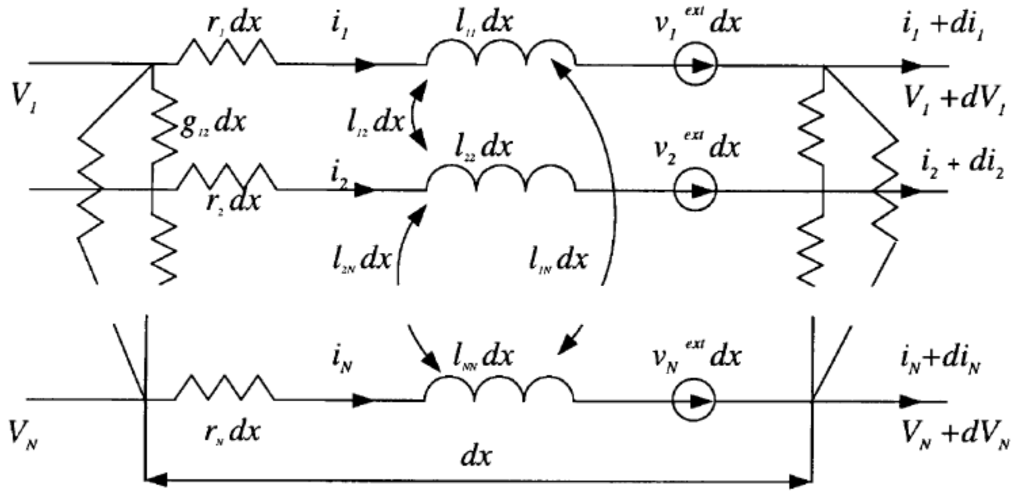

*Fig. 32. Representation of the elemental mesh of a cable used in the continuum model [7].*

In the elemental mesh, the main parameters are distributed over *dx*, as it is possible to see from Fig. 32: parallel resistances $r_i\,dx$, conductances between different strands $g_{ij}\,dx$ (the so-called $g_c$ and $g_a$ which depends on *Rc* and *Ra*), mutual- and self-inductances $l_{ij}\,dx$ and voltage sources $v^{ext}_i\,dx$ induced by the variation of the external magnetic flux density (which drives current to flow in the strands).

In the first approach of this method, electric conductance values for each couple of strands are set uniform over the length of the cable, and equal to:

$$g_c = \frac{2}{Lp \cdot Rc}$$

$$g_a = \frac{2\,(N-1)}{Lp \cdot Ra}$$

Where $g_c$ is equal to the conductance per unit length between non-adjacent strands, $g_a$ is equal to the conductance per unit length between adjacent strands, *Lp* is the cable twist pitch and *N* is the number of strands. *Ra* and *Rc* are lumped values introduce to make comparisons with the network model: *Rc* is the electrical resistance which characterize contacts between non-adjacent strands while *Ra* is the electrical resistance between adjacent strands, inserted in the same positions of the resistances *Rc*.

Numerators of conductance formulae are calculated taking into account that each strand crosses every other non-adjacent strand twice within a twist pitch length (for this reason the numerator of $g_c$ is 2) and the total number of contacts that a single strand encounters during a twist pitch is equal to 2($N$-1) (for this reason the numerator of $g_a$ is 2($N$-1)).

If the conductance is uniform along the cable length, it is clear that this method can not be used for a fine calculation of ISCCs which require a higher level of detail in the representation of the cable. However, the model can be used for long-range coupling currents analysis.

Applying Kirchhoff 's voltage and current laws to the $N$ nodes of the elementary mesh, and imposing the conservation of total operation current in the cable cross-section, a system of $N$-equations linearly dependent is derived, that can be rearranged in the following matrix form:

$$\begin{aligned} \frac{\delta \boldsymbol{v}}{\delta x} &= -\,\mathbf{r}\,\mathbf{i} - \mathbf{l}\frac{\delta \mathbf{i}}{\delta t} + \boldsymbol{v}^{\mathbf{ext}} \\ \frac{\delta \mathbf{i}}{\delta x} &= \boldsymbol{g}\,\boldsymbol{v} \end{aligned} \qquad (1)$$

Where terms in bold represent vectors and matrices of the relative quantities (see [7] for a detailed explanation).

If the second equation of (1) is derived in space, the term $\delta \boldsymbol{v}/\delta x$ appears; coupling it with the first equation, the following set of $N$ equations is obtained, that describes the process of current diffusion along the cable:

$$\boldsymbol{g}\,\mathbf{l}\,\frac{\delta \mathbf{i}}{\delta \mathrm{t}} + \frac{\delta^2 \mathbf{i}}{\delta x^2} + \boldsymbol{g}\,\mathbf{r}\,\mathbf{i} - \boldsymbol{g}\,\boldsymbol{v}^{\mathbf{ext}} = 0$$

This formula is exact only if the conductance variation along $x$ coordinate is negligible, or rather, if elements of $\boldsymbol{g}$ matrix are considered uniform along $dx$.
Finally, applying the proper initial and boundary conditions it is possible to determine the values of currents in each strand of a cable subjected to a time-varying magnetic field.

Despite the first approach of the continuum model allows self-consistent multi-physics analysis and it is suitable for simulations of multistrand cables with real length, it considers a uniform conductance along the cable length, and it does not reproduce accurately the necessary details. Thus, it does not allow a proper evaluation of short-range coupling currents.

The same authors have tried to overcome this limit in [10], rewriting equations (1) considering a second approach: starting from the same set of equations, the equation of one strand is arbitrarily removed (representing quantities as matrices or vectors this corresponds to a deletion of one row), and this strand it is taken as the reference strand. The set of equations (1) can be rearranged in the following set of $N$-$1$ equations:

$$\begin{aligned} \frac{\delta \Delta \boldsymbol{v}}{\delta x} &= - \tilde{\mathbf{r}}\,\mathbf{i} - \tilde{\mathbf{l}}\frac{\delta \mathbf{i}}{\delta t} + \Delta \boldsymbol{v}^{\mathbf{ext}} \\ \frac{\delta \mathbf{i}}{\delta x} &= \tilde{\boldsymbol{g}}\,\Delta \boldsymbol{v} \end{aligned} \qquad (2)$$

Where the values written with ~ are created starting from the matrices of equations (1); moreover, terms of potential difference with respect to the reference strand appear.
Matrix $\tilde{\boldsymbol{g}}$ is more general than matrix $\boldsymbol{g}$**,** with no hypothesis on its space dependence in order to allow that the conductance can change along the *x* coordinate, avoiding the limit of its uniformity along cable length.
Matrix $\tilde{\boldsymbol{g}}$ obtained is non-singular, and can be inverted in the second equation of (2), which is then inserted into the first equation to obtain the final set of *N-1* equations equal to:

$$\tilde{\mathbf{l}}\,\frac{\delta \mathbf{i}}{\delta t} + \tilde{\mathbf{r}}\,\mathbf{i} - \frac{\delta}{\delta x}\left(\tilde{\boldsymbol{g}}^{-1}\,\frac{\delta \mathbf{i}}{\delta x}\right) = \Delta \boldsymbol{v}^{\mathbf{ext}}$$

Unlike the previous version, this set of equations can be solved to find currents that flow into strands with the necessary level of detail to allow the calculation of ISCCs.

The intent of this thesis is precisely to implement the latter approach of the continuum model, to derive the distribution of short-range coupling currents and their corresponding losses in Rutherford cables.

# Losses and current distribution in superconducting Rutherford cables

Due to the high number of parameters involved and by the complexity of the system, it is obviously required to use a calculator to apply the model to practical cases.

## 4.1 Model implementation in THEA

The modelling and the simulations are carried out by means of the THEA software: it is a tool to perform one-dimensional multi-physics analysis involving three different domains: thermal, hydraulic and electric (THEA is in fact the acronym of *Thermal Hydraulic Electric Analysis*). With regard to this work, only the electrical domain is considered, since the focus concerns a specific current distribution; however, it is important to understand that it is easily possible to couple this model with the thermo-hydraulic model (already implemented in THEA) to obtain a complete analysis of transients.

Without going into detail about the THEA software (for a thorough discussion see [11]), it will be sufficient to know that to launch the program it is necessary to provide a *Fortran* code file (called *.input* file) where the main characteristics of the cable, the system conditions and the simulation parameters are set; this file calls some external functions (called *External Routines*) that describe in more detail some specific parameters. For the purposes of this thesis, three routines are involved (the *UserVoltage, UserConductance* and *UserInductance* routines); the assumptions made for drawing up these files will be described in different sub-chapters.

Below, the main considerations in drawing up the *.input* file are reported:

- A number of *Electrical Elements* equal to the number of strands are considered. As already specified, no *Hydraulic* or *Thermal Elements* are inserted into the system; this is a simplification of the physical cable required for our purposes.

- Initial conditions of constant current equal to zero are imposed in the system for the set of differential equations. Not considering transport current allows to focus only on currents induced by the magnetic field)

- Boundary conditions of constant current equal to zero are imposed at both boundaries of each element. As for the previous point, this simplification does not reflects what happens during the normal operation of a magnet. However, for the purposes of this thesis, these simplifications are acceptable and, as will be explained at the end of this chapter, allow to deduce other considerations.

- The function describing the time-varying magnetic field (which in this case represents the source that induces currents) is not explicitly expressed, but it is included within the routine that determines the induced voltage.
- No strain is applied on the cable.

### 4.1.1 Induced voltage calculation

The continuum model considers that each strand is characterized by an external voltage source, induced for example, by a time-varying magnetic field. See Fig. 33.

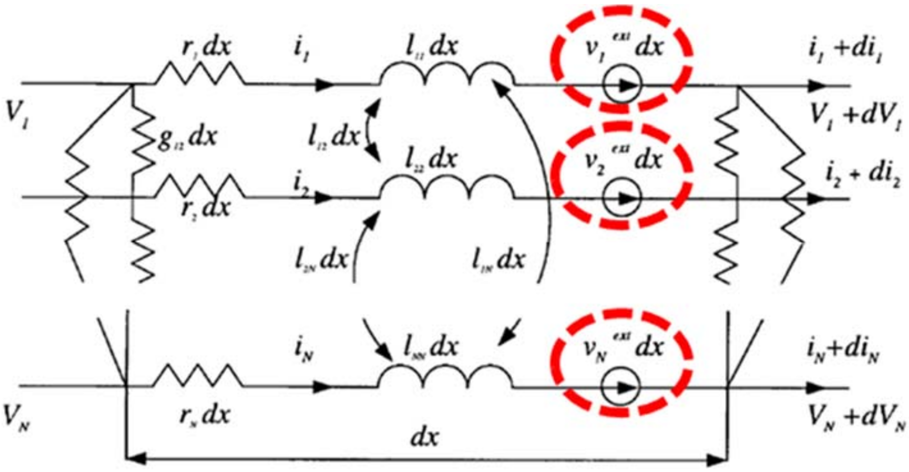

*Fig. 33. The elemental mesh of the continuum model with the highlight of the voltage source for each strand [7].*

For each strand the source of voltage per unit length (due to a time-varying magnetic field) is defined using the following formula:

$$V(x) = \frac{dA(x)}{dx} \cdot \frac{dB}{dt}$$

Where:

- *dB/dt* is the time derivative of the magnetic field function; for the purpose of this thesis only linear magnetic field variations is considered (practical values of field ramp rate are between 0.05 and 0.1 T/s, see Fig.34), even if the simulations can be extended to more complex cases.

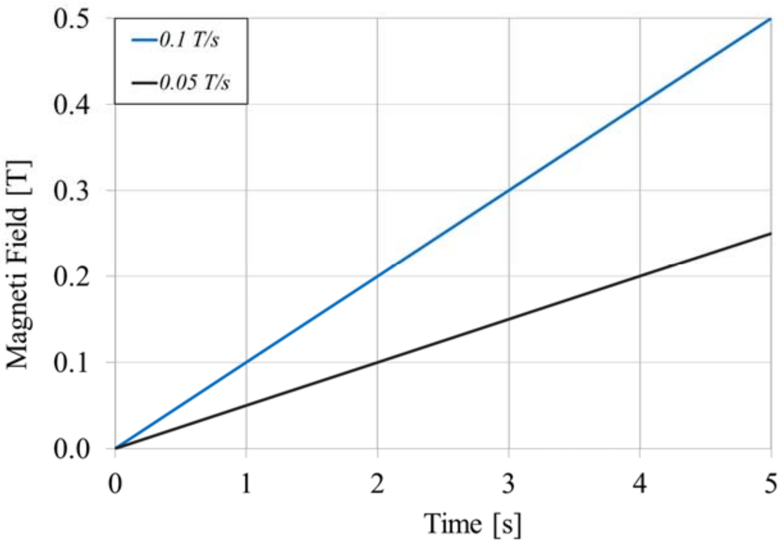

*Fig. 34. Ramp rates for the time-varying magnetic field used for this work.*

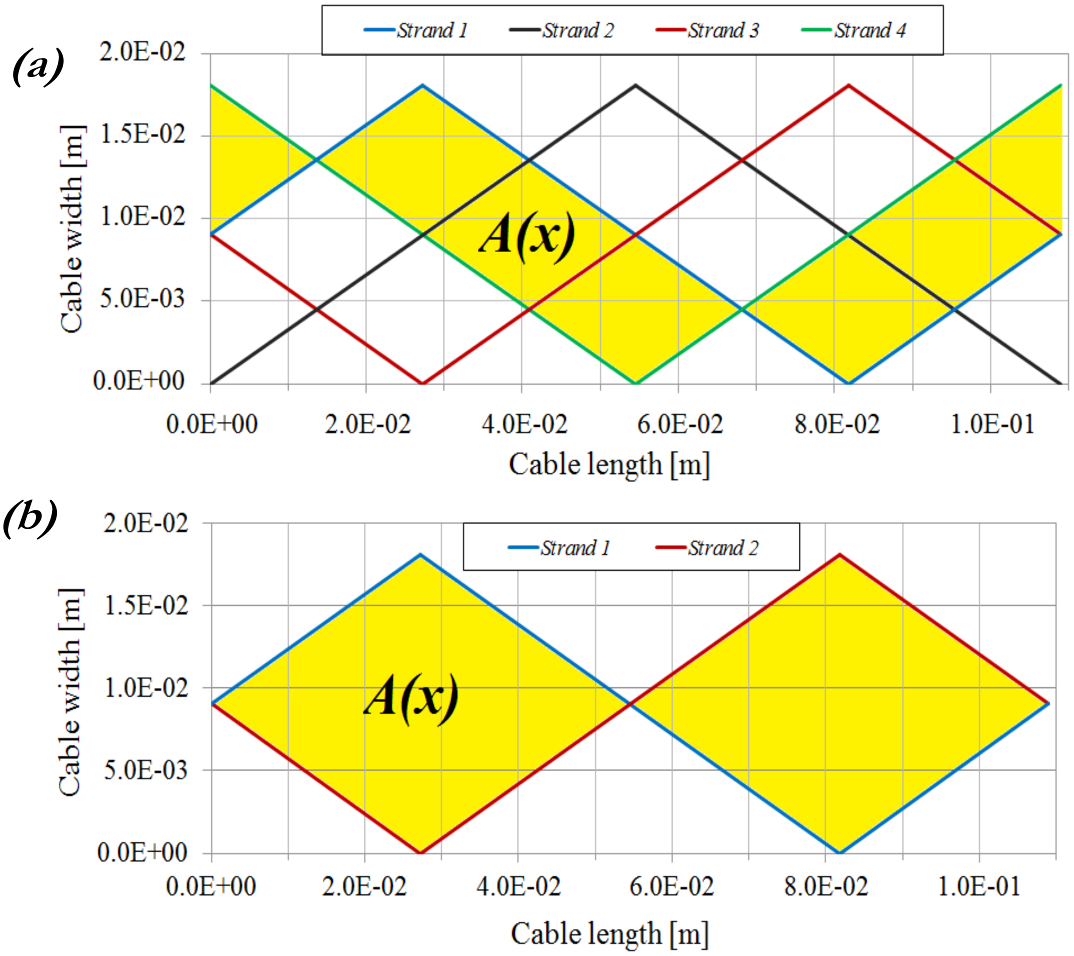

*Fig. 35. 2D representations of a 2 strands cable (a) and a 4 strand cable (b). In both charts the yellow area corresponds to the area of the loop formed by strand 1 respect and the reference strand (last strand)*

- $dA(x)/dx$ is the space derivative of $A(x)$, a function describing the area of the loop formed by the generic strand and the last strand, taken as reference. This area depends both on the cable geometry and on the strand considered each time; see Fig. 35 for clarification. Note that with these assumptions the area and thus the induced voltage for the last strand are null: in fact the voltage is introduced in the equations as a potential difference to the reference strand.

  Furthermore, it is noticed that the $dA(x)/dx$ function has another geometrical meaning:

$$\frac{d\,A(x)}{dx} = y\ position_i(x) - y\ position_{reference}(x)$$

  Where:

  $y\ position_i\ (x)$ = $y$ position of the $i^{th}$ strand compared to the axis passing through the middle of the cable width. See Fig. 36.

  $y\ position_{reference}\ (x)$ = $y$ position of the reference strand compared to the axis passing through the middle of the cable width.

  This definition allows a simpler implementation in the code for the $dA(x)/dx$ function.

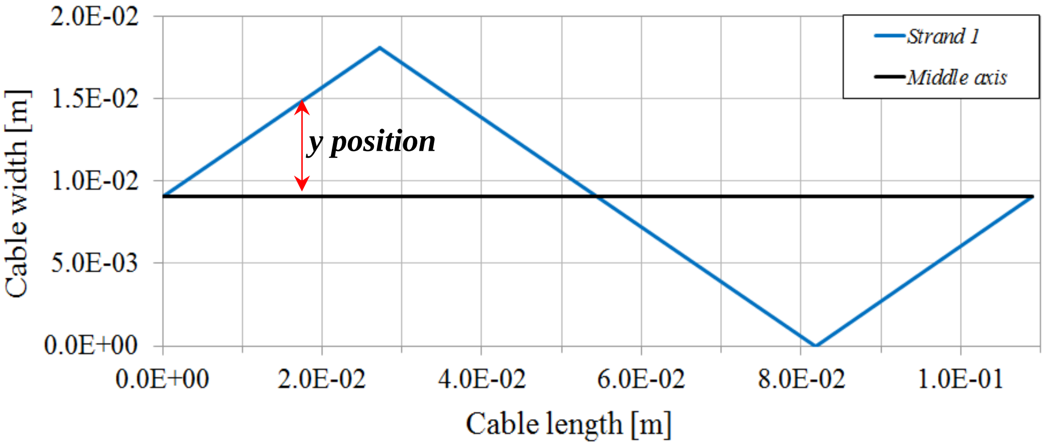

*Fig. 36. y position function for a generic strand.*

### 4.1.2 Conductance calculation

Conductance per unit length is inserted in the code in matrix form, defined as follows:

$$\mathbf{C} = \begin{bmatrix} 0 & \cdots & g_{ij} & \cdots & g_{iN_{strand}} \\ \vdots & & & & \vdots \\ g_{ij} & & \ddots & & g_{ij} \\ \vdots & & & & \vdots \\ g_{N_{strand}j} & \cdots & g_{ij} & \cdots & 0 \end{bmatrix}$$

Where every element of the matrix describes the conductance function between each couple of strands which constitutes the cable. The elements on the main diagonal are zero because they represent the conductance of a strand with itself. The matrix is symmetrical; therefore, the definition of the upper or lower triangle is sufficient.

Excluding the main diagonal, all the elements of this matrix can be divided into 2 categories, depending on the position taken by each pair of strands (see Fig. 37): the elements that describe the conductance functions between two adjacent strands ($g_a$) and the elements that describe the conductance functions between two non-adjacent strands ($g_c$).

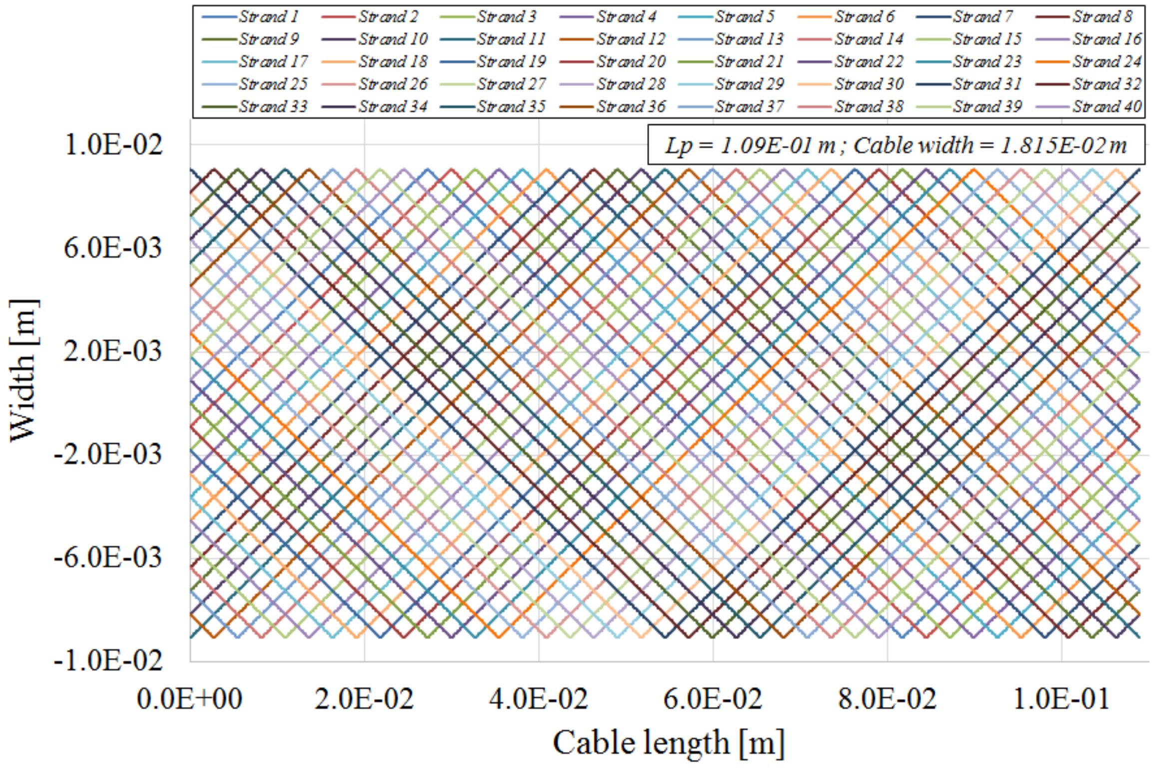

*Fig. 37. 2D representation of a 40 strands Rutherford cable, as derived from the parameters inserted within the code. Following the path of a single strand (a single row of the conductance matrix), it is possible to see that there are 2 strands adjacent to it and 37 strands non-adjacent to it. The width of the individual strand is not provided in the code and for this reason, there are gaps between strands not present in reality: this does not affect the accuracy of the model.*

$g_a$ is a function taken uniform along the cable length, despite it has been explained that the new approach of the continuum model allows the use of a conductance function dependent on the $x$ coordinate. In this case, it is considered that two adjacent strand are constantly in contact with each other along the length of the cable, thus a constant function represents well their electrical connection. For $g_a$ the following formula is used (already described at Chapter 3.1.2) [7]:

$$g_a = \frac{2\,(N-1)}{Lp \cdot Ra}$$

The main difference compared with the first approach of the continuum model is in the form assumed by the function $g_c$. This function is not taken uniform along the cable length, but it varies in order to describe in more detail the electrical contacts in each couple of strands.

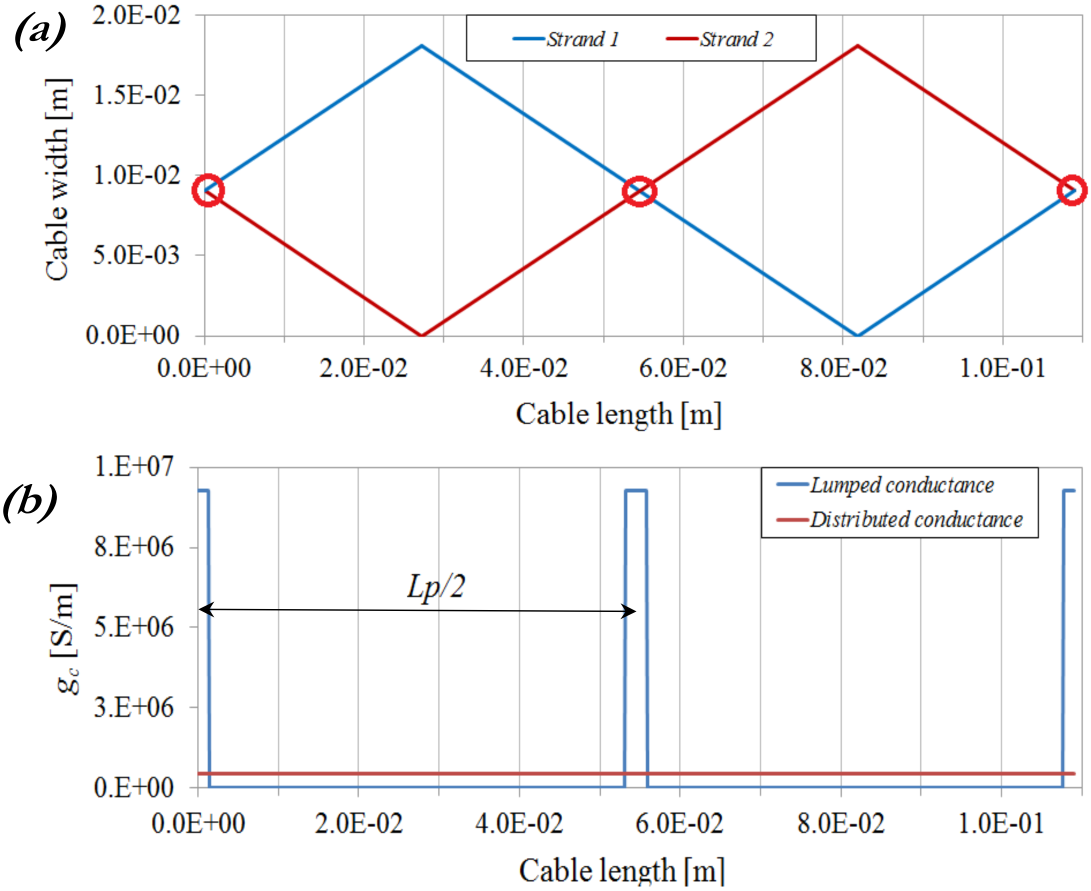

*Fig. 38. Mutual position of two non-adjacent strands (a) and the conductance function that derives from it (b). The red dots in (a) represents contacts between the two strands: the peaks of the conductance function, according to the new approach of the continuum model are positioned in correspondence of these contacts (blue function in (b)). The red function of figure (b) represents the conductance function for the same couple of strands obtained from the first approach of the continuum method.*

The $g_c$ function is written according to this criterion;

$$\begin{cases} g_c \neq 0 & \text{if } x \in \text{interval of contact between the two strands} \\ g_c = 0 & \text{if } x \notin \text{interval of contact between the two strands} \end{cases}$$

Thus, the function profile assumes a trend characterized by peaks (see Fig.38). Each peak is characterized by a longitudinal position of its center, a longitudinal width and a vertical height.

The longitudinal position of the center of each peak depends on the couple of strands considered. It is important to emphasize two features of these functions:

- All functions are equal to each other; a function compared to another is only shifted in the longitudinal position of a certain value (positive or negative) depending on the couple of strands considered each time.
- Within a single function for a generic couple of strands, it is possible to determine a frequency for the appearance of a peak, equal to half of the pitch twist. Indeed each strand crosses every other strand twice per twist pitch; it means that once the longitudinal position of a generic peak is defined all successive or previous peaks are automatically defined simply shifting in the longitudinal position the peak of a value equal to an integer multiple of *Lp/2*.

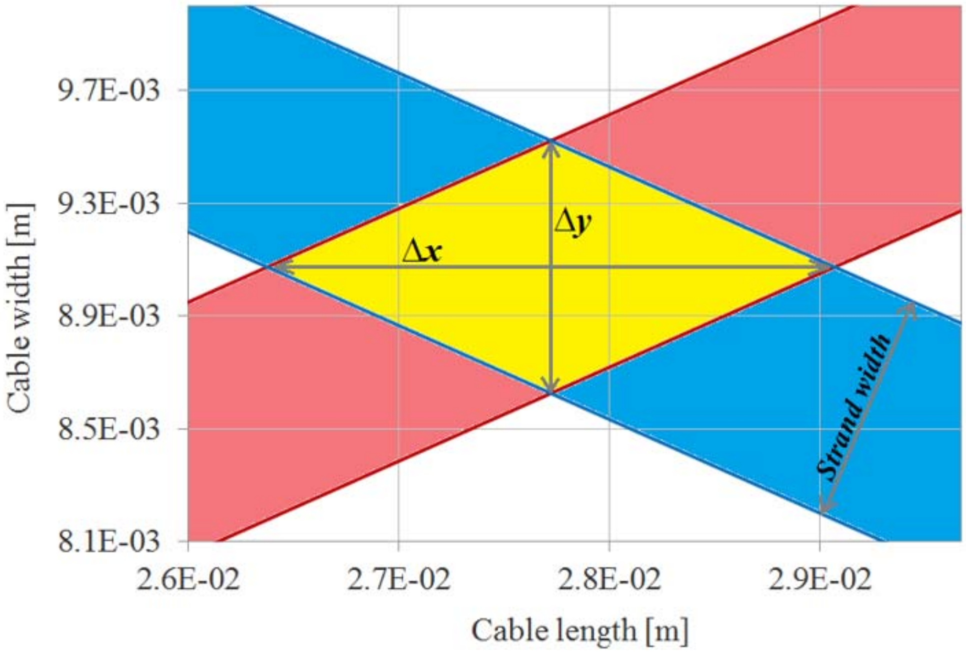

*Fig. 39. Enlargement of the cross-contact point between two non-adjacent strands.*

Referring to Fig. 39, the longitudinal width of a peak of conductance is taken equal to the longitudinal distance $\Delta x$ between the beginning and the end of the contact. This value is fixed for each peaks of every conductance function, once the geometry and the number of strands are given.

The height of the peak of conductance is defined using the following formula, remembering that THEA requires a conductance per unit length as an input:

$$g_c = \frac{\Delta y}{2\,Rc \cdot Contact\ Area}$$

Where:

- $Contact\ Area = \frac{\Delta x \cdot \Delta y}{2}$ .
- $\Delta y$ and $\Delta x$ are described in Fig. 39.
- *Rc* is the electrical resistance between non-adjacent strands.

It is necessary to report the considerations made about the setting of the minimum conductance value: ideally, the conductance value in points which do not belong to the interval of contact between the two strands should be zero, but this is not possible in THEA due to the appearance of an error message. Initially, to solve this problem the minimum conductance value is set equal to a small value (1.0E-10 S/m) slightly greater than zero; despite this expedient allows the program to run, simulations were however incorrect. Finally, the necessity to keep the minimum conductance value near to the maximum conductance value (the height of the peak) is deduced, to not create problems in the process of inversion of the conductance matrix. In conclusion, it is decided to set a compromise value of the minimum conductance equal to the maximum conductance value multiplied by 1.0E-5.

#### *4.1.2.1 Profile of longitudinal conductance*

The so-described profile have rectangular peaks; it is noticed that this leads to undesired numerical errors due to the presence of discontinuities of the first type in correspondence of the starting and ending points of each contact (Fig. 40). To solve this problem different profiles of conductance function are tested, keeping always in mind this criterion: whichever is the shape of the peaks the area under these curves must always remain the same.

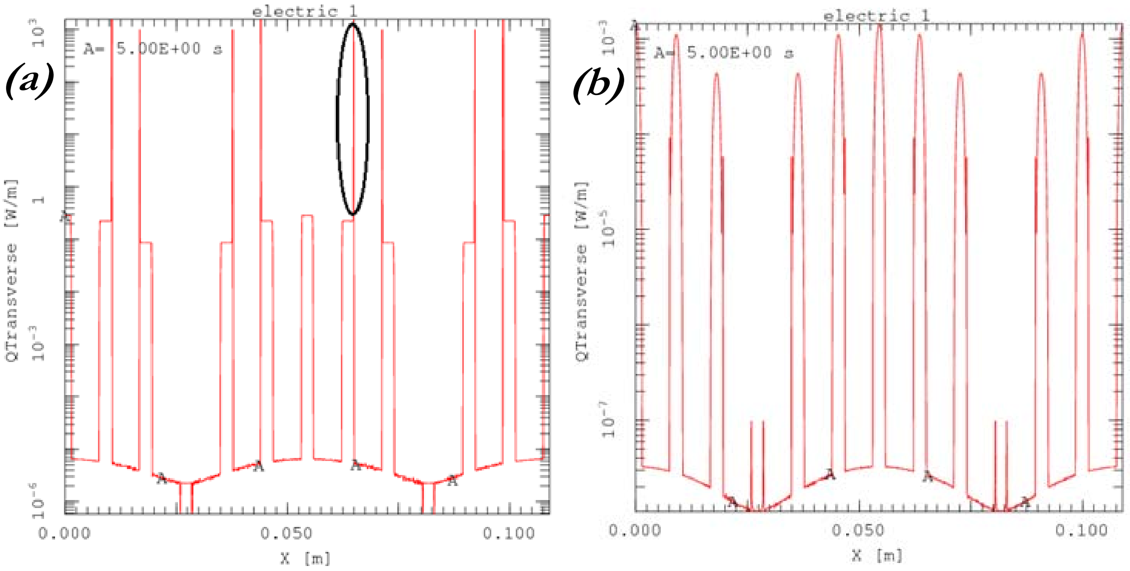

*Fig. 40. (a) Plot for losses due to ISCCs relative to the x position (using THEAPOST software) for strand number 1 considering a rectangular profile with the highlight of a numerical error. (b) Same plot considering the Gaussian profile: the error are consistently reduced.*

Five types of profiles for longitudinal conductance are analysed (see Fig. 41 for an graphic explanation):

- Rectangular (*Profile A*).
- Trapezoidal (inside the peak, the conductance starts from the minimum conductance value and goes up to the maximum value following the side of an isosceles trapezium). The smaller base at the top has the size of 1/5 of the total width of the peak (*Profile B*).
- Trapezoidal (same concept of *Profile B*) but with the smaller base at the top with the size of 3/5 of the total width of the peak (*Profile C*).
- Trapezoidal as Profile C. with sides that are not straight but smoothed using parabolic sections (*Profile D*).
- Gaussian (*Profile E*). It is constituted by three different parabolic sections to smooth as much as possible conductance discontinuities. Due to its higher complexity, this profile has an area under its peaks which differs of 0.8% compared the one under a rectangular peak (taken as reference). Despite that, this is the shape which reduces as much as possible the problems mentioned above.

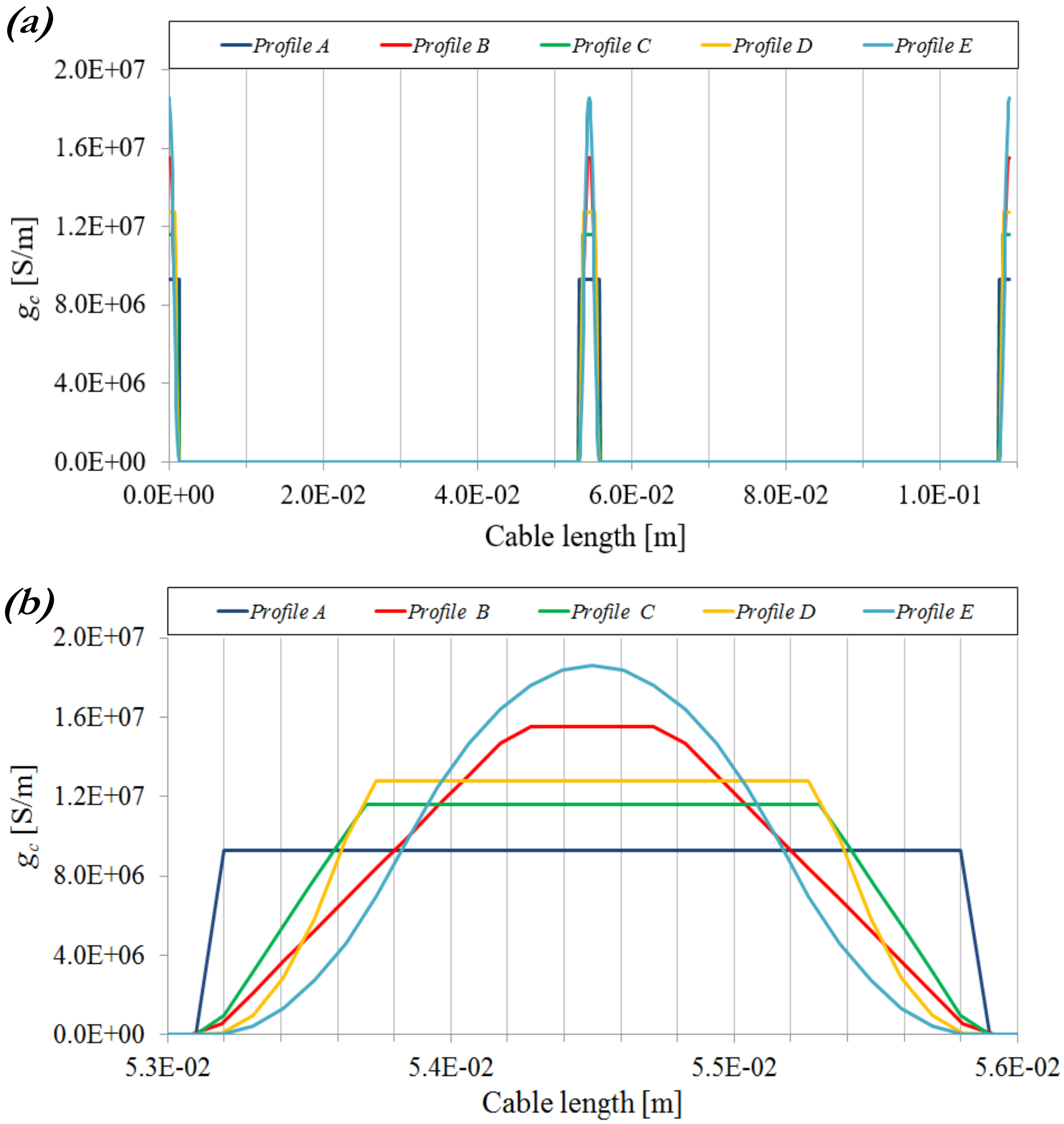

*Fig. 41. (a) Plot of conductance function between two generic strands varying the profile of the peaks (only one twist pitch is considered). (b) Enlargement of the central peak too clarify geometry. Names present in legends are described above.*

## *4.1.3 Inductance calculation*

Inductance per unit length is inserted in the code in matrix form, defined as follows:

$$\mathbf{L} = \begin{bmatrix} l_{ij} & \cdots & l_{iN_{strand}} \\ \vdots & \ddots & \vdots \\ l_{N_{strand}j} & \cdots & l_{N_{strand}N_{strand}} \end{bmatrix}$$

Where $l_{ij}$ is a self-inductance if $i = j$ or a mutual-inductance if $i \neq j$.

The calculation of the inductance in circuits made up of straight elements of negligible cross section is analysed in detail in [38]. For this discussion it will be sufficient to know that when the dimension of the cross-section of the conductors of a circuit composed of straight elements is negligible compared with the distances between the elements, the mutual inductances of elements can be reasonably approximated by those of their central filaments [30].

The self-inductance is defined by the following expression, derived starting from the general formula and neglecting the ratio between the arithmetic mean distance of the points of the cross-section and the cable length [1]:

$$l_{ij} = \frac{\mu_0}{2\pi}\left[ln\left(\frac{2L_i}{\rho_i} - \frac{3}{4}\right)\right] \qquad \text{for } i = j$$

The mutual inductance is defined through the following formula for two parallel straight filaments [1]:

$$l_{ij} = \frac{\mu_0}{2\pi}\left[ln\left(\frac{L_i}{d_{ij}} + \sqrt{1+\frac{L_i^2}{d_{ij}^2}}\right) - \sqrt{1+\frac{L_i^2}{d_{ij}^2}} + \frac{d_{ij}}{L_i}\right] \qquad \text{for } i \neq j$$

Where, for both equations:

- $\mu_0$ is the vacuum permeability.
- $L_i$ is the strand length, equal to three times the value of the twist pitch.
- $\rho_i$ is the strand radius.
- $d_{ij}$ is the distance between the $i^{th}$ and $j^{th}$ strands, given by the following formula [1]:

$$d_{ij} = \sqrt{(x_i - x_j)^2 + (y_i - y_j)^2}$$

$x_i$ and $y_i$ represent the coordinates of the central filament of each strand in the cable cross-section, with respect to fixed reference system (see Fig.42). If a multistrand cable is considered their value is derived by [1]:

$$\begin{cases} x_i = 2\rho\,(i-1) \quad \text{and} \quad y_i = 2\rho & \text{if } i \le \dfrac{N}{2} \\ x_i = 2\rho\,(N-i) \quad \text{and} \quad y_i = 0 & \text{if } i \ge \dfrac{N}{2} \end{cases}$$

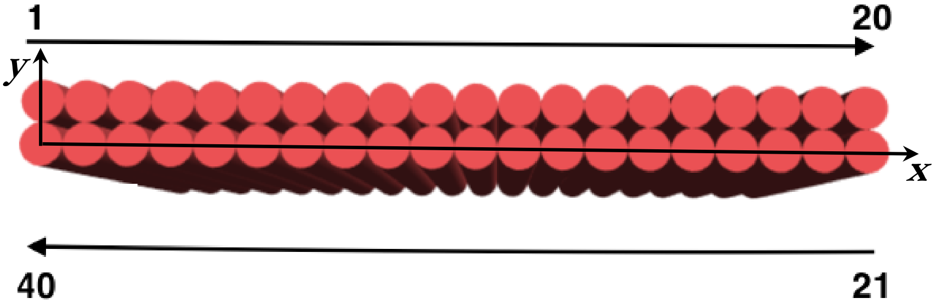

*Fig. 42. Cross section of a 40 strands Rutherford cables with the strand numeration and the reference system used for the inductance calculation.*

A numerical calculation of the inductance between two strands $i$ and $j$ of a volume $V_i$ and $V_j$ is fully treated in [39].

## 4.2 Validation via analytical formulae

The model is validated comparing results obtained through simulations with the ones calculated using analytical formulae available in literature [13 - 42]:

$$\mathrm{P} = \frac{N^2 \cdot w^2 \cdot Lp^2}{120 \cdot Rc} \cdot \left(\frac{dB^2}{dt}\right)$$

Where:

- P is the coupling loss per cable's twist pitch.
- $N$ is the number of strands.
- $w$ is the cable width,
- $Lp$ is the cable twist pitch
- $Rc$ is the cross-contact resistance

Note that this formula considers negligible the resistance, and thus the losses, between adjacent strands. Despite this assumption is true for all practical cases, a study will be presented in which losses between adjacent strands are not negligible: in this case to another analytic will be used to validate the model.
Since the analytical formulae refer to losses per unit of twist pitch, a cable of a length equal to a single twist pitch is considered, so that the losses calculated are immediately comparable with those deduced by the analytical formulae. For completeness, simulations are realized with longer cables (considering the same boundary conditions) focusing on a section of the cable equal to the twist pitch length placed at the cable center, ensuring that losses in this section remain in agreement. The choice of the boundary conditions is relevant to these considerations and it will be discussed later in this chapter.

### 4.2.1 The baseline study case

A $Nb_3Sn$ Rutherford cable developed to be placed in new low-β quadrupoles magnets (*MQXF*) for the High-Luminosity project of LHC is considered as reference to make comparisons between analytical results and simulation results [12]. Table 3 reports the characteristics of this cable and the magnetic field conditions.

| *Cable data* | | |
|---|---|---|
| Number of strands | [/] | 40 |
| Twist Pitch | [m] | $1.09 \cdot 10^{-1}$ |
| Cable width | [m] | $1.82 \cdot 10^{-2}$ |
| Strand diameter | [m] | $8.5 \cdot 10^{-4}$ |
| Cable length | [m] | 1 twist pitch |
| *Rc* | [Ω] | $4.0 \cdot 10^{-5}$ |
| *Ra* | [Ω] | $3.2 \cdot 10^{-4}$ |
| *Operating conditions* | | |
| *dB/dt* | [T/s] | 0.05 |

*Table 3. Main characteristic of the baseline study case used as reference.*

To validate the model, all parameters are varied both in simulation and in the analytical formula, then the results compared. Hereafter, the comparison between numerical and analytical results will be expressed as a percentage called $\varepsilon$ (reported in charts on the ordinate axis), calculated by the following formula:

$$\varepsilon = \text{abs}\left(\frac{\textit{Analytical result} - \textit{Simulation result}}{\textit{Analytical result}}\right)\cdot 100$$

Where *Simulation result* is the result obtained with the combined use of the software THEA and THEAPOST [11]. THEAPOST allows obtaining values of the variable called *QTransverse* as a function of the longitudinal position. This function represents the power per unit length produced by the currents flowing transversely to each electric element equivalent to the interstrand coupling currents. Then, functions are integrated in space to obtain the value of total losses along the length of the cable. The integration is perfomed using the trapezoidal rule as integration method, which is preferred to the Simpson rule.

The function *QTransverse* is obtained through THEPOST for single strands: to get the total value of losses for the entire cable, two method are analysed:

- *Method A*: total losses are calculated by multiplying the losses relating to the generic strand 1, for the number of strands constituting the cable. This method implies that losses are well balanced across all strands, and it allows to reduce calculations.

- *Method B*: losses are calculated for each strands and them summed. This method is more accurate but requires more computation time.

### *4.2.2 Convergence studies*

Convergence is studied in terms of minimum number of mesh elements used for simulations, needed to reach accordance between analytical and simulation results. If a difference (expressed through the $\varepsilon$ parameter) of less than 1% is assumed acceptable to reach convergence, a number of mesh elements between 250 and 300 per twist pitch needs to be considered for simulations (See Fig. 43). This value is the same for both *Method A* and *Method B*.

From Fig. 42 it is possible to see that when the number of elements is low, the difference between losses calculated using the faster *Method A* or the more time spending *Method B* increases. This is probably due to a decrease of accuracy of the software interpreting the real trend of the conductance function, whence the appearance of imbalances between strands. However, when the convergence is achieved, results are the same for both methods: results presented in this work are therefore calculated with the time-saving *Method A*, unless differently specified.

Once the minimum number of elements is established, it should be noted that higher is the number of elements and higher is the overhead of the continuum model compared to the network model. Whereas a number of mesh elements equal to 250, the overhead compared to the network model that simulates a 40 strands cable is "limited" to a factor equal to 250/40 ≈ 6: 6 continuous elements for each network ashlar. Higher is the number of elements and higher is the level of detail of the simulation compared to the network model. For this reason, the simulations are carried out (unless otherwise specified) with a number of mesh elements equal to 1000, to ensure an optimal level of detail.

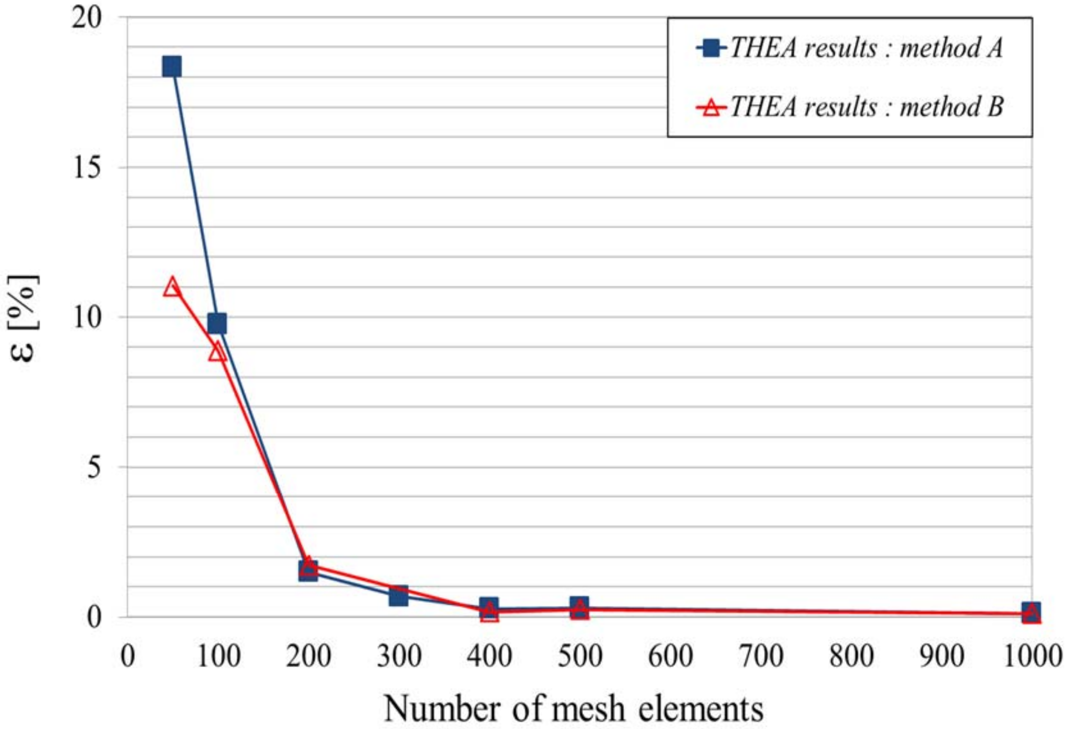

*Fig. 43. Variations between analytical and numerical results by changing the number of mesh elements in the simulations. Simulation results are calculated using two different methods.*

### *4.2.3 Parametric studies*

In this section, the comparisons between losses obtained via analytic formula and simulations are reported, modifying each time one single parameter from the baseline study case. Unless specified otherwise, all parameters that are not described as variables are maintained with the values reported in Table 3.

Unless differently specified, graphs in which losses appear are in a semi-logarithmic scale, while those in which the $\varepsilon$ parameter appears are displayed in normal scale.

- *Impact of* $\frac{dB}{dt}$ *:*

**(a)**

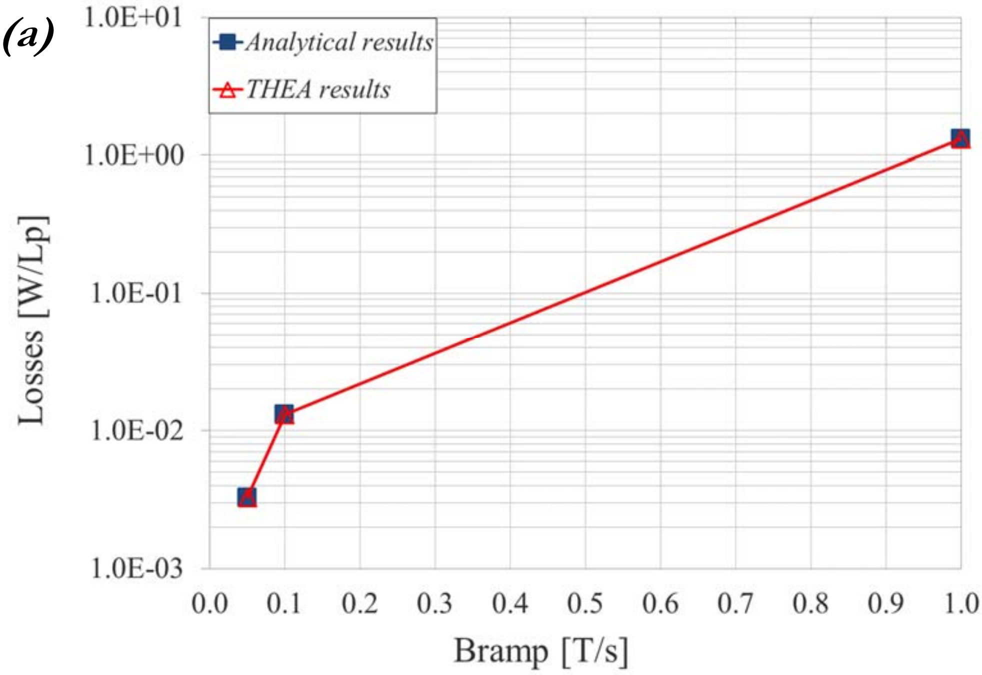

**(b)**

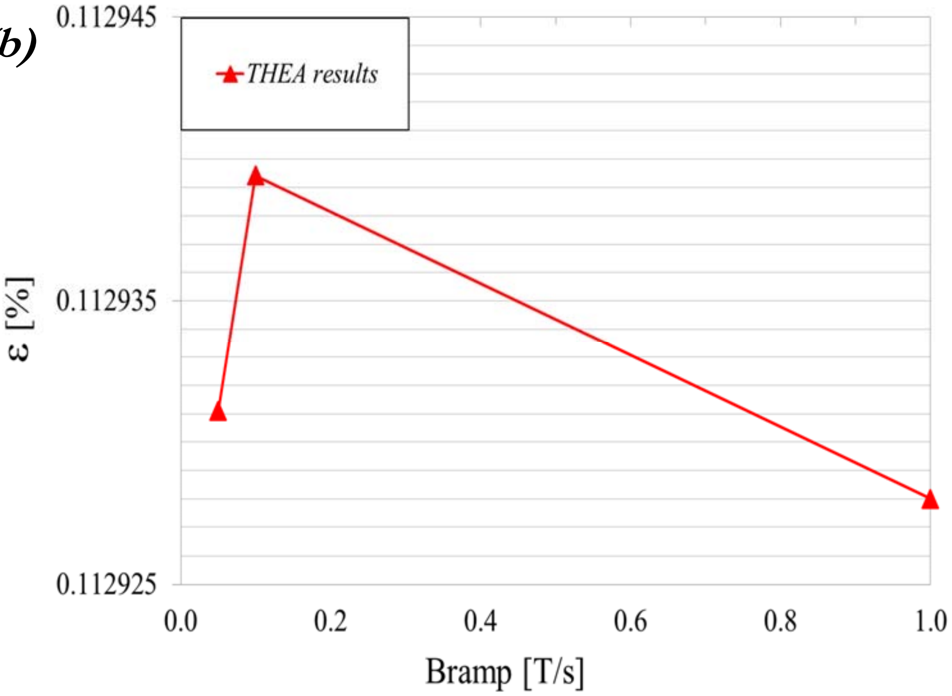

*Fig. 44. (a) Simulation results for losses varying the magnetic field ramp rate; (b) variation between numerical and analytical results.*

Fig. 44 (a) shows that steeper is the magnetic field ramp rate considered and higher are the losses. Moreover, the curve deducted using THEA is superimposed to the one derived analytically.

The comparison between results is presented in Fig. 44 (b): the $\varepsilon$ parameter remains very limited and therefore concordance between simulations and analytical results is verified for magnetic field rate parameter.

- *Impact of the cable width:*

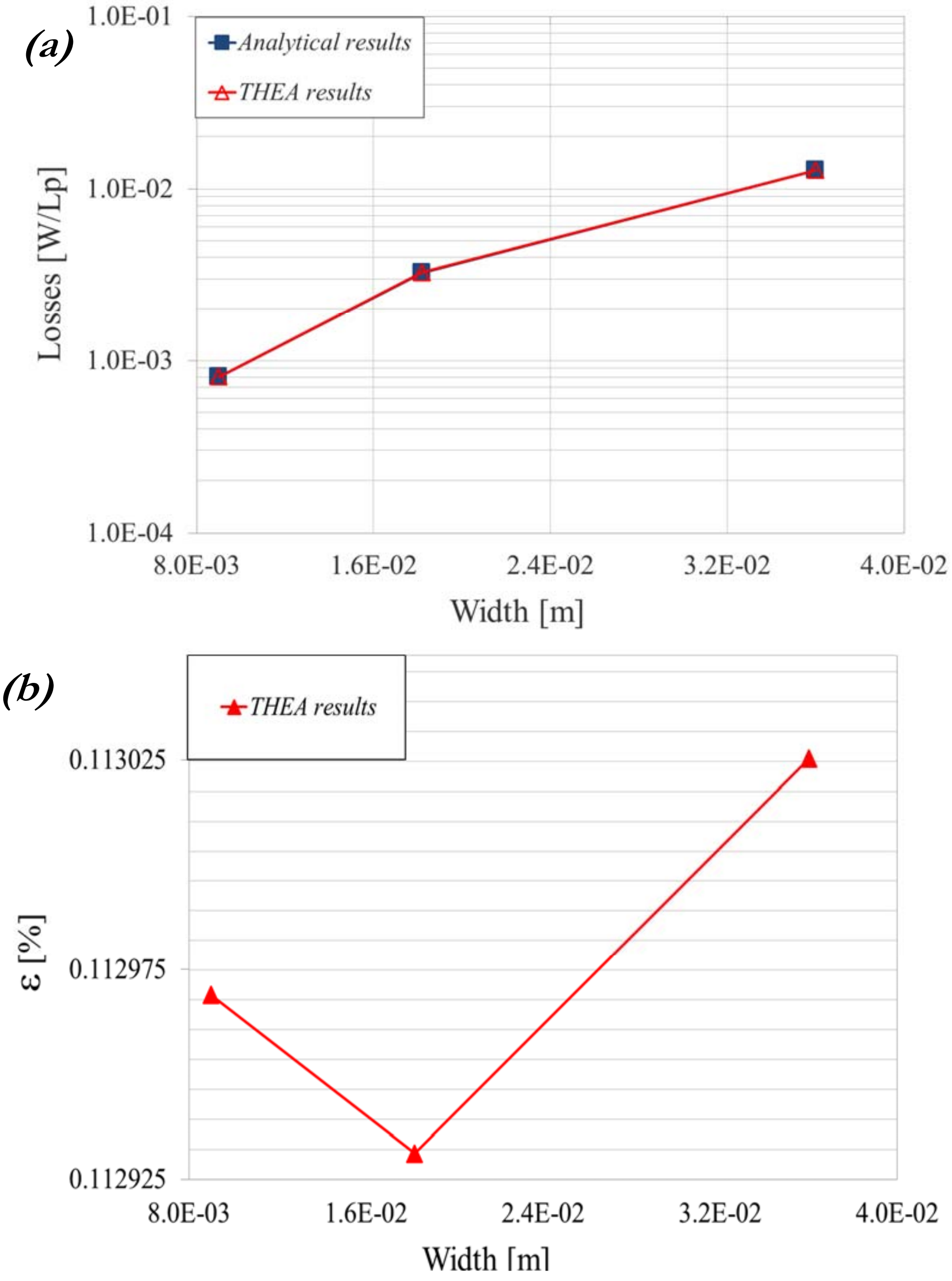

*Fig. 45. (a) Simulation results for losses varying the cable width; (b) variation between numerical and analytical results.*

Fig. 45 (a) shows that larger is the width of the cable and higher are the losses. Moreover, the curve deducted using THEA is superimposed to the one derived analytically.

The comparison between results is presented in Fig. 45 (b): the $\varepsilon$ parameter remains very limited and therefore concordance between simulations and analytical results is verified for the cable width parameter.

- *Impact of the twist pitch length:*

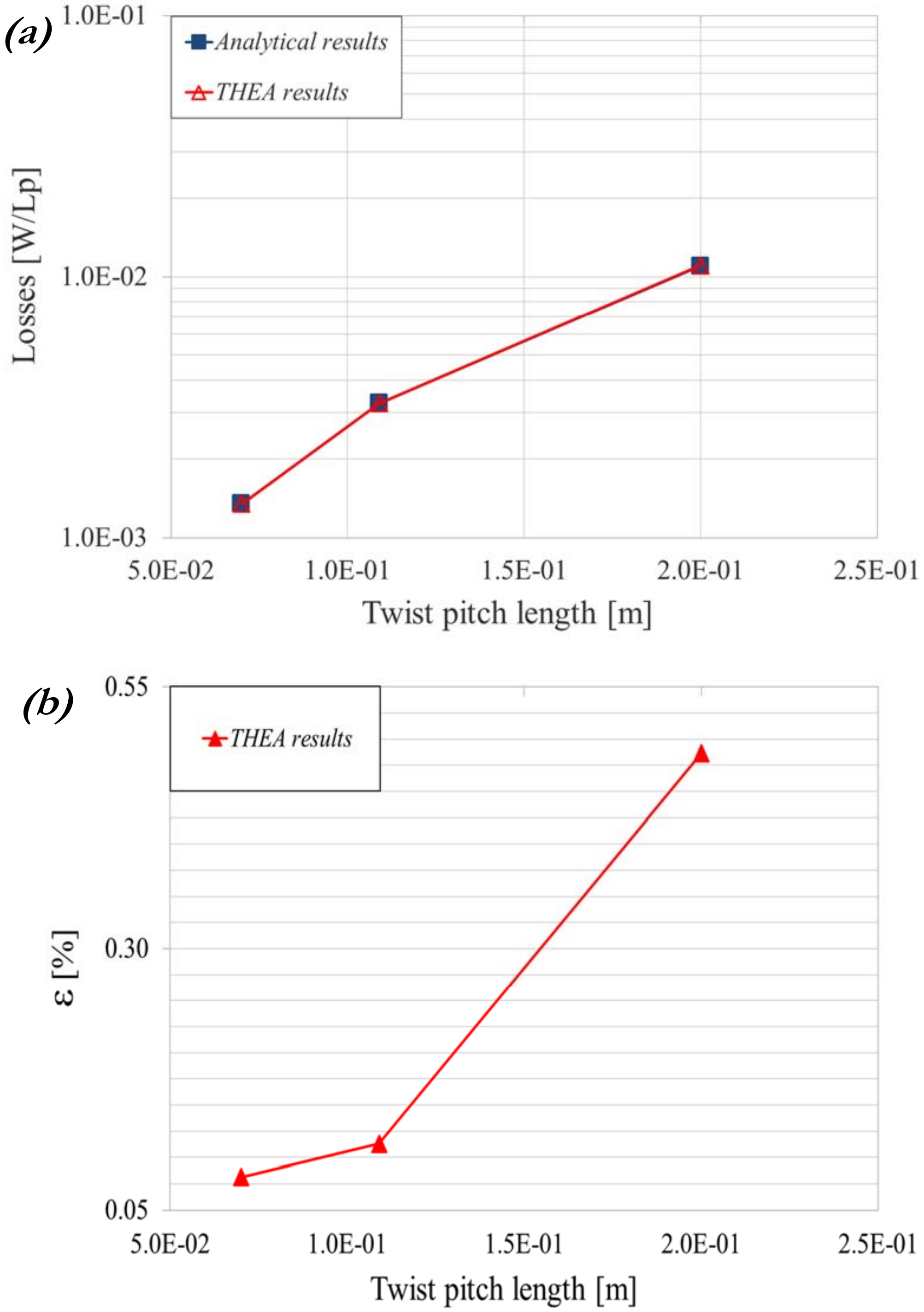

*Fig. 46. (a) Simulation results for losses varying the cable twist pitch; (b) variation between numerical and analytical results.*

Fig. 46 (a) shows that larger is the cable twist pitch and higher are the losses. Moreover, the curve deducted using THEA is superimposed to the one derived analytically.

The comparison between results is presented in Fig. 46 (b): the $\varepsilon$ parameter remains very limited and therefore concordance between simulations and analytical results is verified for the cable twist pitch parameter.

For clarification, when the twist pitch length is doubled compared to the baseline study case, the term $\varepsilon$ quadruples (remaining within the limits of convergence): this is mainly due to the fact that the number of mesh elements is not changed in accordance with the increase in length, thus a tolerable decrease in results precision is expected.

- *Impact of the profile of longitudinal conductance:*

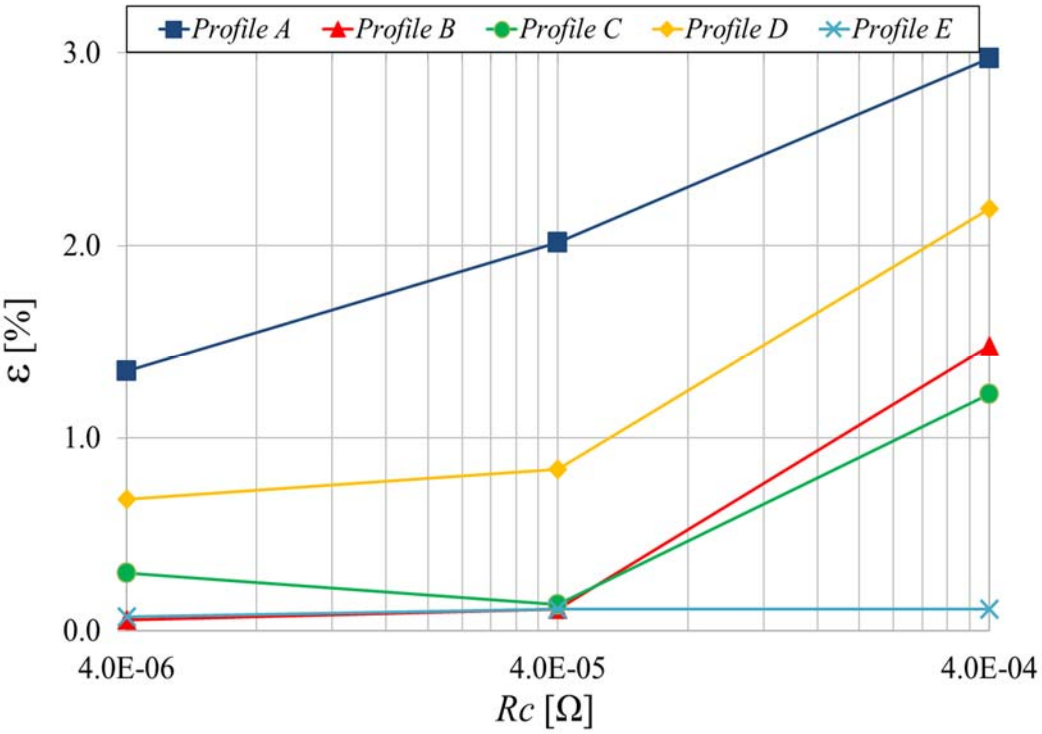

*Fig. 47. Variation between analytical numerical results for different Rc, varying the profile of the peaks in conductance functions. For an explanation of the legend, see Chapter 4.1.2.1.*

As already seen in Chapter 4.1.2.1 , different profiles of the longitudinal conductance function are investigated, in substitution of the basic rectangular shape, which give rise to some problems. This study is realized to find the profile that reduces more the difference between simulations and analytical results.

The comparison are performed by comparing results for losses for different conductance functions, varying a parameter arbitrarily chosen. For example in Fig. 47, the Rc value is changed.

As it is possible to see, the Gaussian shape (*Profile E*, in light blue) is the one which returns the best results; other profiles are acceptable to achieve convergence, with the exception of the Rectangular shape (*Profile A*, in dark blue) which leads to variations up to 2%. Other tests are executed modifying other parameters rather than *Rc*, which all lead to the same conclusion.

- *Impact of Rc:*

From Fig. 48 two different behaviours can be inferred: when *Rc* is higher than the study case, analytical and numerical results are in agreement, while they diverge consistently when *Rc* values are smaller compared to the study case; for this last case even the difference between the solution computed by *Method A* and *Method B* increases.
This phenomenon is due to the fact that, when *Rc* is very low, the time constant of the RL circuit becomes very large, up to values that need longer time of simulation to reach the steady state condition. The results reported previously are all realized with simulation *End Time* equal to 3 seconds, not sufficient to achieve steady state conditions.

In Fig. 49 there is a comparison between currents trends for different simulation *End Times*, considering *Rc* 1000 times smaller than the baseline study case. In simulations for 3 seconds (Fig. 47 (a)) currents do not reach the steady state, which is instead achieved with simulations up to 30 seconds.

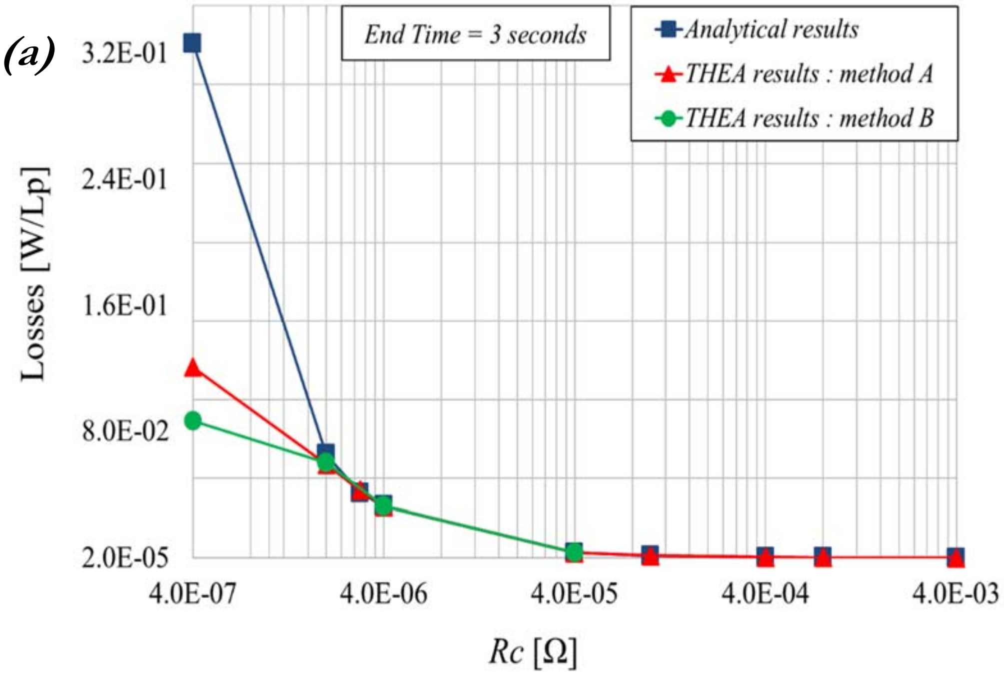

*Fig. 48. (a) Simulation results for losses varying Rc for simulation End Time of 3 seconds. This chart is in semi-logarithmic scale.*

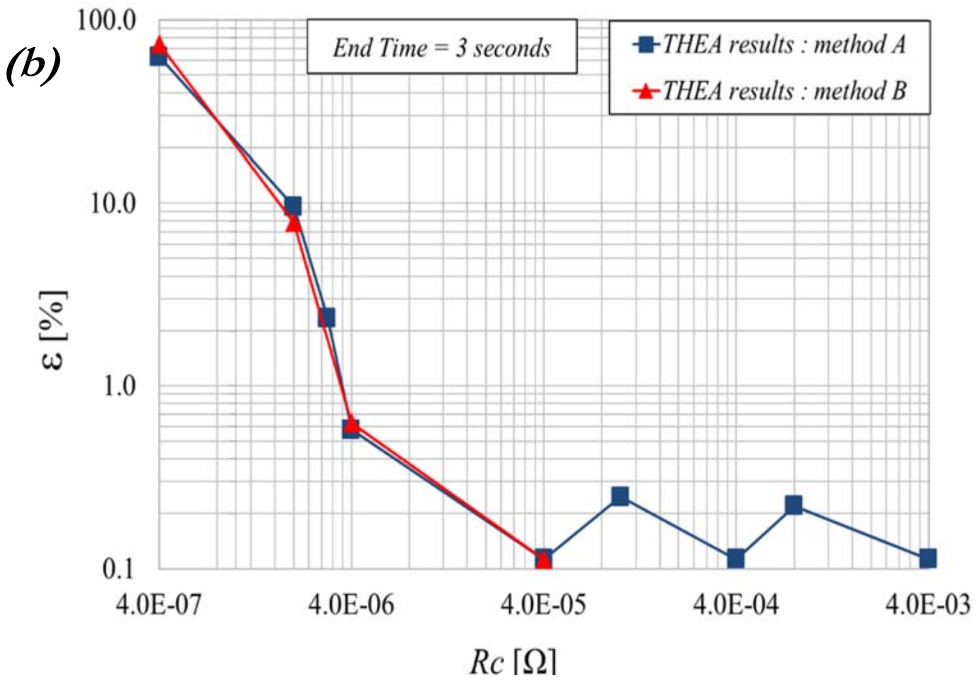

*Fig. 48. (b) Variation between numerical and analytical results. For this chart both axis are in logarithmic scale.*

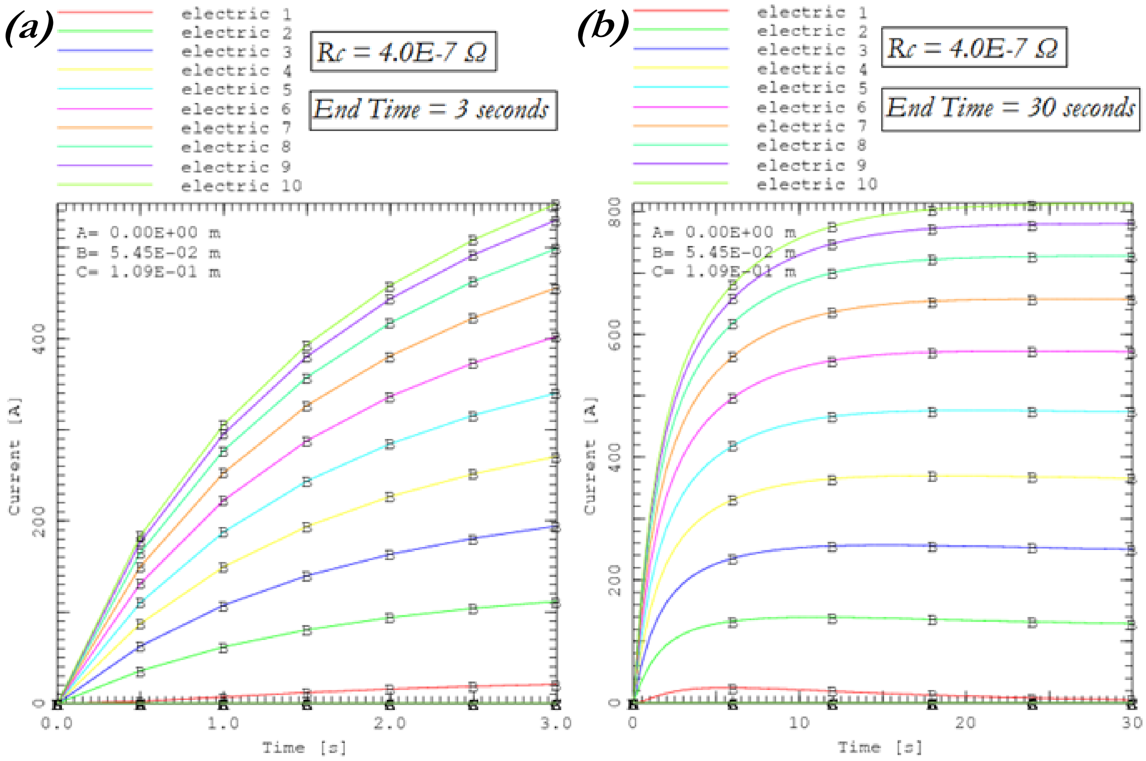

*Fig. 49. Short-range coupling currents depending on time, for the first 10 strands of a 40 strands cable with Rc equal to $4.0 \cdot 10^{-7}$ Ω, for simulations with End Time of 3 seconds (a) and 30 seconds (b). Results are displayed for 3 different cable positions: cable begin (A), middle of the cable (B) and cable end (C); due to boundary conditions all points of curves A and C remains equal to zero.*

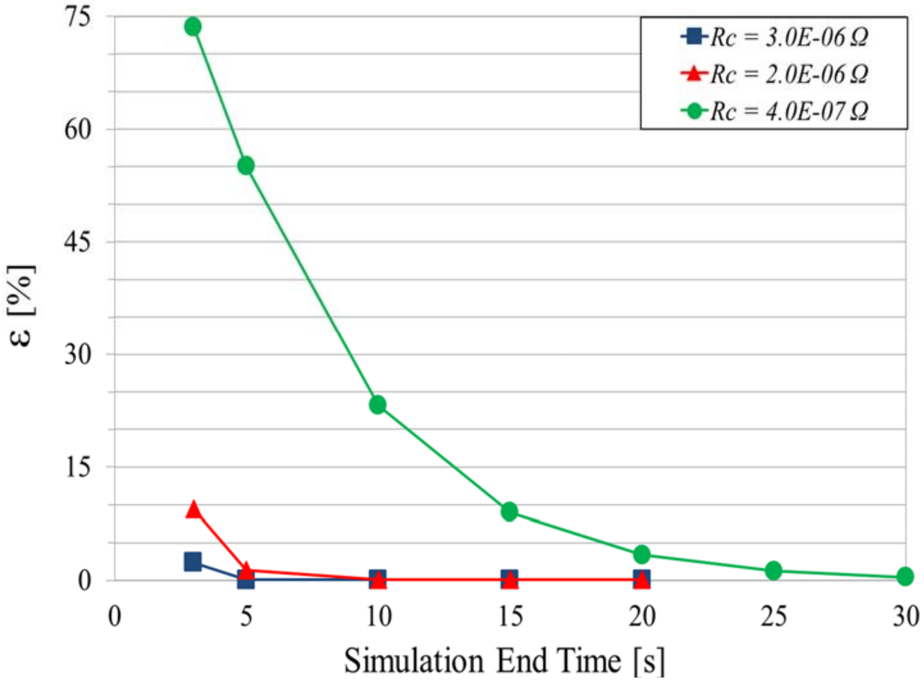

*Fig. 50. Variation between numerical and analytical results varying the simulation End Time, for cable with different Rc (values still much smaller than the baseline study case).*

As it is possible to see from Fig. 50, for *Rc* equal to 4. $\cdot 10^{-7}$ (green curve), an *End Time* equal to (or greater than) 30 seconds is required to reach convergence. Increasing the *Rc* value shorter simulations are sufficient.

However, higher *End Time* however means greater computational time: it is therefore preferable to adjust the *End Time* value in accord with the change of *Rc*.

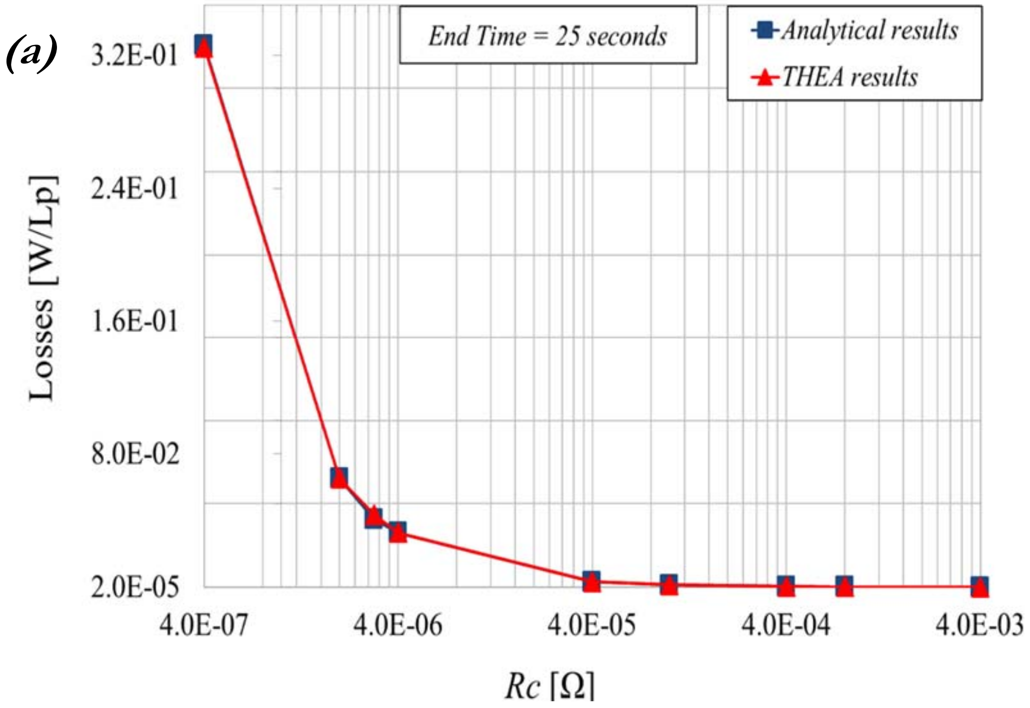

*Fig. 51. (a) Simulation results for losses varying Rc, with simulation End Time equal to 30 seconds.*

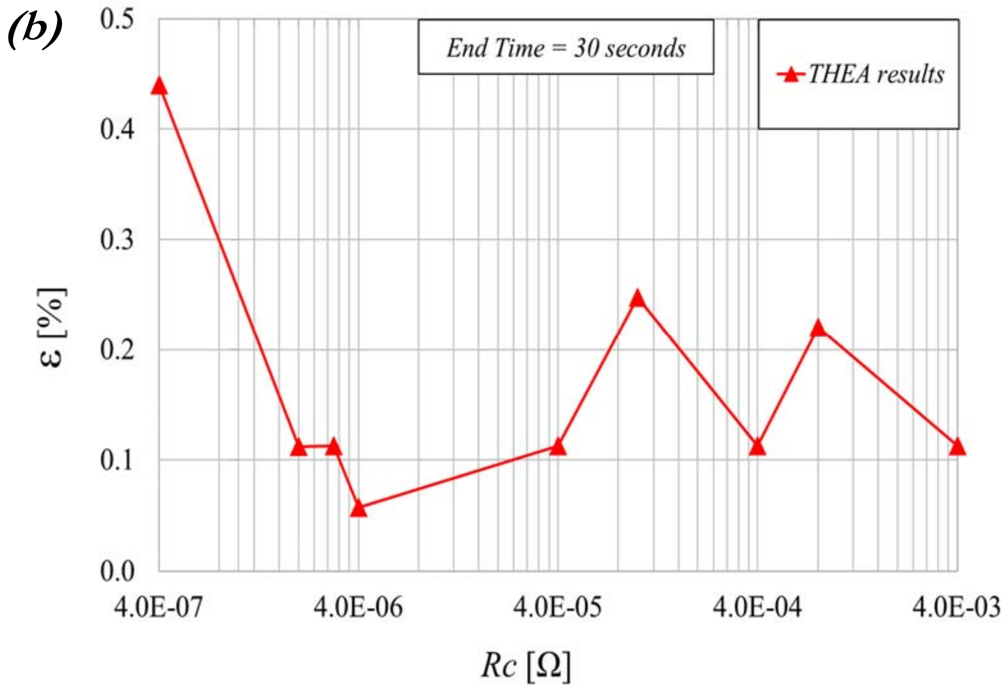

*Fig. 51. (b) Variation between numerical and analytical results, with simulation End Time equal to 30 seconds.*

Given that, to compare analytical and numerical results varying *Rc*, simulations are repeated considering a sufficient simulation *End Time* to achieve convergence. Fig. 51 (a) shows that lower is *Rc* and higher are the losses. Moreover, the curve deducted using THEA is superimposed to the one derived analytically.

The comparison between results is presented in Fig. 51 (b): the *ε* parameter remains very limited and therefore concordance between simulations and analytical results is verified for the *Rc* value, provided an appropriate simulation *End Time* is considered.

- ### *Impact of the Ra:*

For this study, a different analytical formula is considered to investigate the convergence between simulations and analytical results. In fact, Ra is not present in the formula introduced previously, because the losses due to contacts between adjacent strands are considered negligible compared to losses between non-adjacent strands. This assumption cannot longer be true if Rc is kept constant while Ra is varied: in some ranges of Ra, losses between adjacent strands can rise consistently and no longer be negligible. It is therefore necessary to consider the following formula [41]:

$$\mathrm{P} = \mathrm{P}\perp + \mathrm{P}\parallel = \frac{w^2\,Lp^2}{6}\left(\frac{dB^2}{dt}\right)\left(\frac{N^2}{20Rc} + \frac{1}{Ra}\right)$$

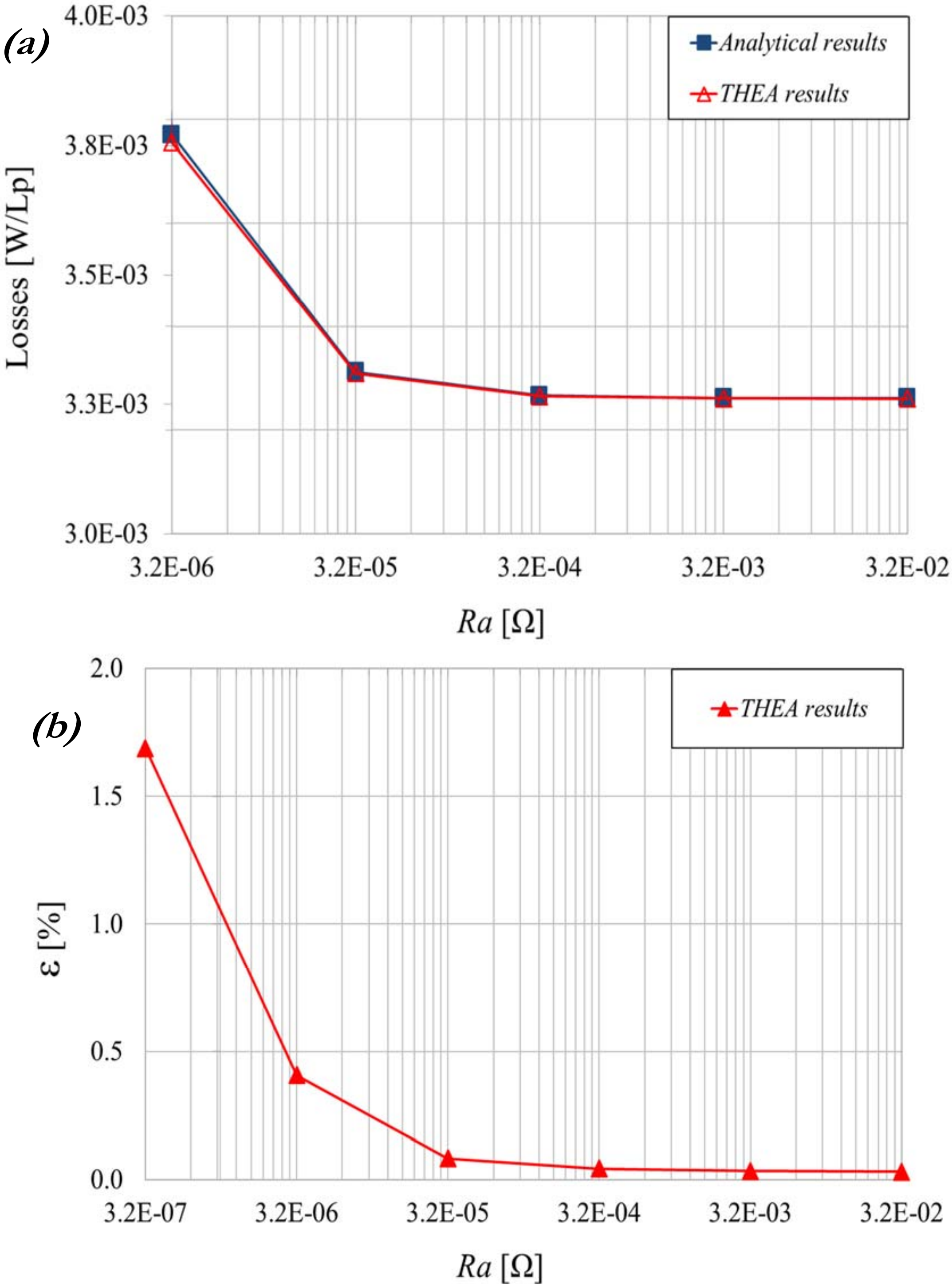

*Fig. 52. (a) Simulation results for losses, varying Ra; (b) variation between numerical and analytical results. Both charts are in semi-logarithmic scale.*

Indeed, the analytical formula reported in literature is slightly different from the above expression: in the formulation resistance *Ra* should be multiplied by *N* (total number of strands) in correspondence of the denominator of the second term between brackets. However, Ra values introduced in THEA code are discretized on an interval equal to *Lp/2N* [12]; this means that the multiplication by *N* is already implicitly contained in the *Ra* value, hence the reason for the absence of multiplication.

Fig. 52 (a) shows that lower is *Ra* and higher are the losses. Moreover, the curve deducted using THEA is superimposed to the one derived analytically.

The comparison between results is presented in Fig. 52 (b): the $\varepsilon$ parameter remains very limited and therefore concordance between simulations and analytical results is verified for the Ra parameter.

### *4.2.4 Dependence of losses on Rc and Ra*

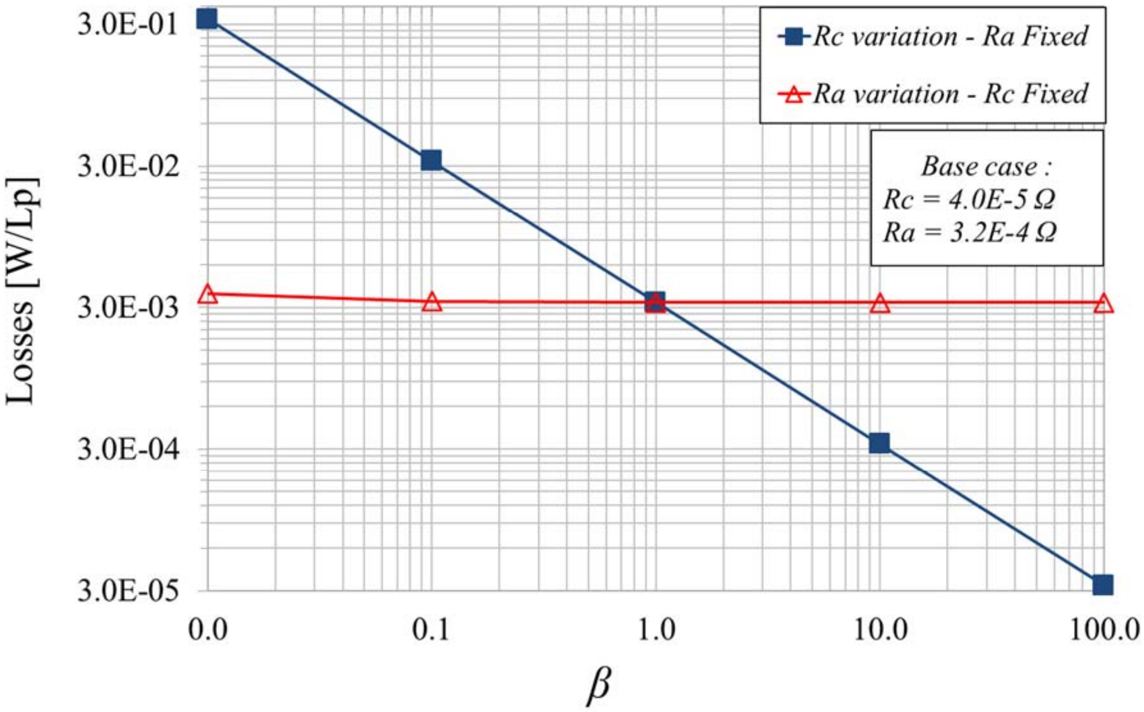

*Fig. 53. Simulation results for losses, varying Rc keeping Ra fixed (blue curve) and varying Ra keeping Rc fixed (red curve).*

Having clarified that losses due to interstrand coupling currents are function of the electric resistances between strands, it is investigated whether losses depend more from *Rc* value or from *R*a value. Therefore, two studies were carried out changing *Ra* or *Rc* singularly: in a first study *Rc* is kept fixed and *Ra* is varied and in a second case *Ra* is maintained fixed and *Rc* varied (see Fig. 53). In order to compare these two experiments, results are graded on the longitudinal axis taking into account the adimensional factor $\beta$, which represents the number for which the value of *Ra* or *Rc* is multiplied or divided each time (while the other value, *Rc* or *Ra*, is kept fixed).

$$\beta = \frac{R_{Varied}}{R_{BaseCase}}$$

Where:

- $R_{Varied}$ = value of *Rc* or *Ra*, varied in each simulation.
- $R_{BaseCase}$ = the value of the other resistance (*Rc* or *Ra*) which is kept equal to the baseline study case ($Rc = 4.0 \cdot 10^{-5}\ \Omega$ and $Ra = 3.2 \cdot 10^{-4}\ \Omega$)

Two conclusion can be deducted by curves reported in Fig. 53: if *Ra* is varied maintaining fixed *Rc* (red curve) the value of losses does not change significantly from one simulation to the other; on the other hand, if *Rc* is varied maintaining *Ra* fixed significant variations are displayed (losses increase or decrease proportionally with $\beta$: when $\beta$ is equal to 10 losses are 10 times larger than the baseline study case, when $\beta$ is equal to 0.1 losses are 10 time smaller than the study case and so on).
Therefore, losses depend more on the value of the resistance *Rc* rather than on the *Ra* value, or rather, that the contribution of losses between non-adjacent strands is significantly more important compared to losses between adjacent strands.

Finally, agreement is demonstrated between analytical results and those obtained through simulations, varying all parameters involved; thus, it is possible to conclude that the method implemented by the simulations is validated for the study of losses in Rutherford cables due to induced coupling currents. This method can be applied to simulate losses for every cable geometries, electrical contact resistances and variations of the external magnetic field.

Furthermore, this electric model can be coupled with the thermo-hydraulic model already implemented in THEA, for a more comprehensive study of transients.

## 4.3 Results

Simulations are performed using parameters of the baseline study case, changing only the length of the cable where specified. Distributions of short-range coupling currents (Fig.54 - 55) and losses (Fig. 56-58) induced in each strand by a time-varying magnetic field are presented. Results are display along the cable length and the cable width.

Fig. 54 shows that currents return equal to zero every twist pitch along the cable length; this is due to the definition of the induced voltage functions.

Fig. 55 represent the same current, displayed on the cable width. For each strand, currents assume their maximum absolute values at cable sides, while at the cable center currents assume their minimum value.

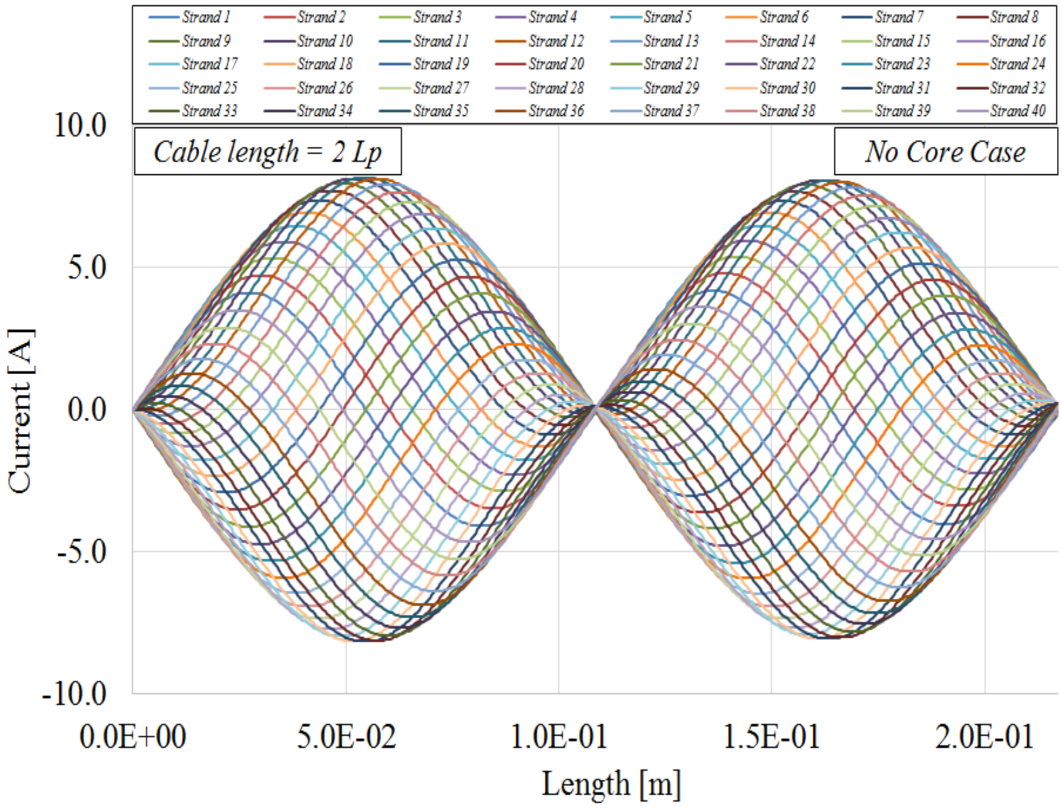

*Fig. 54. Induced coupling currents distribution along the cable length, for a 40 strand Rutherford cable, considering a cable length of two twist pitches.*

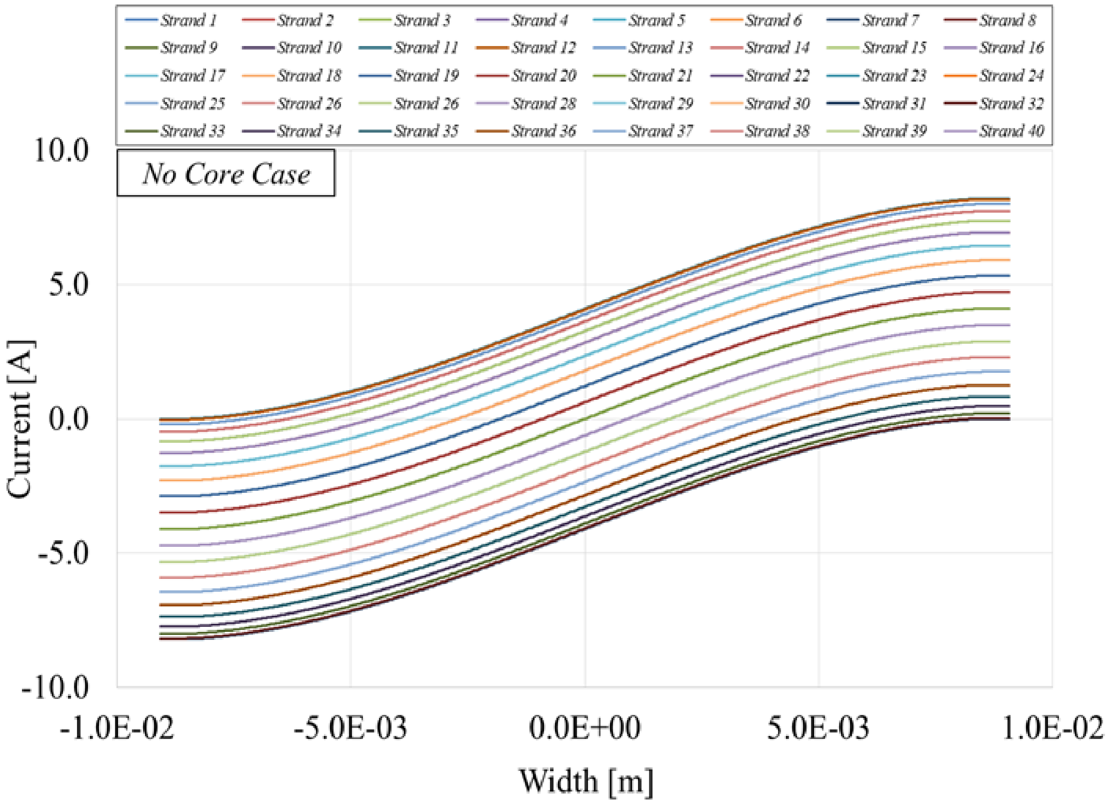

*Fig. 55. Induced coupling currents distribution along the width of the cable, for a 40 strand Rutherford cable. The origin of the axes is placed at half the width, thus the width assumes positive and negative values.*

Fig. 56 shows losses distribution along the cable length for a single strand. To avoid misunderstandings in reading the chart, only the function of one arbitrary strand is shown to describe the trend: the functions of all other strands are identical, shifted of a certain value along the longitudinal axis.
Since the model assumes that conductance functions are characterized by peaks, losses should also be concentrated at points where short-range coupling currents flow, i.e. points of contact between the strands. Instead, distribution is almost perfectly sinusoidal and peaks are weakly visible. The reason is due to the number of strand considered as a function of the longitudinal size of the contact between strands and the twist pitch length. In fact, each strand crosses 2*(N-1)* other strands along a twist pitch, this means that there will be the same number of contact points and conductance peaks, equally shifted in the longitudinal direction. These peaks are not dimensionless, but for the geometry of the baseline study case, they have a width equal to $2.7 \cdot 10^{-3}$ m. If all of these peaks are considered individually and placed perfectly side by side, they would cover a length of $2.1 \cdot 10^{-1}$ m, within a twist pitch of only $1.09 \cdot 10^{-1}$ m. This means that these peaks are partially overlapped and in the global function there is no space for minimum values that should separate a peak to the other making them distinguishable. For this reason, the function appears as a continuous sinusoid.
To clarify this concept, see Fig. 57, which shows the values of losses on a pitch twist (expressed as *QTransverse*) extracted directly from THEAPOST software. The chart (a) shows the trend for a single strand of a 40 strands cable with the of the baseline study case, while the chart (b) shows the trend considering a cable with only 10 strands, keeping all other parameters unchanged. In the second case, since the number of contacts is reduced, the conductance peaks are separated and in accord, it is possible to distinguish different peaks of losses.

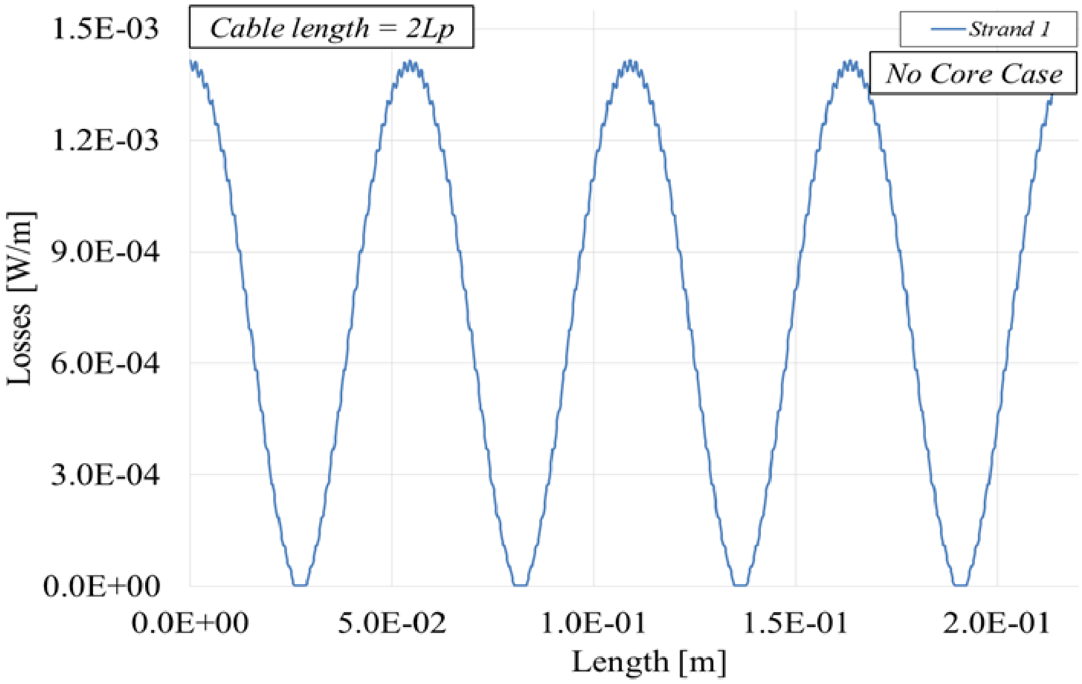

*Fig. 56. Losses distribution along the cable length, for a single strand of a 40 strand Rutherford cable, considering a cable length of two twist pitches.*

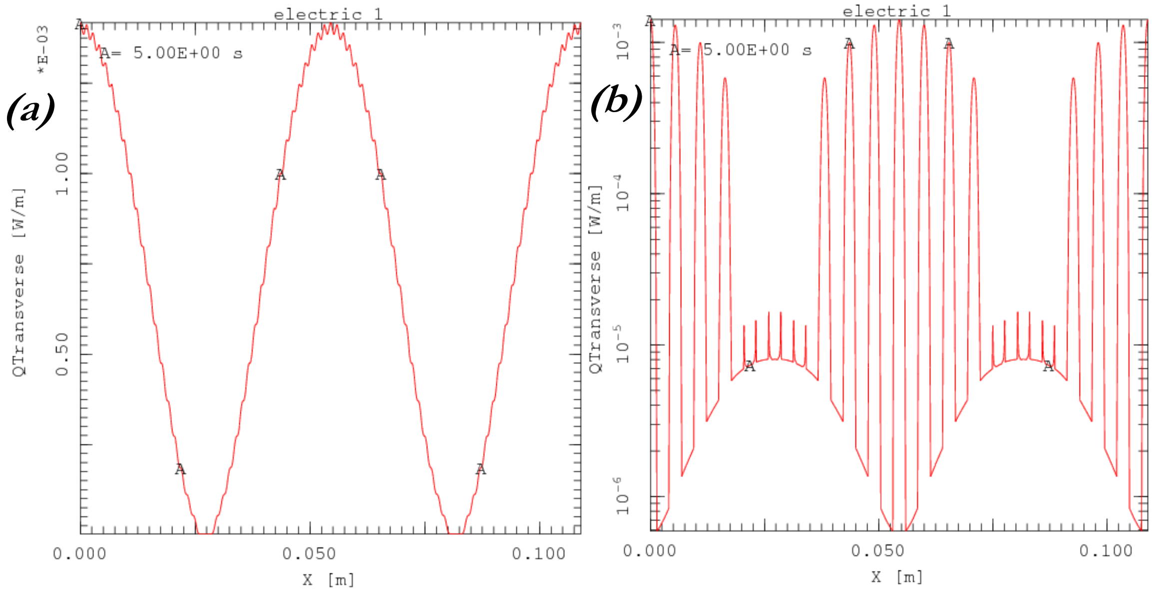

*Fig. 57. Losses distribution along the twist pitch of a cable, for a single strand of a Rutherford cable with (a) 40 strands and (b) 10 strands.*

Fig. 58 shows losses distribution along the cable width. Losses are higher at the cable center, while they assume their minimum value at cable sides. Note that in this case, functions are the same for all strands.

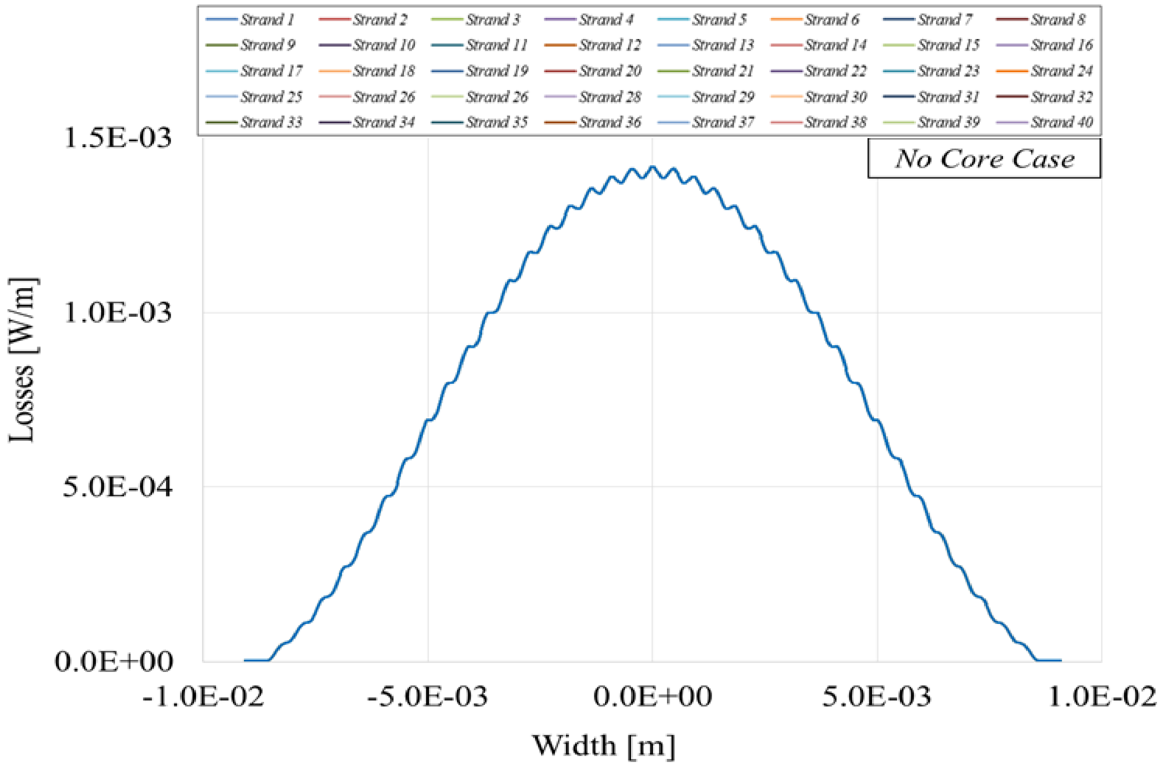

*Fig. 58. Losses distribution along the width of the cable, for a 40 strand Rutherford cable. The origin of the axes is placed at half the width, thus the width assumes positive and negative values.*

## *4.3.1 Studies about the cable sample length and boundary conditions*

As already explained, Rutherford cables used in LHC magnets are usually extremely long; this creates some problems in measuring currents and losses distributions along their entire length, by experiment or through simulations:

- The experimental measurement of losses on the entire length of the cable is impractical and hard to realize. Experiments are performed on short length sections of the cable sample, obtained cutting longer cables.
- Despite the continuum model implemented allows to simulate cables of whichever geometry and length, simulations of long multistrand cables require a high number of mesh elements to maintain the accuracy level to achieve convergence, thus, requiring significantly long computational times even for a powerful calculator.

Therefore, it is necessary to find a proper length and boundary conditions of the cable sample, to insert as input data for simulations, which allow at the same time to simulate an ideally infinite cable, and to represent conditions in agreement with the experiments that are carried out on smaller portions of the cable.

- *Cable length analysis*

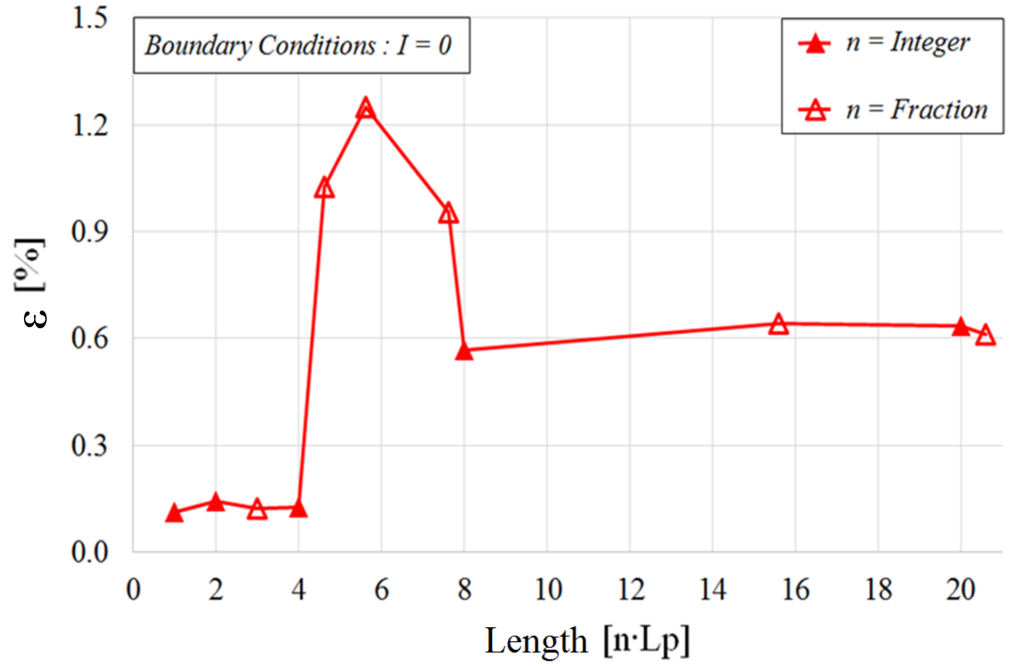

*Fig. 59. Losses variation from the analytical case, simulating different cable lengths. Filled points are for length equal to integer numbers of twist pitch, while blank points consider fractions of the twist pitch. In all cases, boundary conditions of constant current equal to zero are set. Note that the number of mesh elements are varied accordingly to the cable length to achieve convergence.*

From the work reported in [43], when considering a time-varying magnetic field uniform all over the cable, the minimum length of the cable sample that allows to obtain the desired results is equal to a twist pitch. To prove it, Fig. 59 shows that losses per pitch twist (expressed as variations from the analytical result) remain almost the same for all cable length simulated: thus, a cable sample with a length equal to a single twist pitch is sufficient to simulate total losses in longer cables. This assumption is verified, considering boundary condition of null current at both sides of each strand.
Although the periodicity of losses along the twist pitch is demonstrated, real cable lengths are not always equal to integer multiples of the twist pitch. Therefore, it is useful to understand the behaviour of the model for such geometries. Blank points in Fig.59 represent cable lengths involving fractions of the twist pitch. Despite these are the points for which losses deviate more from the analytical results, variations are acceptable and it can be concluded that, for boundary conditions of null current, total losses agree independently by the cable length simulated.

Then, losses distribution along the cable is analysed for different cable lengths. Fig. 60 (a) shows losses distributions for cable length equal to an integer number of twist pitches: total losses functions remains almost constant (with small ripples) for all cases, albeit for simulations of long cables (20 *Lp*), ripples are more pronounced. In all cases, at the cable center the function returns to be nearly uniform. Fig. 60 (b) considers fractions of the twist pitch: in these cases losses distributions assume a marked wavelike trend; ripples are higher for shorter lengths and tends to be smoothed for longer cables. Fig. 61 compares losses distributions for a long cable of length equal to an integer number (20 *Lp*) or a fraction (20.6 *Lp*) of the twist pitch. Functions are very similar in the first part of the cable, while they differ in the second part: considering fractions of the twist pitch, the symmetry of the system is lost. In both cases, ripples are smoothed in their central section.

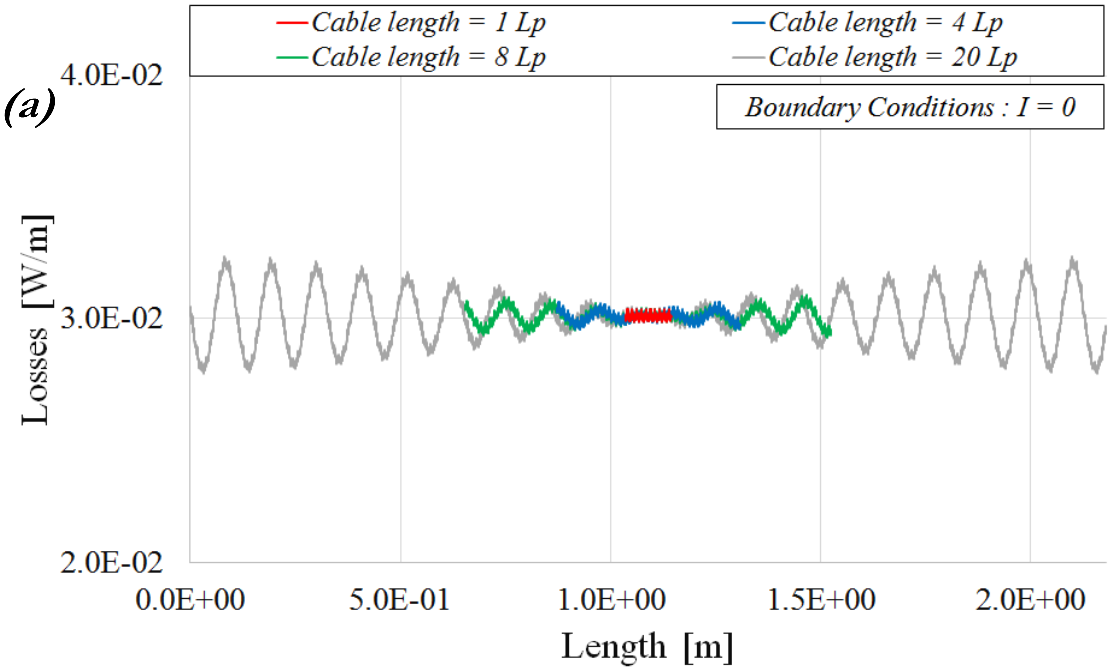

*Fig. 60 (a). Total losses distribution for different cable lengths. All cable lengths are equal to an integer number of twist pitches. Boundary conditions of constant current equal to zero are set for all strands.*

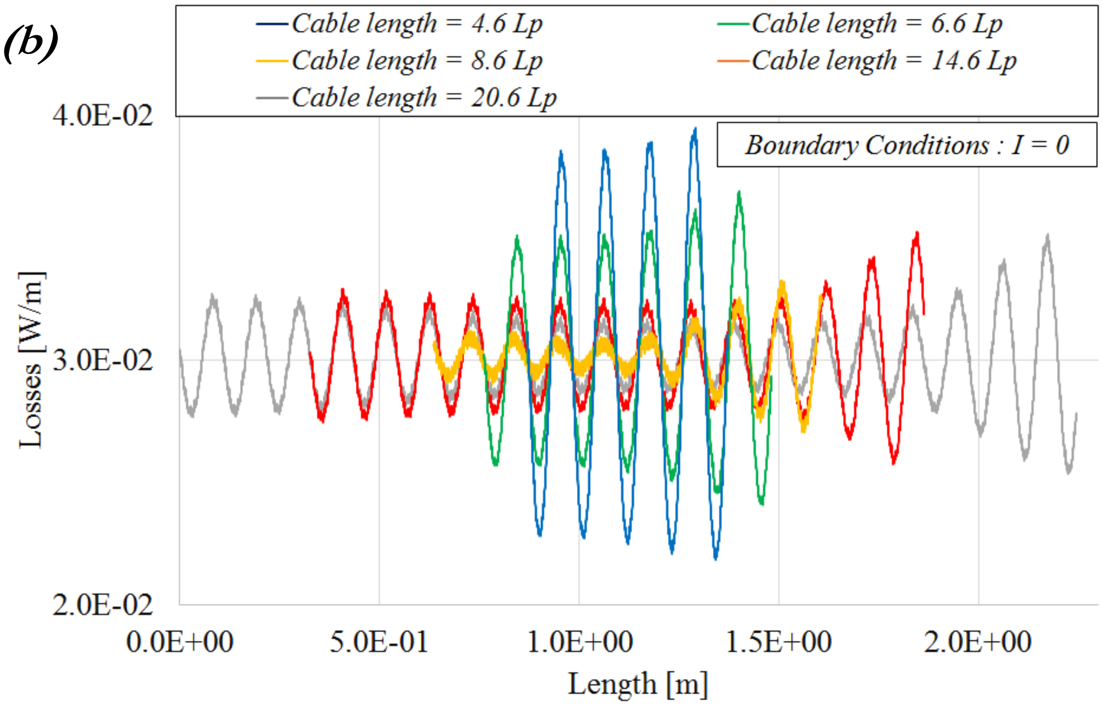

*Fig. 60 (b). Total losses distribution for different cable lengths. All cable lengths involve fraction of the twist pitch. Boundary conditions of constant current equal to zero are set for all strands.*

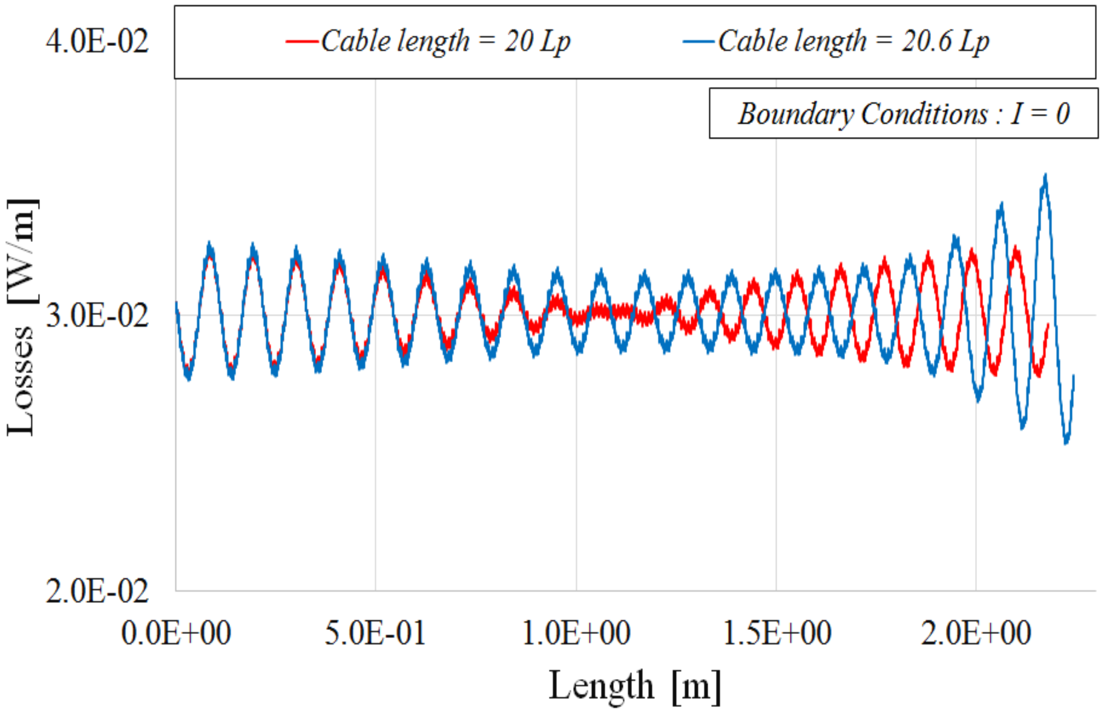

*Fig. 61. Comparison of losses distributions between cables length equal to an integer number of twist pitches (red curve) or a fraction of the twist pitch (blue curve). Boundary conditions of constant current equal to zero are set for all strands.*

## ➢ *Boundary conditions analysis*

As explained, a proper choice of the boundary conditions allows to simulate real measurable conditions. So far in this work, zero current conditions are considered for both sides of the cable sample: this physically corresponds to a model of a neatly cut sample, as it happens in experimental cases. Thus, results are relevant because strictly comparable with measurable reality.

It is demonstrated that under such conditions, a cable sample of a length equal to a twist pitch is sufficient for the calculation of total losses of longer cables. Then a second study is carried out to see if even currents and losses distributions are respected and not only their mean value. Comparisons are made for two cases: a cable of a length equal to one twist pitch (the sample) and a cable with a length equal to nine twist pitches (its results can be extended to infinite cable lengths) focusing on its central section of one twist pitch long. In both cases, boundary conditions of zero current are applied. Fig. 62 explains the concept behind this experiment.

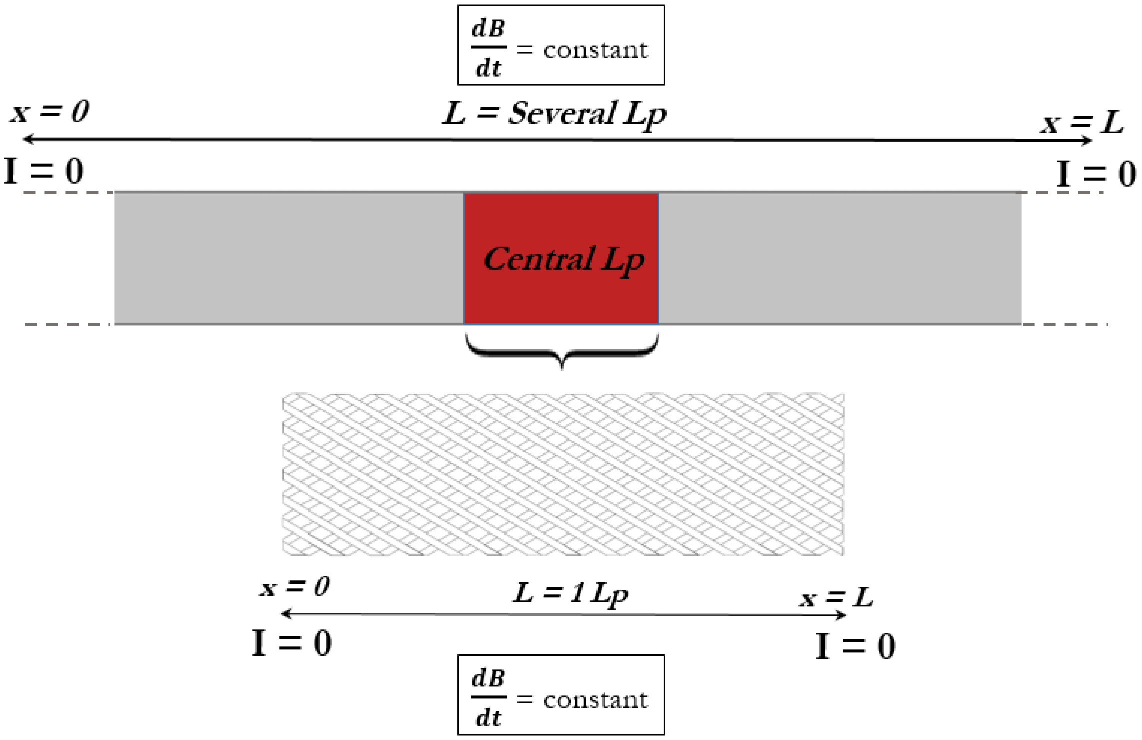

*Fig. 62. The central twist pitch of a cable of infinite length is compared with a cable sample of a length equal to a twist pitch, maintaining the same boundary conditions and considering the same uniform time-varying magnetic field.*

Comparisons between currents and losses distributions for the two cases are shown in Fig. 63 - 64. In Fig. 64 for simplicity, only one strand is presented, but results can be extended to all strands.

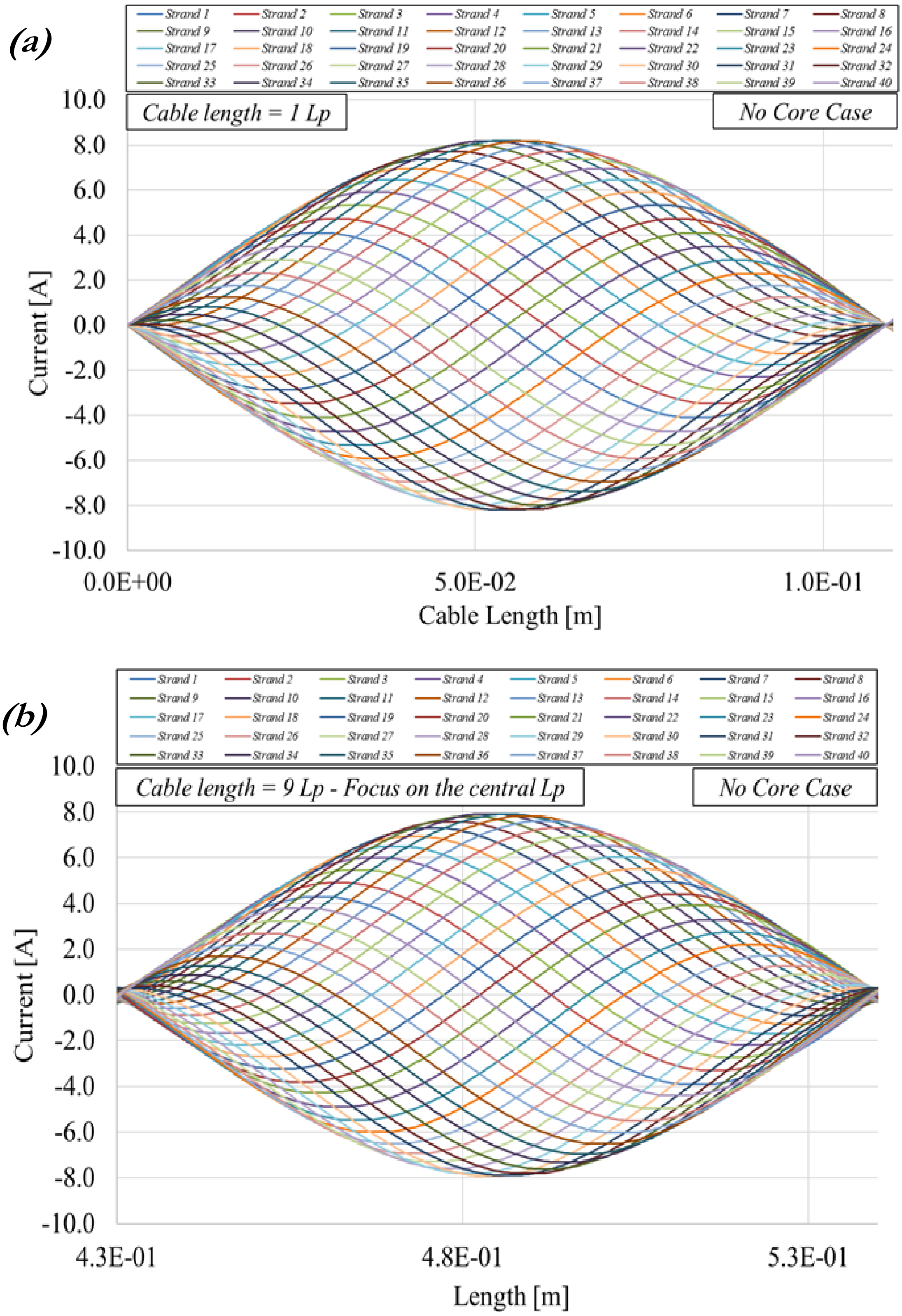

*Fig. 63. Current distribution in a 40 strands Rutherford cable sample of one twist pitch long (a) , and in the central twist pitch of a 40 strands Rutherford cable of nine twist pitch long (b).*

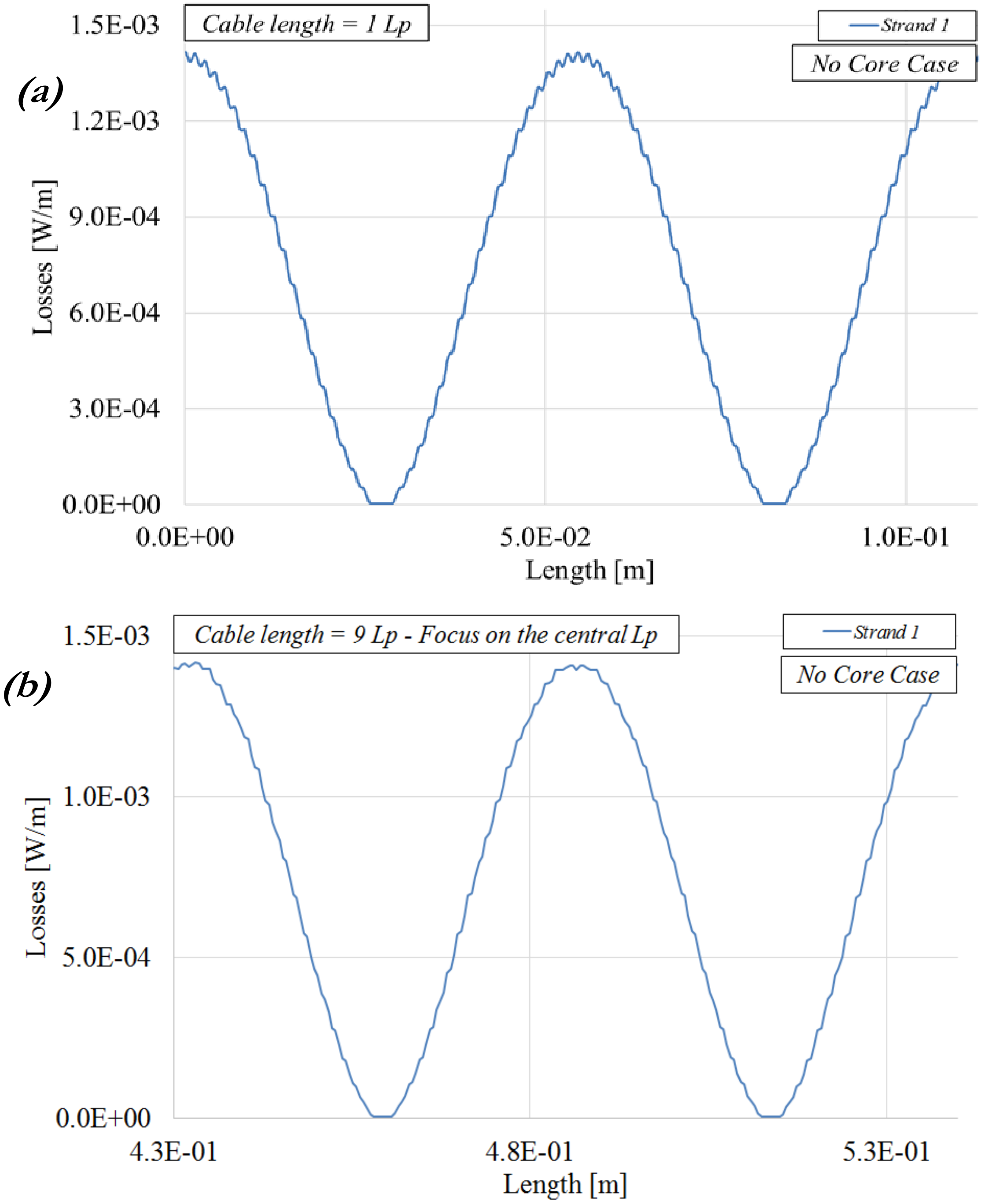

*Fig. 64. Losses distribution in a 40 strands Rutherford cable sample of one twist pitch long (a) , and in the central twist pitch of a 40 strands Rutherford cable of nine twist pitch long (b).*

Curves are very similar for both figures, this allows to derive two conclusions:

- A cable sample of a minimum length equal to one twist pitch is sufficient to simulate losses distributions, and not only the total losses value, along longer cables. This also confirms the periodicity of currents and losses distributions in a Rutherford cable subjected to a uniform magnetic field, with period equal to the twist pitch, as reported in [6]. By the way, some cases remains excluded; in fact, the periodicity is lost when short cables with lengths involving fractions of twist pitch are simulated. Increasing the length of the cable, however, this dependence by the length is substantially lost, as shown in Fig. 61.

- Results obtained do not depend on the position where boundary conditions are placed, as already concluded in [43]. In fact, simulated distributions are identical both in cases in which boundary conditions are at the ends of the cable sample analysed, or they are far from the central section taken into account inside a longer cable.

Then, by setting different boundary conditions, it is possible to simulate other situations, such as when strands are not simply cut at the ends of the cable sample but they are welded together: in this case equipotential boundary conditions are used (zero voltage for each strand, in particular).

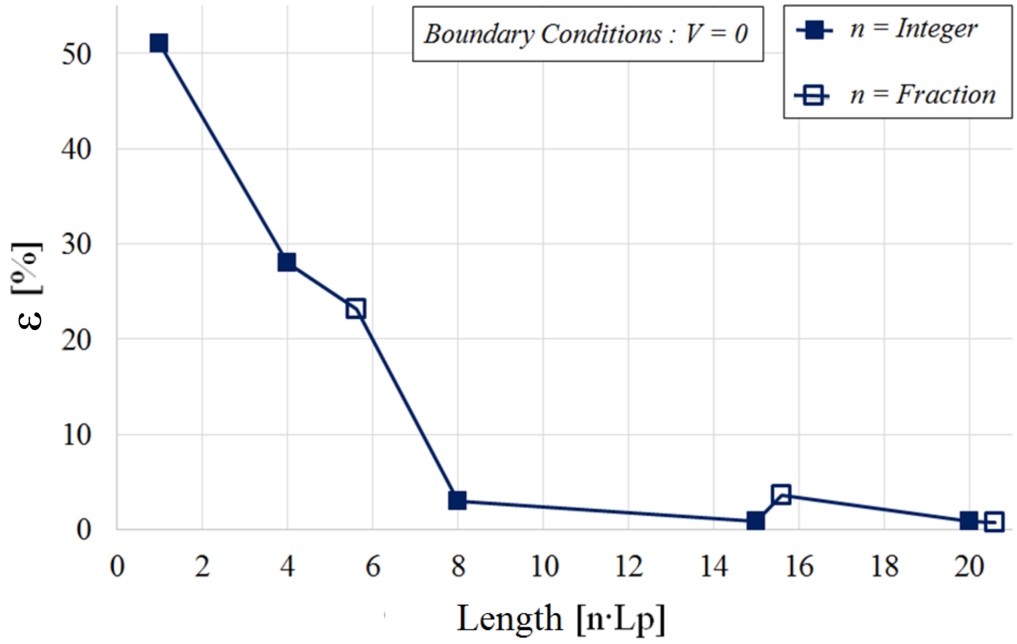

*Fig. 65. Losses variation from the analytical case, simulating different cable lengths. Filled points are for length equal to integer numbers of twist pitch, while blank points consider fractions of the twist pitch. In all cases, boundary conditions of constant voltage equal to zero are set. Note that the number of mesh elements are varied accordingly to the cable length to achieve convergence.*

Concerning total losses, simulations are performed on different cable lengths, involving integer or fractions of the twist pitch, as shown in Fig. 65. The calculation of total losses per twist pitch is performed considering only the central twist pitch of every cables, since for equipotential conditions the losses distribution varies consistently from the cable sides to its center. Differently from the current boundary conditions (Fig. 59), in this case losses presents significant variation from the analytical case when they simulated short cable lengths. In particular, a cable sample length equal to a single twist pitch is not sufficient to simulate total losses on longer cables. However, increasing the cable length, results returns in agreement both with the analytical case and with simulations using current boundary conditions. To understand this behaviour, total losses distributions are compared for short (1 Lp) and long (20 Lp) cable lengths in Fig. 66, considering boundary conditions of constant null current (blue curve) and constant null voltage (red curve).

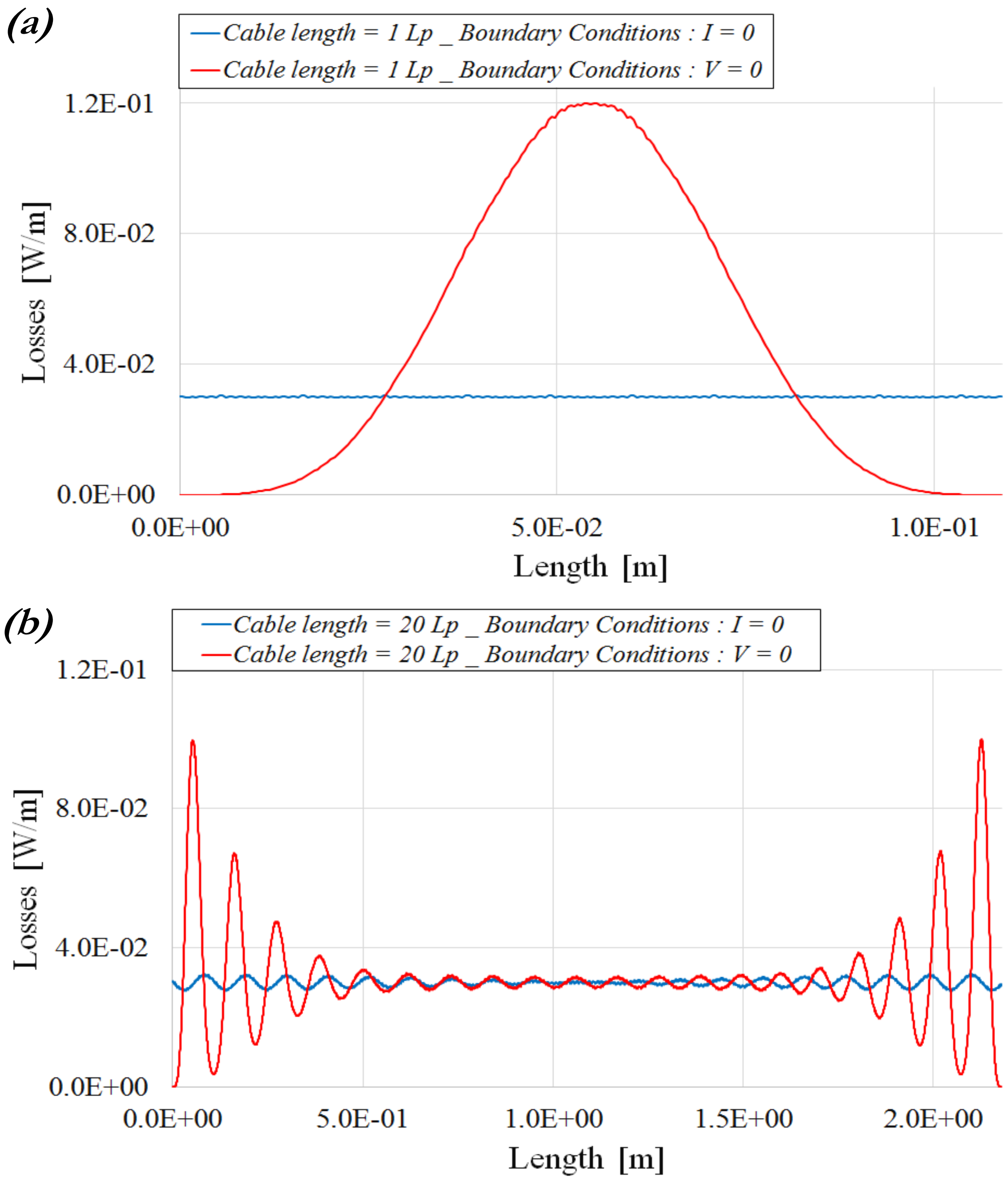

*Fig. 66. Total losses distribution in a cable sample of length equal to (a) one twist pitch or (b) 20 twist pitches, considering different boundary conditions at both sides: current equal to zero or voltage equal to zero.*

For the shortest cable (Fig. 66 (a)), losses distribution is strictly dependant by the boundary conditions chosen. It remains almost constant (with minor ripples) considering zero current conditions, while it assumes a Gaussian shape when considering equipotential conditions; the maximum value of this function in particular, is four times higher than the maximum value assumed by the blue curve. This partly explains the great difference between total losses for such short cables. Conversely, simulating longer cables (Fig. 66 (b)) the difference between the two losses distributions decreases, down to a negligible amount when only the central section is considered.

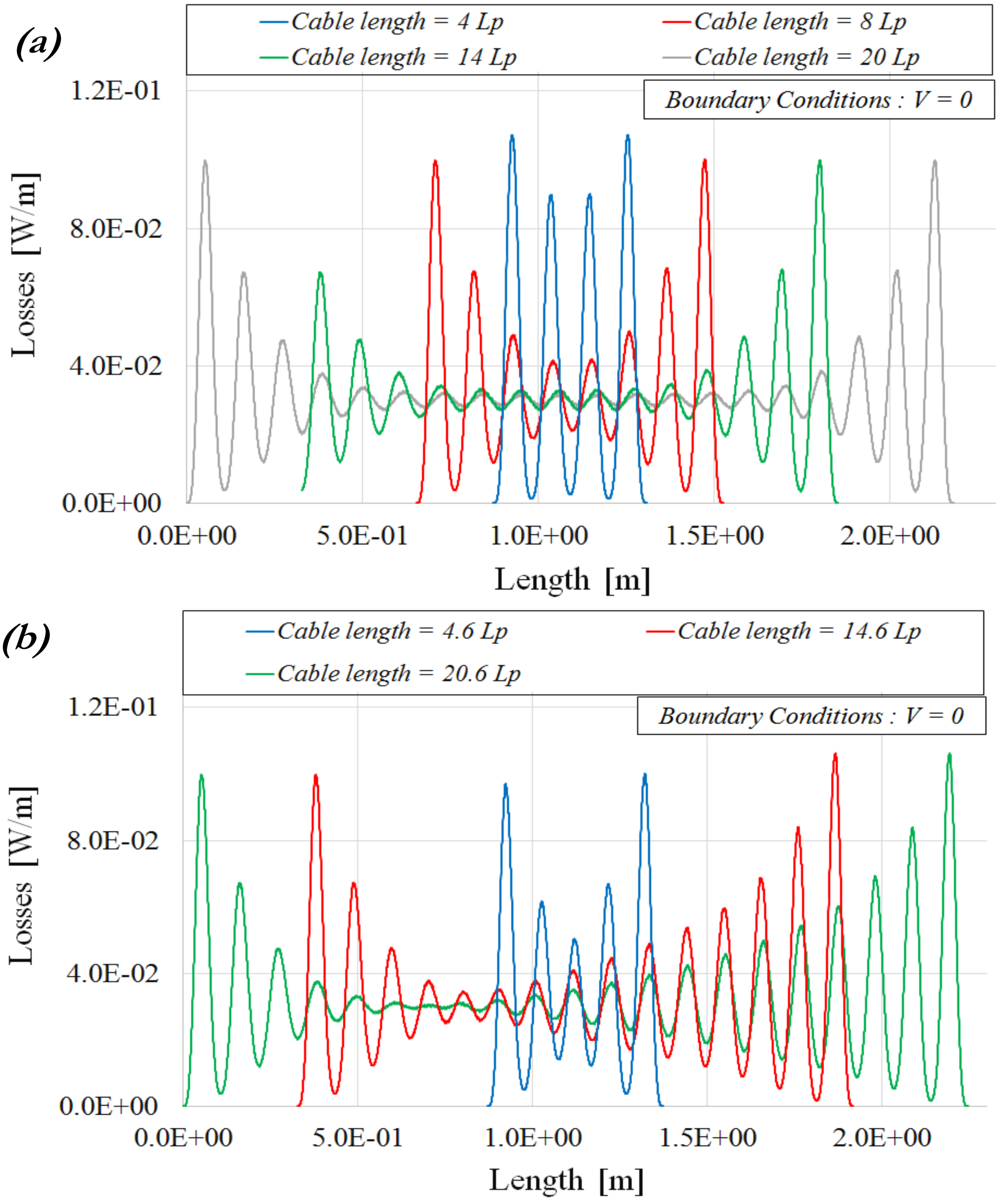

*Fig. 67. Total losses distribution for different cable lengths: (a) considering integer numbers of the twist pitch or (b) fraction of it. Boundary conditions of constant voltage equal to zero are set for all strands.*

As realized for uniform current conditions, losses distributions are investigated for realistic cables lengths, setting equipotential boundary conditions. Simulations are performed for cable lengths equal to an integer number (Fig 67 (a)) or fractions (Fig. 67 (b)) of the twist pitch. Functions present the following features: a wavelike trend with a peak for each twist pitch; ripples are higher at the boundaries and smoothed at the cable center. Although at first glance, no clear differences appear between functions considering integers or fractions of the twist pitch (compared to the case with constant current conditions), an accurate analysis allows to highlight some of them. Fig. 68 compares losses distribution for long cables; functions are very similar in the first part of the cable, while they differ in the second part: considering fractions of the twist pitch, the symmetry of the system is lost

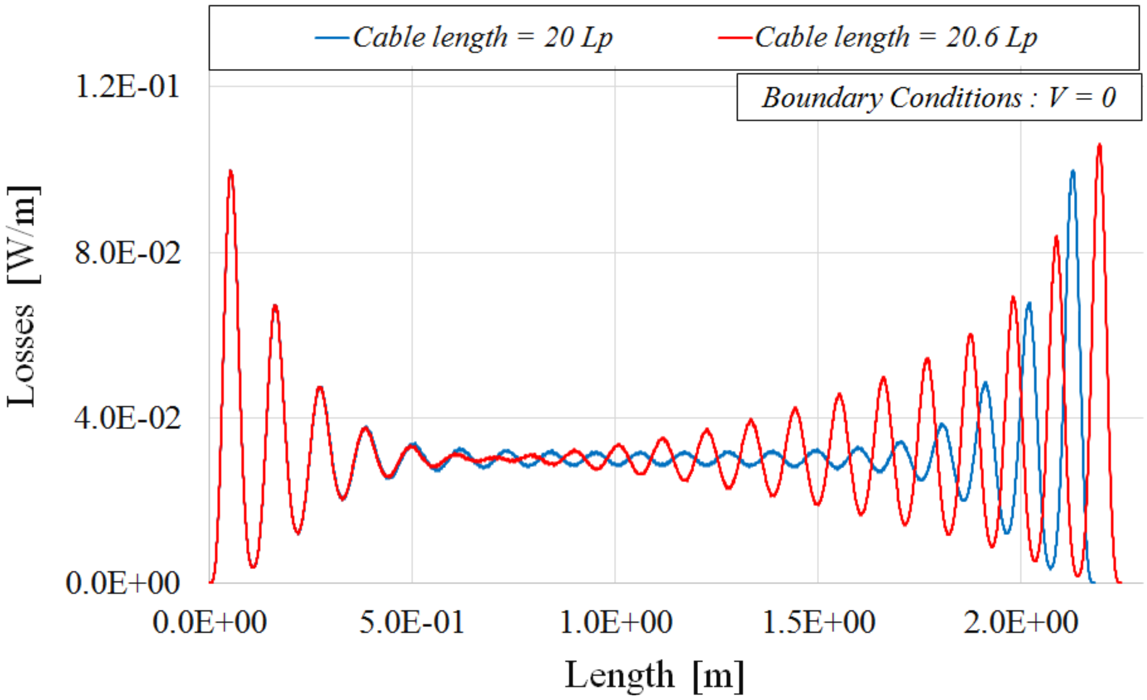

*Fig. 68. Comparison of losses distributions between cables length equal to an integer number of twist pitches (red curve) or a fraction of the twist pitch (blue curve). Boundary conditions of constant voltage equal to zero are set for all strands.*

Finally, this study leads to the following conclusions:

- Simulating sufficiently long cables and considering cable sections (equal to a twist pitch) sufficiently distant from the boundaries, the losses distribution is independent of the choice of boundary conditions and by the position in which they are set.
- When equipotential boundary conditions are set, simulations of short cables leads to substantial differences from the analytic results. Increasing the cable length, differences are reduced. Therefore with these boundary conditions, it is not possible to use a cable of one twist pitch to simulate total losses of longer cables.
- Considering realistic cable lengths where fraction of the twist pitch are involved, the symmetry of the system is lost for all boundary conditions. However, increasing the

length of the cables, this dependence is reduced and the value of total losses and the losses distribution over the central twist pitch returns to convergence.

Despite the importance of these conclusions, their applicability has limitations: they are not valid when the time-varying magnetic field varies along the length of the cable. In addition, the choice regarding the boundary conditions used to simulate what really happens at cable terminals remains unclear. Real cables are not cut as in experimental cases (uniform current conditions) or welded (equipotential conditions), but usually there are joints that connects them to the following cables; this situation is intermediate between the two conditions and it is not easy to implement in the code. For these reasons, furthers studies are needed.

## Chapter 5

# Losses and current distribution in superconducting Rutherford cables with core

In this chapter, one of the main strategies implemented to reduce AC losses inside Rutherford cables is described. It concerns the introduction of a new element within the superconducting cable, called core [44 – 48]. Subsequently, this technique is implemented in simulations, deducing conclusions about its effectiveness.

## 5.1 What is core

Core is a resistive strip of various width, thickness and material, inserted inside the Rutherford cable, which separates the top layer of strands from the lower [14]. In Fig. 69, sections of two Rutherford cables are shown.

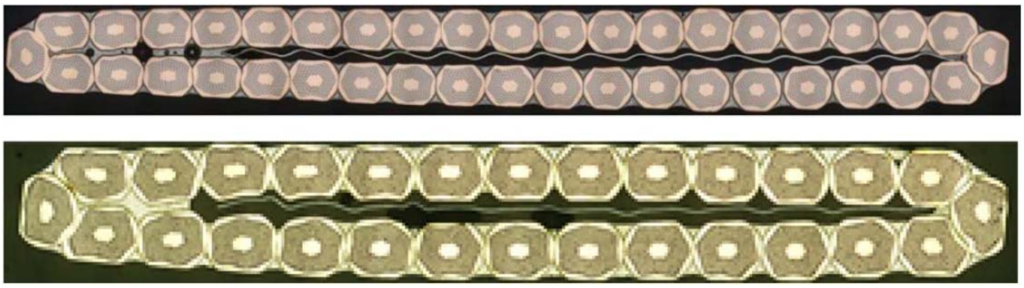

*Fig. 69. SEM images of a cross-section of two Rutherford cables with core [49].*

The interposition of a resistive material in the region between different strands changes the value of resistances that characterize contacts. As seen in Chapter 4.2.3, increasing the resistance between strands (especially *Rc*), the intensity of interstrand coupling currents is reduced and total losses are lowered. However, *Rc* and *Ra* should remain inside proper limits: they have to provide sufficiently high *ICRs* to suppress ISSCs, but still enough low to guarantee a proper current sharing between strands. Therefore, with an accurate choice of core's parameters, it is possible to reduce AC losses compared to uncored cables, without affecting stability. See Fig. 70 for a comparison of sections of cored and uncored cables.

Most of the cores are composed of *stainless steel* (to improve the mechanical stability and to ensure the increase of interstrand resistance) and *copper* (to provide a normal metal shunt path for magnet protection). However, the evolution of superconducting materials evolves together with those of the materials constituting the core, therefore in the years, several other options have been experimented in terms of core geometries and materials, such as Mg-o paper tape [34], woven s-glass [50] and Cr-plated stainless steel [15].

In addition, the introduction of the core brings other advantages, which are briefly introduced:

- It reduces field distortions. Even when ISCCs are weak, their presence causes "*dynamic magnetization*" (see Chapter 3), which produces distortions in the magnetic field in magnet bores. Suppressing ISCCs, this problem is lowered.

- It enhances the longitudinal *quench propagation velocity* $v_q$. $v_q$ is one of the parameters defining the requirements of the protection of a cable [51 - 52]. Inserting a core it is possible to enhance $v_q$ consistently, allowing faster quench detection and protection systems.

- It improves mechanical properties. Stainless steel core enhances mechanical resistance and elongation, providing additional tensile strength. Thus, cored cable can withstand higher winding tensions than an uncored cable [53 - 54]

- It reduces by a factor from 2 to 5 the thermal conductivity between non-adjacent strands, compared to non-cored cables. Optimal stability conditions for a cable are obtained at low conductance: a reduction in the interstrand thermal conductance reduces the transverse normal zone propagation, therefore improving the chances for strands for recovery [12].

- It reduces the cost of the cable, by segregating some amount of copper in the core. In fact, this procedure does not affect the manufacturing cost (segregated copper's cost is negligible compared to the copper co-processed with the superconductor); thus, by increasing the amount of copper within the core, leaving unchanged the total amount used for the cable, it is possible to reduce the capital cost [52 - 53].

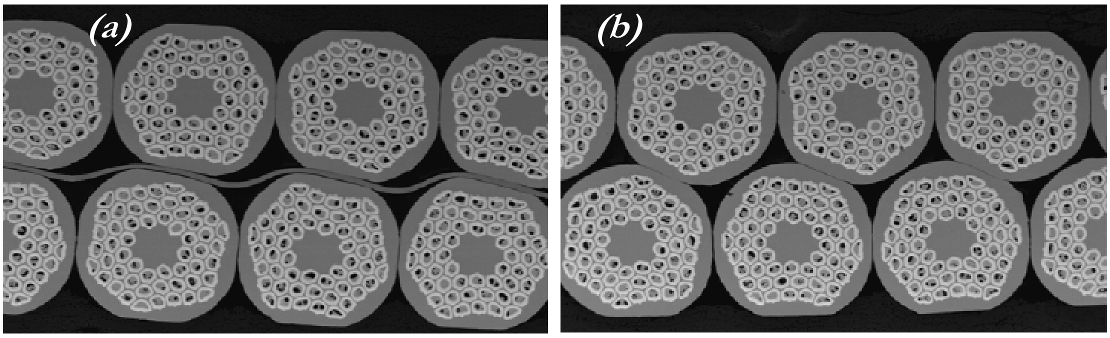

*Fig. 70. Cross-section of Rutherford cables (a) with and (b) without an inner core [55].*

## 5.2 Model implementation in THEA

Some modifications are performed into the THEA code, in order to include the core in the system. No changes are made in the *.input* file, then no electric element are added: none longitudinal current is considered to flow into the core. In practice, the presence of the core only affects the value of the electrical resistance *Rc* set in the proper *External Routine.* At the same time the value of *Ra* remains unvaried, since the core does not physically interpose between adjacent strands. In Fig. 71 it is reported a comparison in terms of *ICRs* between cored and uncored cables.

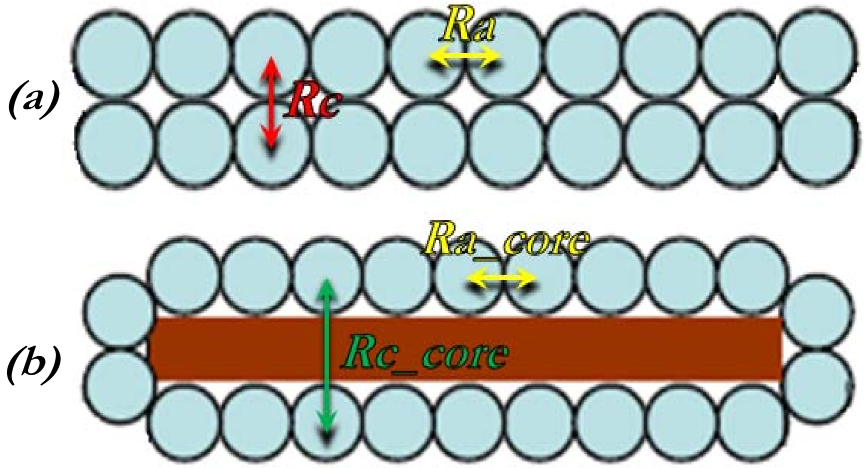

$$Ra = Ra\_Core \quad \text{and} \quad Rc < Rc\_core$$

*Fig. 71. Cross-section of Rutherford cables (a) without and (b) without an inner core, with the highlight of resistance variations.*

It is not easy to deduce a priori the *Rc_core* value (the resistance between non-adjacent strands due to the presence of the core) that a certain type of core introduces in the system. *Rc_core* value is a function of:

- The intrinsic characteristics of the core: the thickness, the materials used and their arrangement within the core and the thermo-mechanical processes carried out to realize the core.
- The characteristics of the Rutherford cable: not all cores are effective for all cables.
- The processes that occur during the coupling between the core and the cable.

This function has no analytical formulae, thus often must rely on experimental analysis.

However, even when the electrical parameters of the core are set, it is not sufficient to define the electric resistance values that characterize every contact between non-adjacent strands. In fact, they depends on core geometry; for the 2D model used the width of the core and its placement are specifically relevant. When the core width is not equal to the cable width, means that the core can be interposed between some contacts (in the following, the term "covering" contacts is used) and not be interposed between some others; this depends on the relative position of each contact and the core.

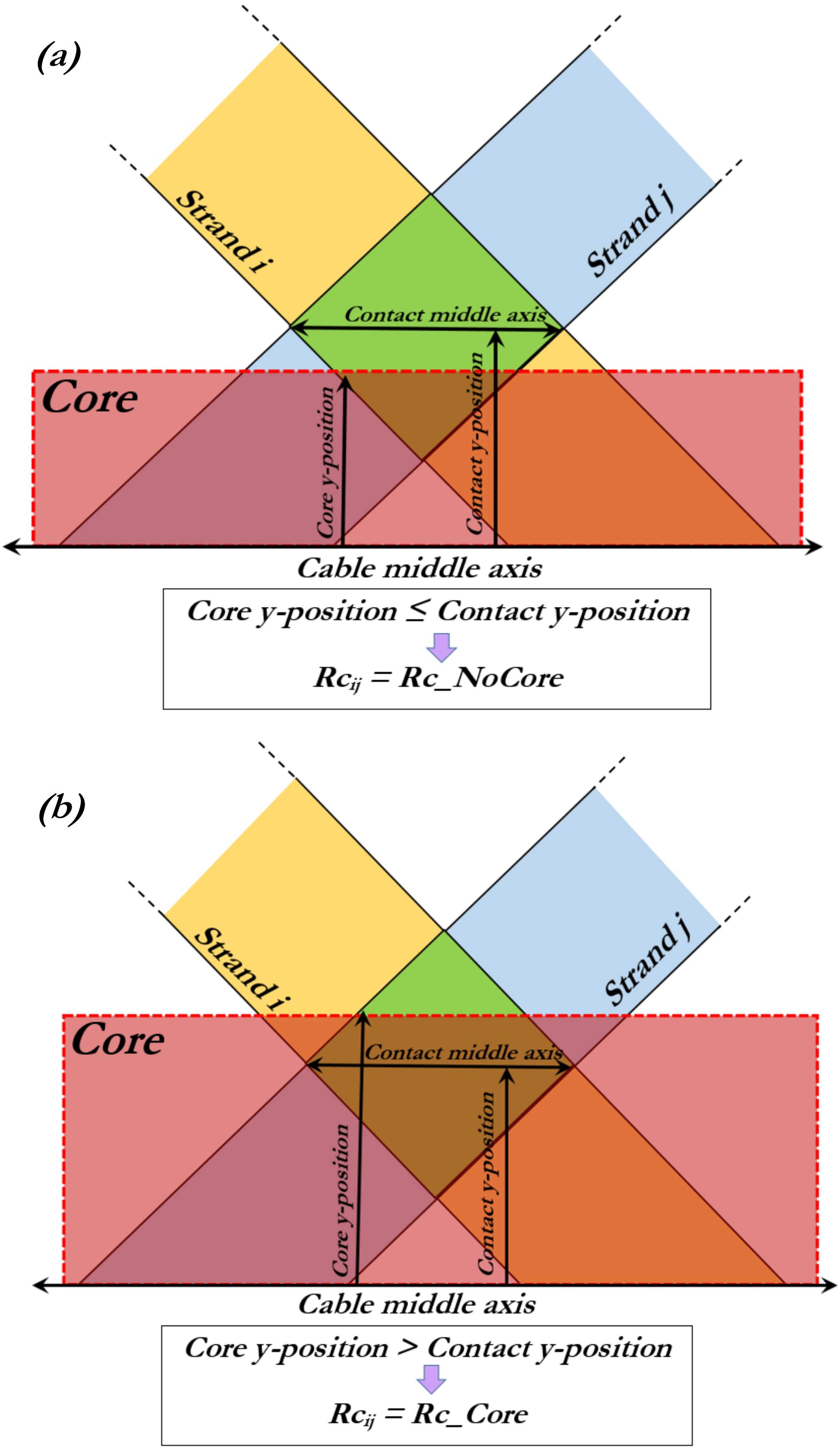

*Fig. 72. Contacts between two generic strands (a) covered or (b) not covered by the core, and resistance values considered for each case.*

Furthermore, given that contacts between strands are not dimensionless but they have a width (although very small than the width of the cable) and that it is not feasible to define *Rc_core* in cases of a partial coverage of a contact, the following assumption is made. If the core covers more than half the size of the contact (i.e., if the $y$ position of the core exceeds the $y$ position of the center of a contact), then the contact is considered entirely covered by the core and the *Rc_core* value is assumed for that contact. Otherwise, if the size of the core covers half of the contact or less, the contact is considered to not be covered by the core and the resistance is assumed equal to the uncored cable case. In Fig. 72 this concept is explained over a generic contact.

## *5.2.1 Parametric studies*

This chapter reports the study about the dependence of cable total losses by the electrical and geometrical characteristics of the core. The cable features simulated are identical to those presented in Chapter 4.2.1, in this way results can be compared with those obtained with the uncored cable described in Chapter 4.

No reference core is used, but conclusion are general and applicable to any kind of core. Furthermore, as well as the model described in Chapter 4, even the model implemented with the core can be applied independently of the geometry and electrical characteristics of the strands and the core and the magnetic field conditions of the system.

- *Impact of the core width:*

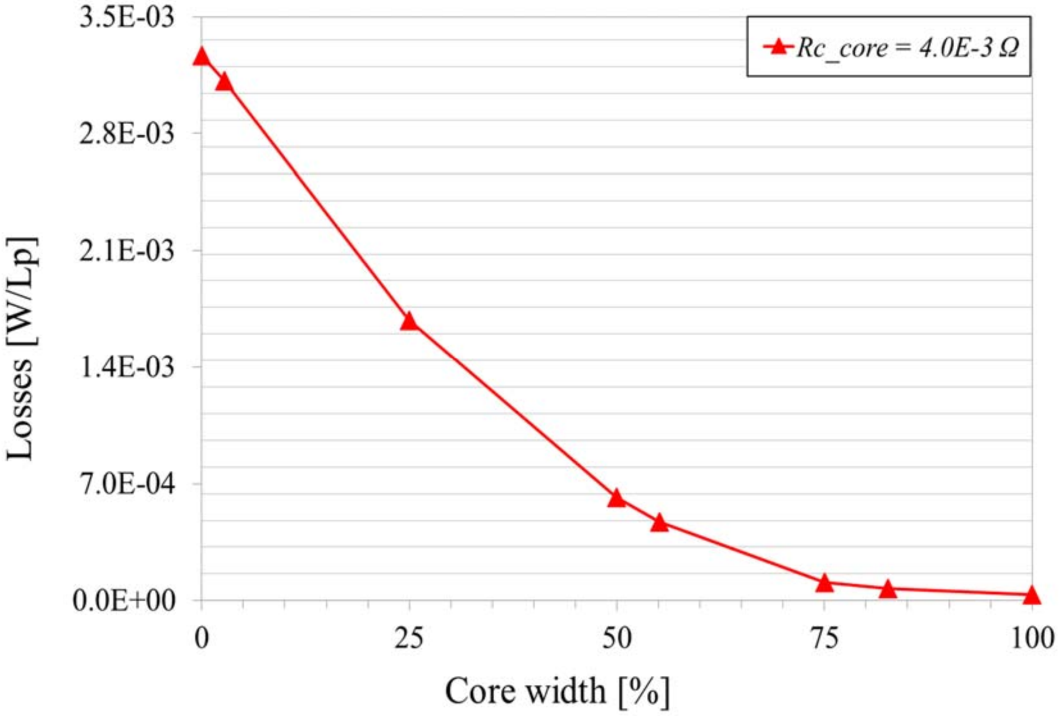

*Fig. 73. Simulation results for losses varying the core width. The resistance Rc_core is set equal to 4.0*·$10^{-3}$ Ω *for every cases.*

Core width is variated, as a percentage of the total width of the cable:

$$Core\ width\ =\ \frac{Cable_{width}}{Core_{width}}\cdot 100$$

A percentage equals to zero, is equivalent to the uncored cable case. Core is kept central.

The *Rc_core* value is set equal to $4.0\cdot10^{-3}\ \Omega$ (100 times bigger than in the uncored case). Results are displayed in Fig. 73 were semi-logarithmic scale is used. As expected, as the size of the core increases, the losses are reduced.

One may wonder, if even very limited changes in the core width can lead to significant variations in losses; therefore, it is useful to state the following consideration. Since it is considered that the core covers a contact as soon as the transverse position of one of its two sides is greater than the transverse position of the contact middle axis, it is necessary to understand that for an arbitrary increase in the size of the core, there is no general rule about how many contacts between strands are covered by the core that were previously uncovered. A small increase of the width of the core "$\Delta$*width*" may not be sufficient to cover new contacts, while an increase *"*$\Delta$*width* + $\delta$", with $\delta$ that can be very little, could be enough to obtain a different result. When the baseline study case geometry is used, for example, there is no difference between losses in a cable with a central core which covers 25% or 27.5% of the cable width, because passing from one case to the other, no extra contact is covered by the core.

- *Impact of Rc_core:*

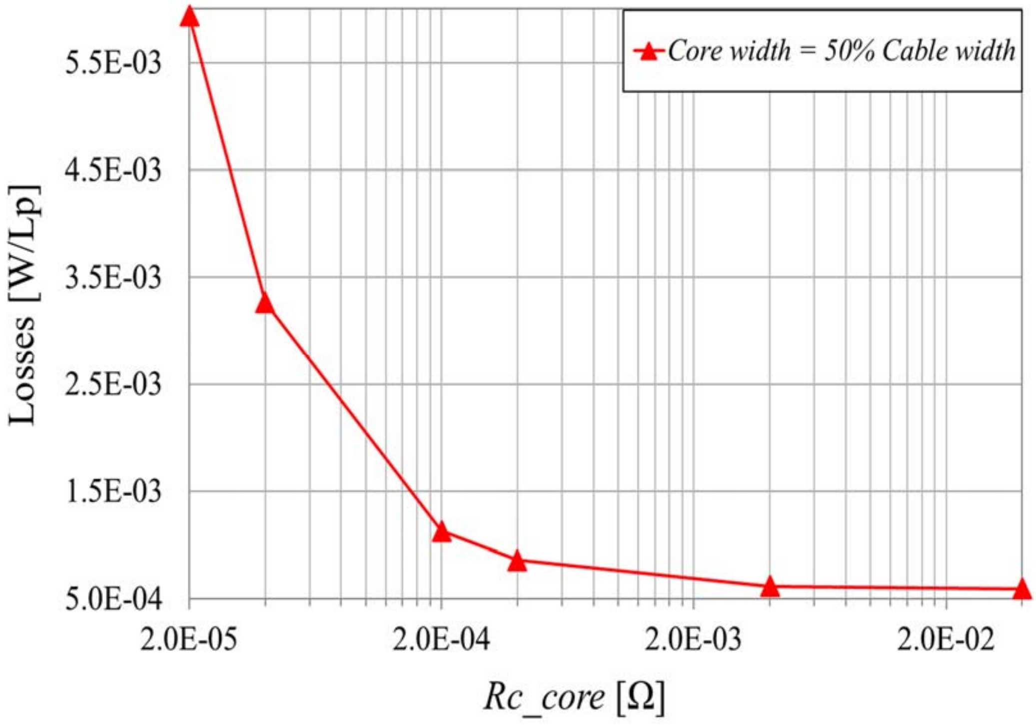

*Fig. 74. Simulation results for losses varying the Rc_core value. The width of the core is set equal to 50% of the cable width for every cases.*

Rc_core value are varied, keeping the core width equal to 50% of cable width has for every cases. Core is kept central.
Results are displayed in Fig. 74 were semi-logarithmic scale is used. As expected, as the resistance Rc_core increases, losses are reduced.

### ➢ *Impact of the core positioning:*

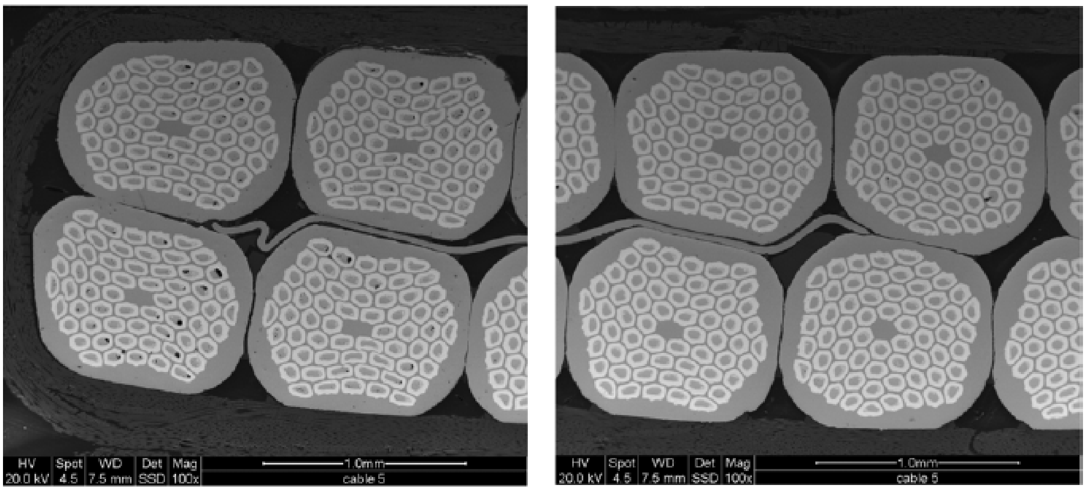

*Fig. 75. Cross-section of a Rutherford cable, focusing on core ends. Due to inhomogeneities, the core is off-center. [56].*

To complete the study, it is analysed what happens when the core is not placed centrally compared to the cable width, but it is shifted to one side. In fact, the positioning of the core can deviate from the central position, due to irregularities during insertion (see Fig. 75 for a practical example). It is important to know if this situation represents a limit or an advantage in terms of performance of the cable.
Therefore, the possibility to set the exact position of the core ends is implemented in THEA.

In the following charts, core positioning is set through a variable called α; its value is calculated through the following formula:

$$\alpha = \left( \frac{Y_{CoreShifted} - Y_{CoreCentered}}{\text{abs}\,(Y_{Cable} - Y_{CoreCentered})} \right) \cdot 100 \ [\%]$$

Where:

- $Y_{CoreShfted}$ = $y$ position of the side of the shifted core which is nearer to one of two cable sides, calculated from the middle axis of the cable (note: if the core is placed centrally, it makes no difference which of the two sides of the core is considered).

- $Y_{CoreCentered} = y$ position of the upper side of the centered core, calculated from the middle axis of the cable. The sign of this value changes accordingly to this relation: it is taken positive if $Y_{CoreShfted}$ is positive or negative if $Y_{CoreShfted}$ is negative.

- $Y_{Cable} = y$ position of the upper side of the cable, calculated from the middle axis of the cable. The sign of this value changes accordingly to this relation: it is taken positive if $Y_{CoreShfted}$ is positive or negative if $Y_{CoreShfted}$ is negative.

When α is positive, it means that the core is shifted "upward" compared to the perfectly centered position; this situation is shown in Fig. 76, for the *x-y* and *y-x* planes of the cable. When α is negative, it means that the core is shifted "downward" compared to the perfectly centered position; this situation is shown in Fig. 77, for the *x-y* and *y-x* planes of the cable. When α equal is equal to 0% , it means that the core is not shifted from the central position while, at the opposite, values of +100% or -100% represents the case in which the core is shifted to its maximum, reaching the cable sides.

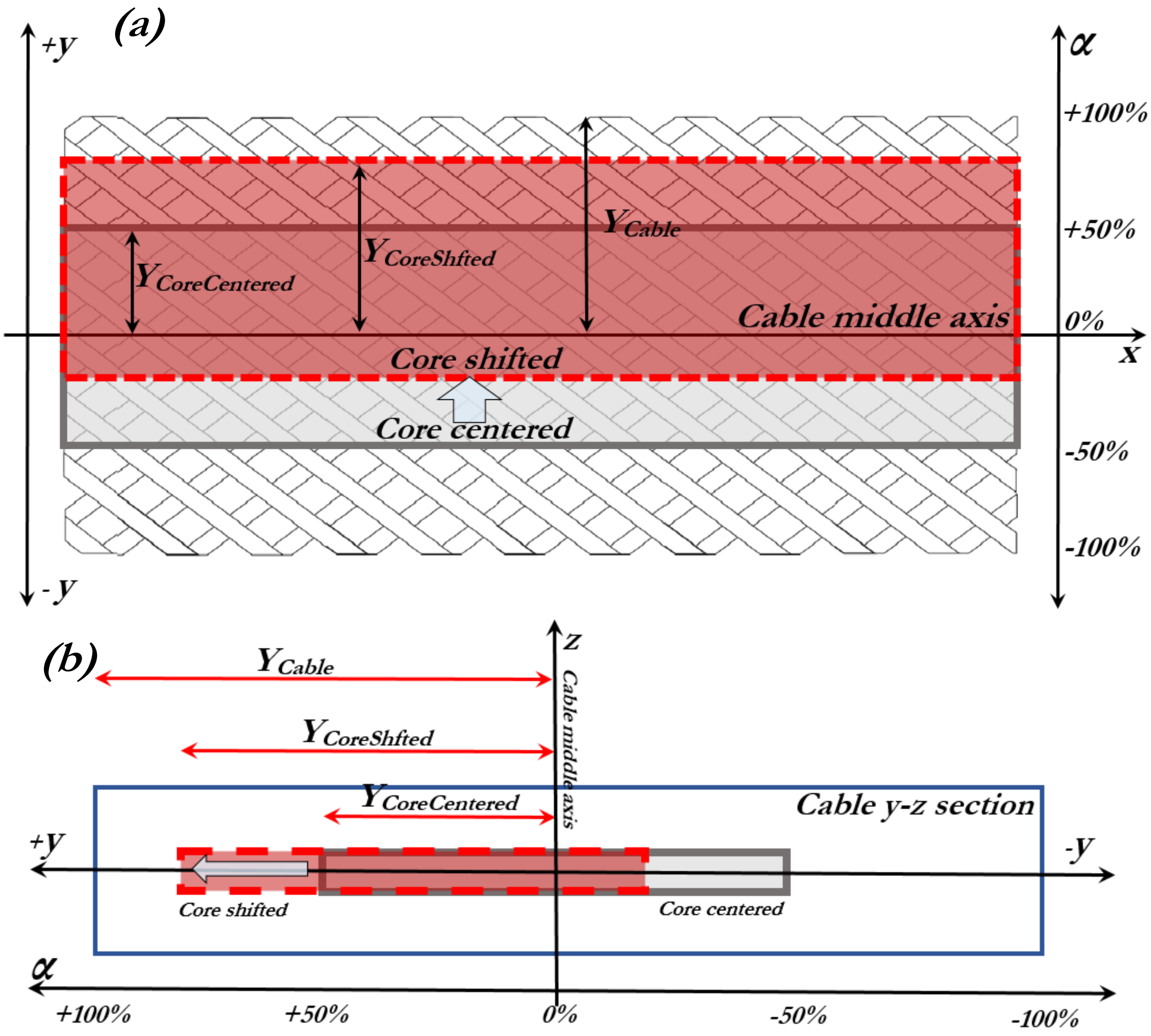

*Fig. 76. (a) x-y and y-z planes of a Rutherford cable with core shifted upward from the central position.*

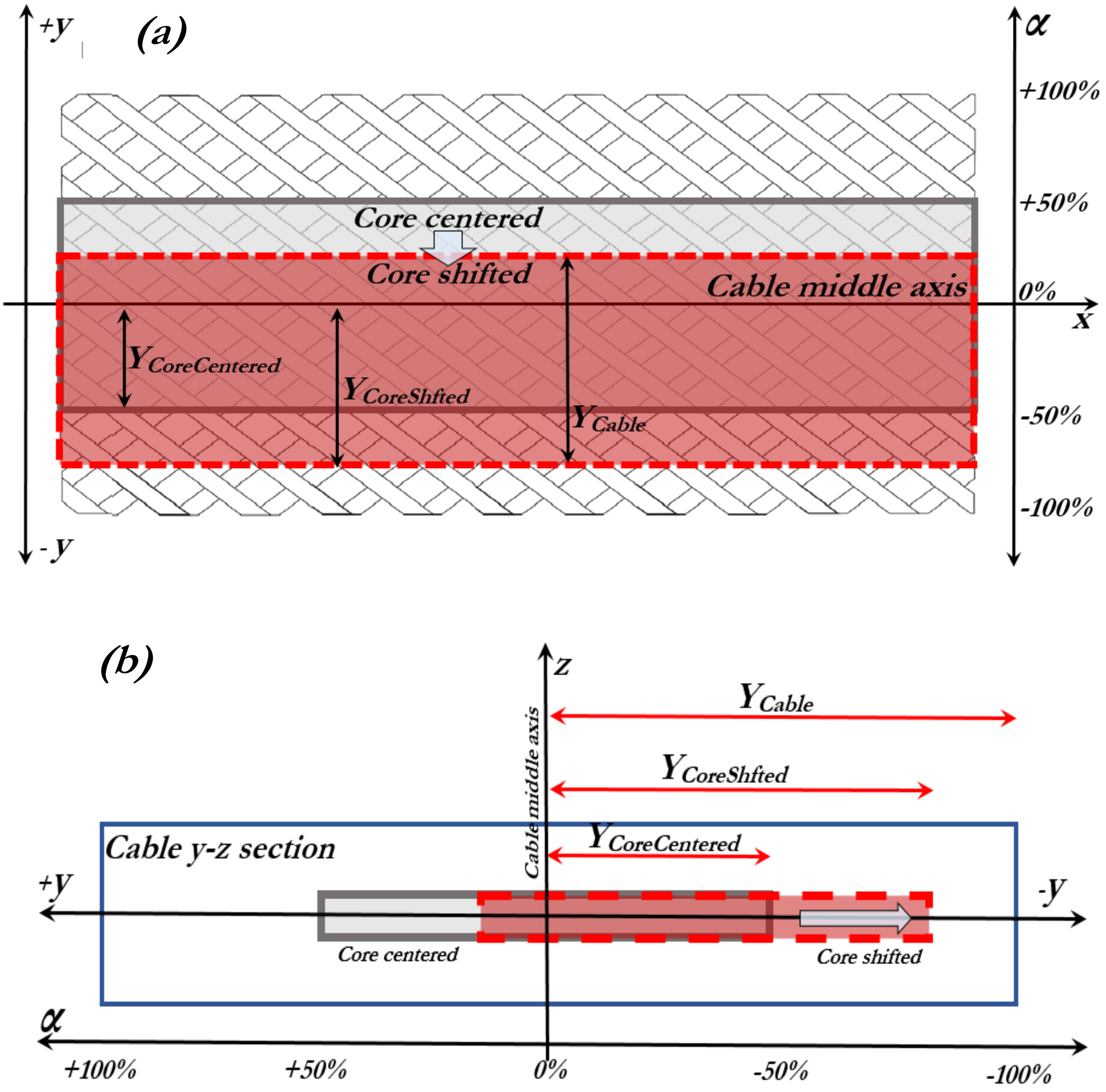

*Fig. 77. (a) x-y and y-z planes of a Rutherford cable with core shifted downward from the central position.*

Simulation results are compared with the uncored case.
For the first study *Rc_core* is set equal to $4.0\cdot10^{-3}\ \Omega$ (100 times bigger than in the uncored case) and core positioning is varied considering cores of different width. The variation from the uncored case (which in each case is represented in the charts by points with α equal to zero) is displayed by means of the parameter *ε_Core*, a percentage calculated with the following equation:

$$\varepsilon\_Core = abs\left(\frac{Losses_{CenteredCore} - Losses_{ShiftedCore}}{Losses_{CenteredCore}}\right)\cdot 100$$

See Fig. 78 for results.

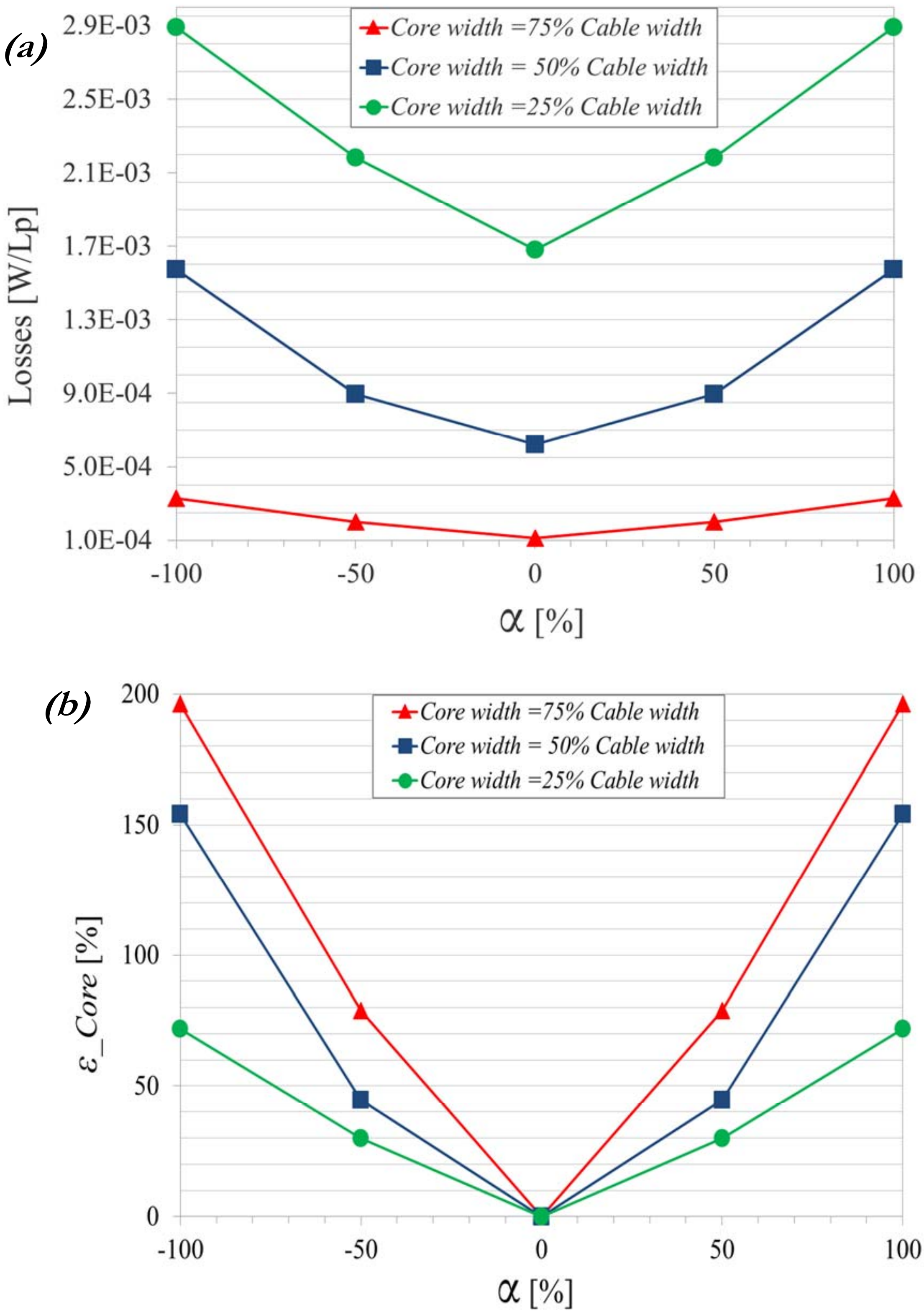

*Fig. 78. (a) Simulation results for losses, varying the positioning of the core inside the cable, setting the value of Rc_core equal to $4.0{\cdot}10^{-3}$ Ω; (b) variation between the shifted case and the centered case. In both charts different core width are displayed.*

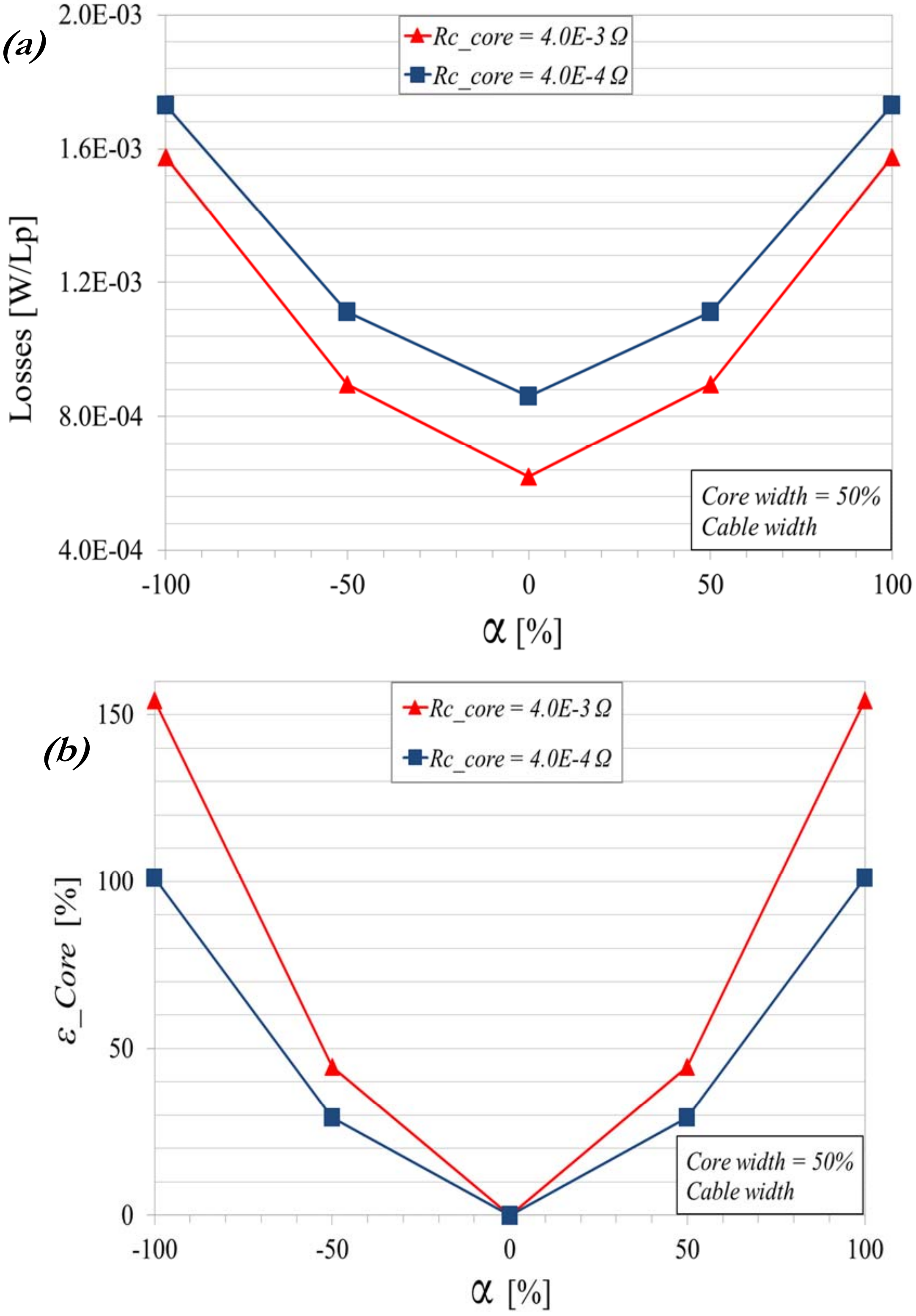

*Fig. 79. (a) Simulation results for losses, varying the positioning of the core inside the cable, setting the width of the core equal to 50% of the cable width; (b) variation between the shifted case and the centered case. In both charts different Rc_core values are displayed.*

As it is possible to see from Fig. 78, higher is the shifting of the core and higher is the value of losses compared to the case of perfectly centered core (this is a confirmation of what reported in literature [15]); the larger is the size of the core and the greater this effect is.

Subsequently, the experiment is repeated fixing the size of the core (equal to 50% of the cable width) and varying the value of *Rc_core*; results are presented in Fig. 79. Higher is the resistance of the core and the greater is the increase of losses, shifting core from its central position.

Therefore, it is necessary to control the positioning of the core, trying to maintain it as central as possible, especially for core whose effect is important: those that cover large portions of the cable and have particularly high values of resistance compared to the resistance between non-adjacent strands of the uncored cable.

## *5.2.2 Self-validation of the model with the core*

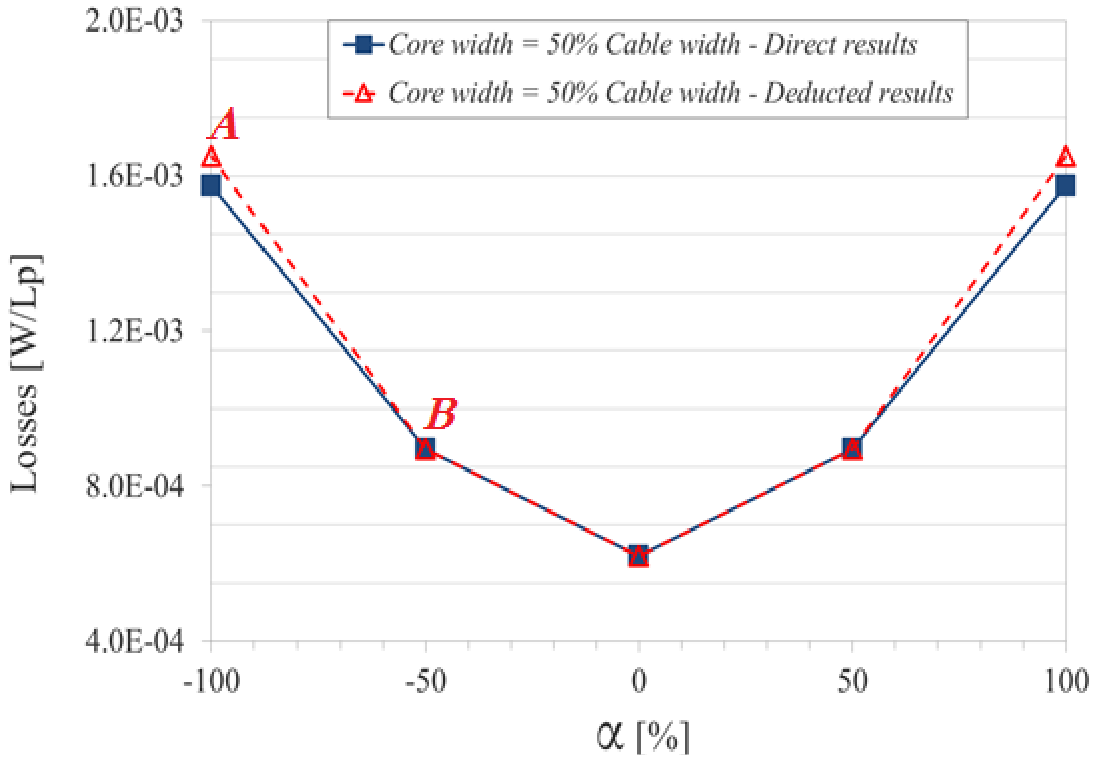

*Fig. 80. Losses for a cored cable with core width equal to 50% of the cable width, obtained through direct simulations (blue curve), or performing operations on simulation results for different core width and α values (red curve). The procedure to derive points A and B is described in Fig. 81 - 82.*

To obtain a proper validation of the model considering core, a study similar to the one reported in Chapter 4.2 for the uncored cable should be carried, comparing simulation results with an analytical formulae. At the writing of this thesis, a correct formula with which to operate this comparison has not been found in literature. Notwithstanding this, it is possible to verify the self-consistency of the method, keeping in mind that it does not constitutes a proper validation of the method with core.

For self-validation of the method with the core, it is verified that loss curves can be deduced without realizing direct simulations, but performing operations on curves obtained using different parameters, taking advantage of the geometric properties of the cable. For the case analysed in Fig.80, the losses curve for a cored cable width core width = 50% of the cable width is reproduced without direct simulations but deducing its points by means of division and sum operations on points of other curves. The derivation of points of the red curve is explained in Fig. 81 - 82; points not described can be easily deduced from the cable symmetry.
Since the curves in Fig. 80 are very similar, it is possible to conclude that the self-consistency of the model with core is verified.

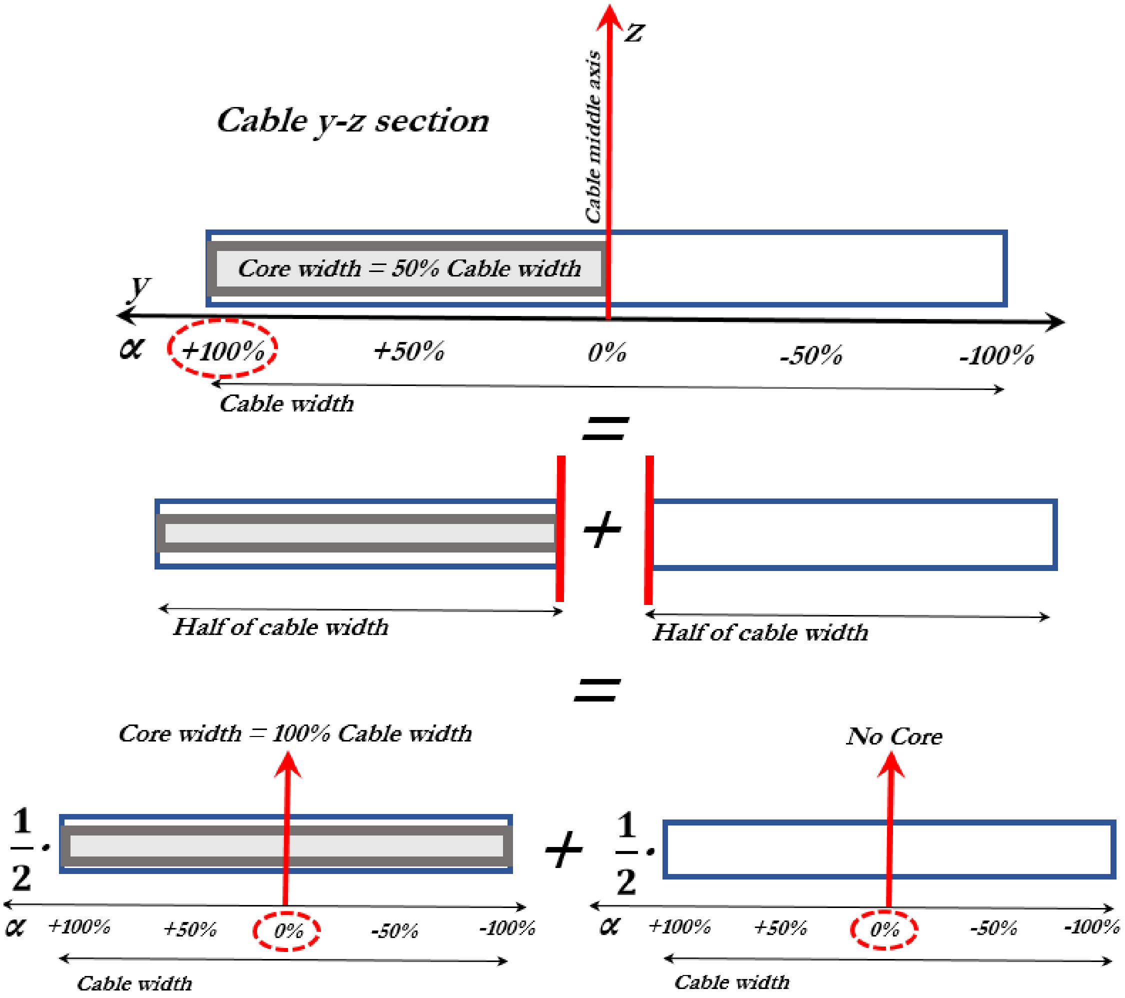

*Fig. 81. Procedure to deduce point A of Fig. 80. Each of the two halves of the y-z cross-section of a cable can be considered separately: they can be seen in turn, as the half of other cables having different characteristics. Thus, summing half of the losses for a cable with core width = 100% cable width placed centrally (left half), and half of the losses for a cable without core (right half), it is equivalent to the direct calculation of point A.*

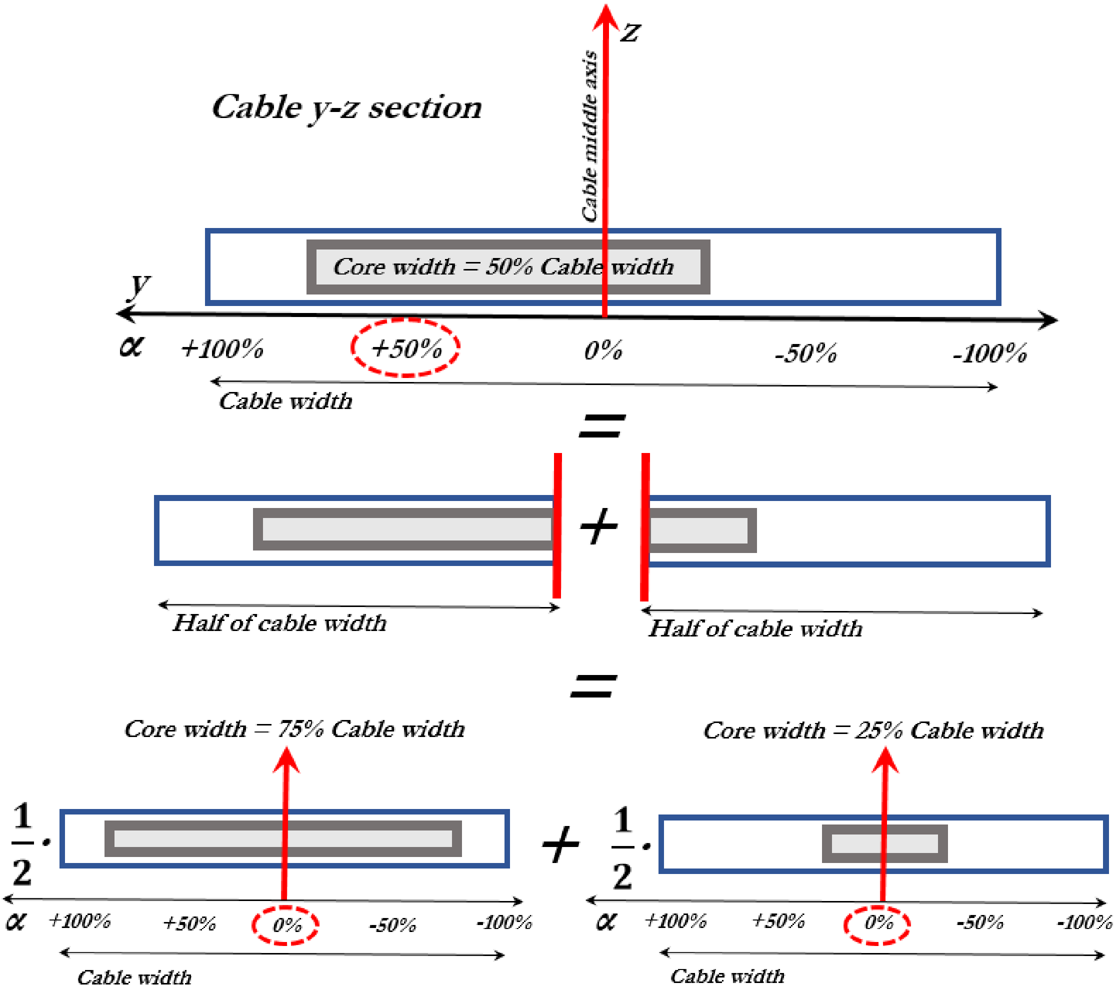

*Fig. 82. Procedure to deduce point B of Fig. 80. Each of the two halves of the y-z cross-section of a cable can be considered separately: they can be seen in turn, as the half of other cables having different characteristics. Thus, summing half of the losses for a cable with core width = 75% cable width placed centrally (left half), and half of the losses for a cable with core width = 25% cable width placed centrally (right half), it is equivalent to the direct calculation of point B.*

## *5.2.3 Conductance function analysis*

It is interesting to analyse how the trend of the conductance function changes in presence of the core, since losses distribution depends directly this function.

In Fig. 83 the conductance functions along the length of a Rutherford cable are shown, with the characteristics of the baseline study case described in chapter 4.2.1, for the couple of strands number 1 and 11. A cable length equal to two twist pitches is considered, therefore four peaks of conductance (corresponding to four contacts) are present. In Fig.71 (a) the cable is uncored, in (b) a core is inserted with core width = 50% cable width and *Rc_core* equal to $4.0 \cdot 10^{-3}$ Ω, covering all contacts between the couple of strands, while in (c) the same core is shifted with α = 50% ; in case (c) some contacts remain covered by the core while others become uncovered.

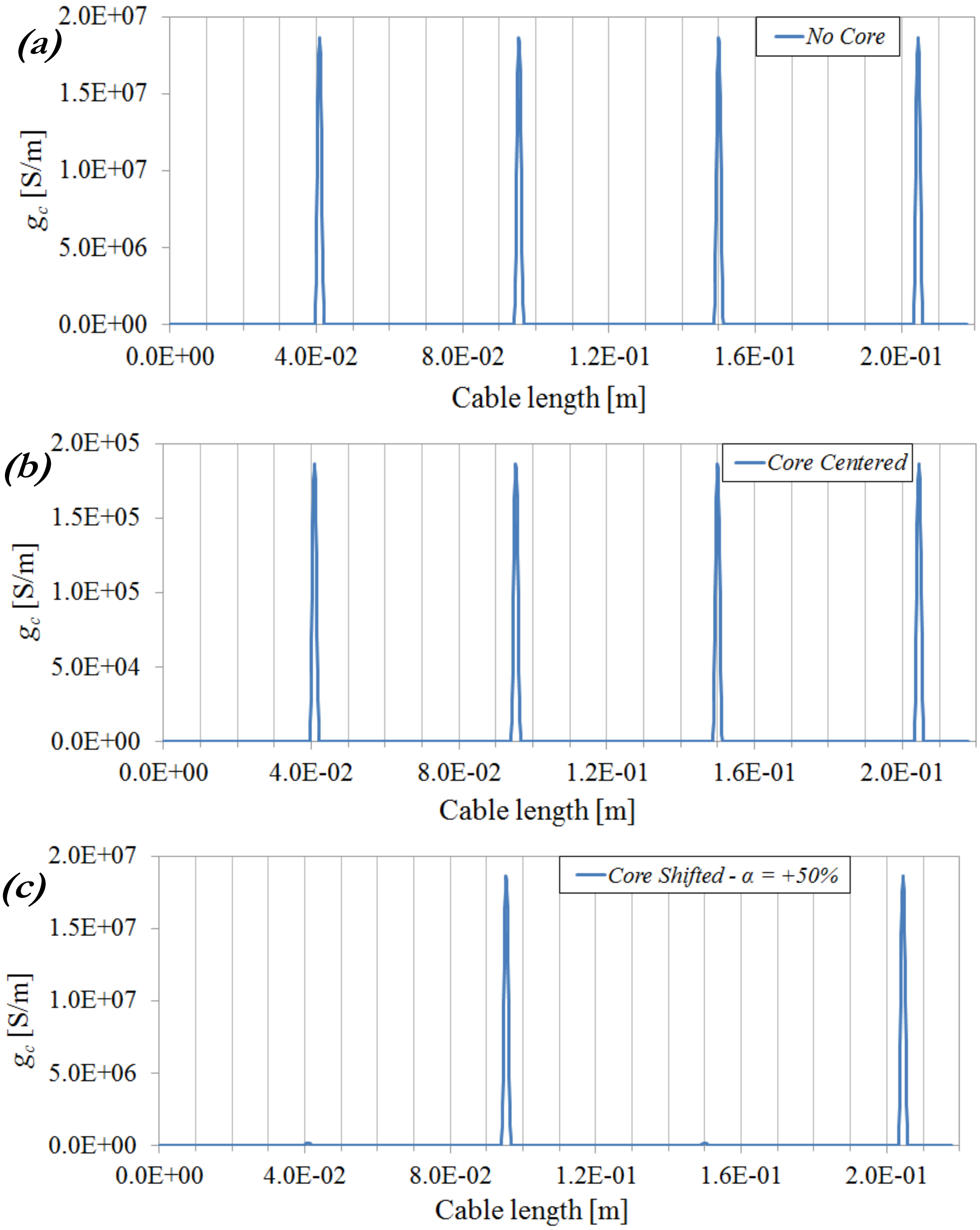

*Fig 83. Conductance functions between strands number 1 and 11 of a Rutherford cable with characteristics equal to the baseline study case, considering three different options: (a) uncored cable, (b) insertion of a centered core with core width = 50% cable width and Rc_core equal to 4.0E-3 Ω, (c) the same cable as the precedent but with α = +50%.*

Charts show that when all contacts are covered by the core (Fig.83 (b)), the order of magnitude of the height of the peaks in the conductance function is lower compared to the uncored case (Fig. 83 (a)), and the decrease is proportional to the ratio between the *Rc* value of the uncored case and the *Rc_core* value. When the core is shifted (Fig. 83 (c)), covered contacts assumes a different order of magnitude from uncovered contacts, within the same function. Therefore, the symmetry of the function is lost, but the periodicity of one twist pitch remains (after a twist pitch, the contact between the two strands is on the same transverse position, compared to the cable middle axis).
From this, it follows that even the distribution of losses and currents will no longer be symmetrical. In contact points characterized by higher peaks of conductance (in which the resistance is equal to the *Rc* value for the uncored cables), the intensity of currents and losses will be higher compared to the contact points characterized by lower conductance peaks (in which the resistance is equal to the *Rc_core* value).

## *5.3 Results*

To obtain the distribution of currents and losses in Rutherford cables with core, simulations are performed considering the characteristics of the baseline study case and a cable length equal to two twist pitches; then a core is inserted. *Rc_core* value is set equal to $4.0 \cdot 10^{-3}\ \Omega$ for all cases, while core width and position are changed.

### *5.3.1 Centered core case*

The first study is performed considering a centered core ($\alpha = 0\%$).

In Fig. 84 currents distributions along the cable length are shown, with core width equal to the 50% (Fig. 84 (a)) and the 75% (Fig. 84 (b)) of the cable width. Same results are reported along the width of the cable, in Fig. 85. It is useful to compare these distributions with those obtained for the uncored cable case, shown in Fig 54 - 55. The more relevant comparisons are those referred to the cable width: from these charts, it is easier to estimate the effect of the core.

As it is possible to see, in each strand current is almost constant in correspondence of the core position; that means there is no exchange of current between strands because the core acts as an insulator. Currents can flow in the areas at the core sides; wider is the core width, lower is the area in which current can flow. Consequently, smaller is this area, the lower is the intensity of currents, which cannot find enough space to fully develop as they do in the uncored case. Furthermore, if the core is centered charts are perfectly symmetrical.

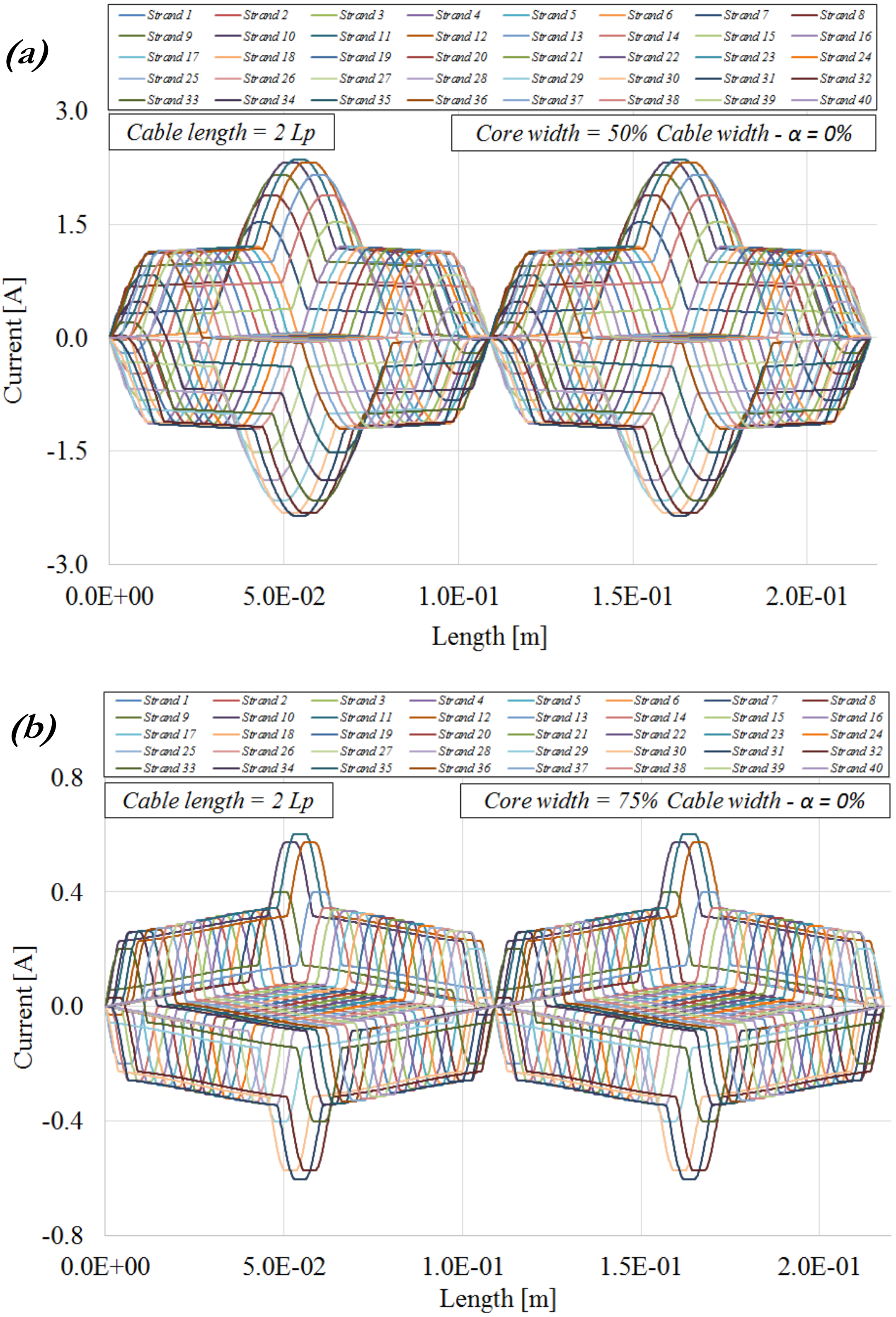

*Fig 84. Induced coupling currents distribution along the cable length, for a 40 strand Rutherford cable with a centered core, considering a cable length of two twist pitches. Core width is set equal to (a) 50% and (b) 75% of the cable width.*

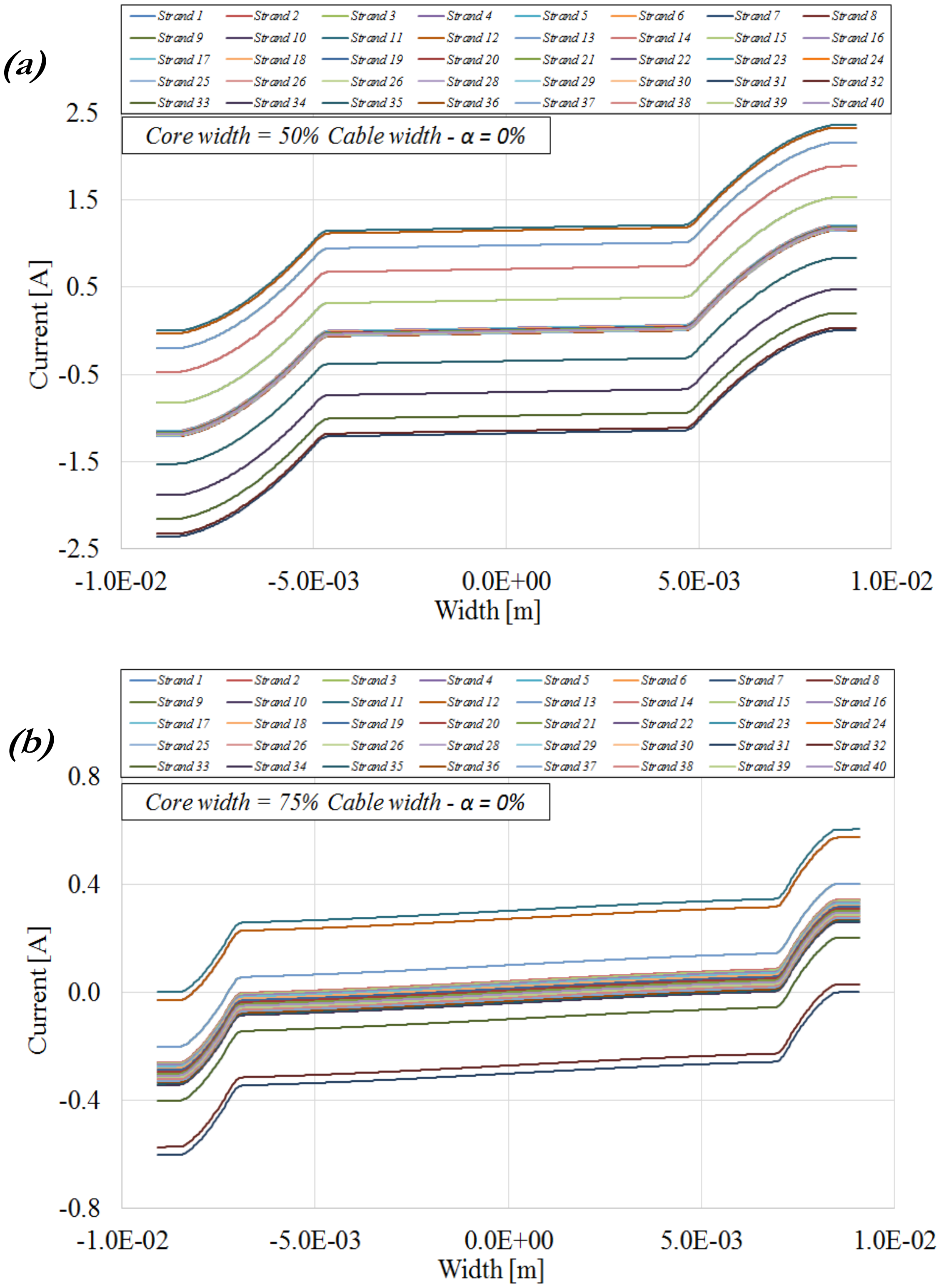

*Fig 85. Induced coupling currents distribution along the cable width, for a 40 strand Rutherford cable with a centered core. Core width is set equal to (a) 50% and (b) 75% of the cable width.*

In Fig. 86 losses distributions along the cable length are shown, considering a core width equal to the 50% (Fig. 86 (a)) and the 75% (Fig. 86 (b)) of the cable width; losses are displayed for a single strand for more clarity. Same results are reported along the width of the cable, in Fig. 87, in this case the curves are displayed for all 40 strands, all of which are exactly superimposed in the graph. In this case it is useful to compare these distributions with the charts shown in Fig. 56 -58 for the uncored cable.

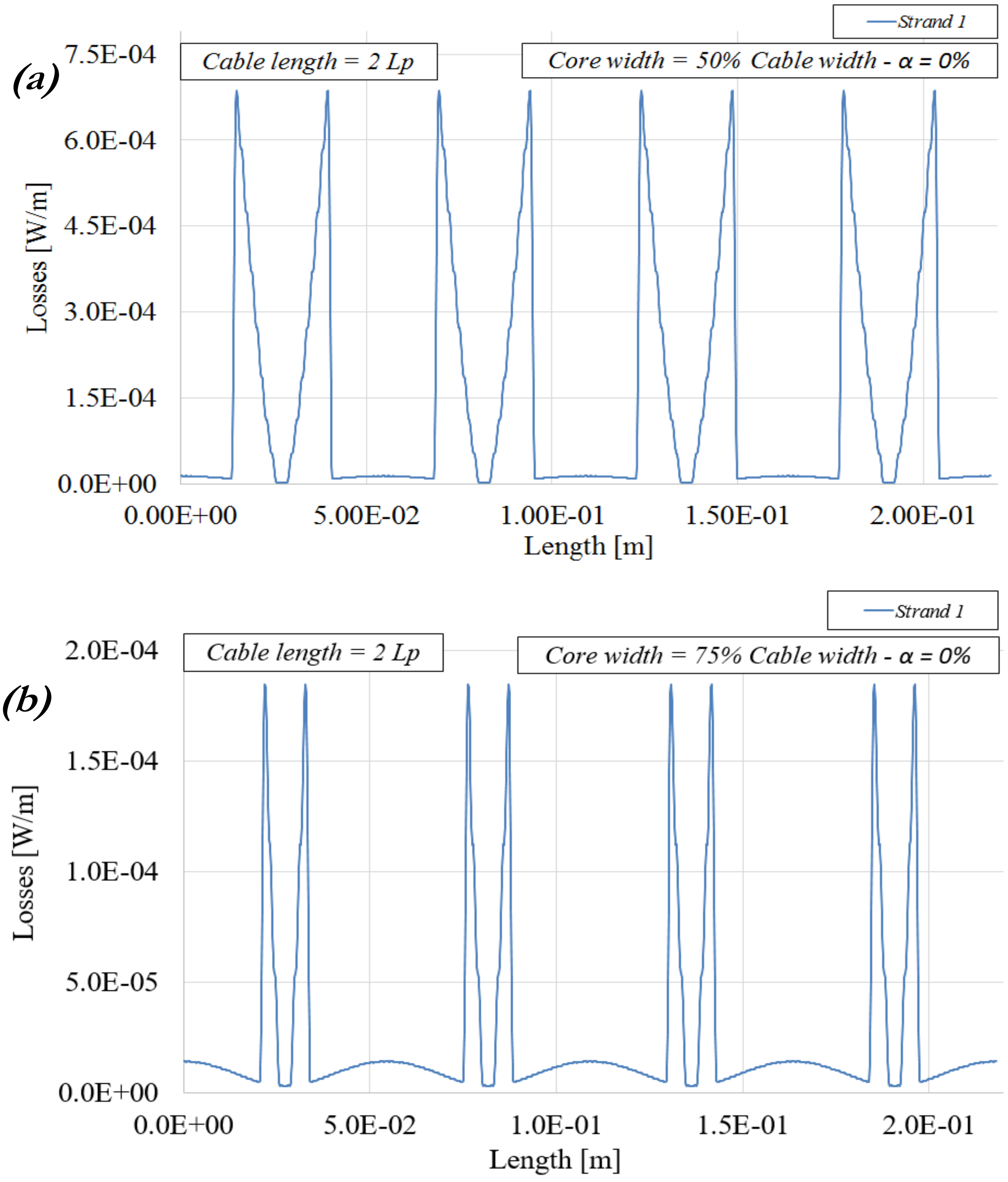

*Fig 86. Losses distribution along the cable length, for one single strand of a 40 strand Rutherford cable with a centered core, considering a cable length of two twist pitches. Core width is set equal to (a) 50% and (b) 75% of the cable width.*

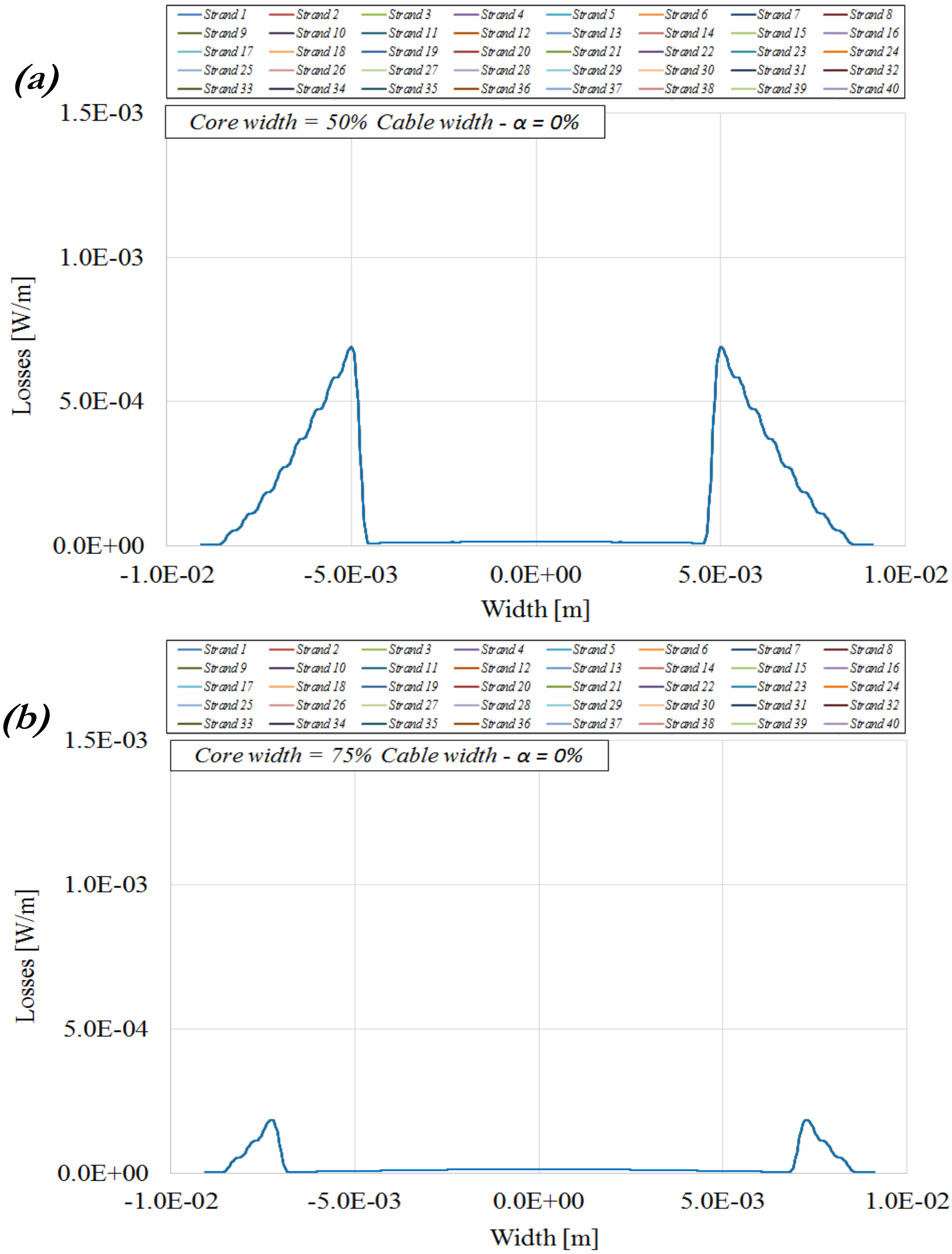

*Fig 87. Losses distribution along the cable width, for a 40 strand Rutherford cable with a centered core. Core width is set equal to (a) 50% and (b) 75% of the cable width.*

As it is possible to from Fig. 87, the loss curve is lowered in correspondence of the core position. In particular, given the high value of the ratio between the resistance *Rc* of the uncored cable and *Rc_core*, the function is suppressed down to negligible values. On core sides, the loss distribution assumes the identical profile of the uncored case. Wider is the core and greater this effect is.

Moreover, it is possible to draw a conclusion about the width of the core to be used in a multistrand cable. With reference to the loss distributions in Fig. 58-87, it is visible how curves assume very low values at the cable sides, reaching zero value at the cable extremities, regardless of the presence of the core. From conclusion presented in Chapter 5.2.1, it results that total losses are lower, the greater is the width of the core; therefore, it may seem obvious that using a core that covers 100% of the cable width is the best solution. However, this is a particularly stringent condition, which it is not always easy to ensure due to inhomogeineties in the core insertion or core spreading within the cable. Nonetheless, there is no need that the core width is exactly equal the cable width, but the range of its size is broader: although the cable side sections are left uncovered, the losses resulting from these contacts are very low and practically negligible. Therefore, even smaller dimensions of the core width are acceptable; the tolerance range depends on the individual case.

## *5.3.2 Shifted core case*

The second study is performed considering the shifting of the core ($\alpha \neq 0\%$).

In Fig. 88 - 90 currents distributions along the cable length are shown, while in Fig. 89 – 91 the same distributions are displayed along the cable width. In Fig. 88 – 89 cables with core width equal to 50% of the cable width are simulated, while in Fig. 90 – 91 cables width core width equal to 75% of the cable width are simulated. For all figures, the reference (a) represents a core shifted of value $\alpha = +50\%$, while reference (b) represents a core shifted of value $\alpha = +100\%$. Negative values of $\alpha$ are not realized, due to the symmetry of the cable, as demonstrated in Chapter 5.2.1. It is useful to compare these charts with those referred to the uncored case (Fig. 54 – 5) and the centered core cases (Fig. 84 – 85). As for centered results, the more relevant comparisons are those referred to the cable width: from these charts, it is easier to estimate the effect of the core.

When the core is shifted the symmetry of the system is lost: the currents are not able to redistribute equally at the core sides. This create a wider area at one of the cable sides in which contacts are not covered by the core and currents are free to flow among strands (it is the side opposite to the direction of the shifting). In this area the currents intensity is greater compared to the centered core case. On the contrary, at the opposite side of the cable, the area in which currents circulate between strands is smaller and therefore the currents intensity is lower; but this effect cannot "balance" the wider area, thus total current is greater for a shifted core compared to a centered core. The wider is the core width and the greater this effect appears.

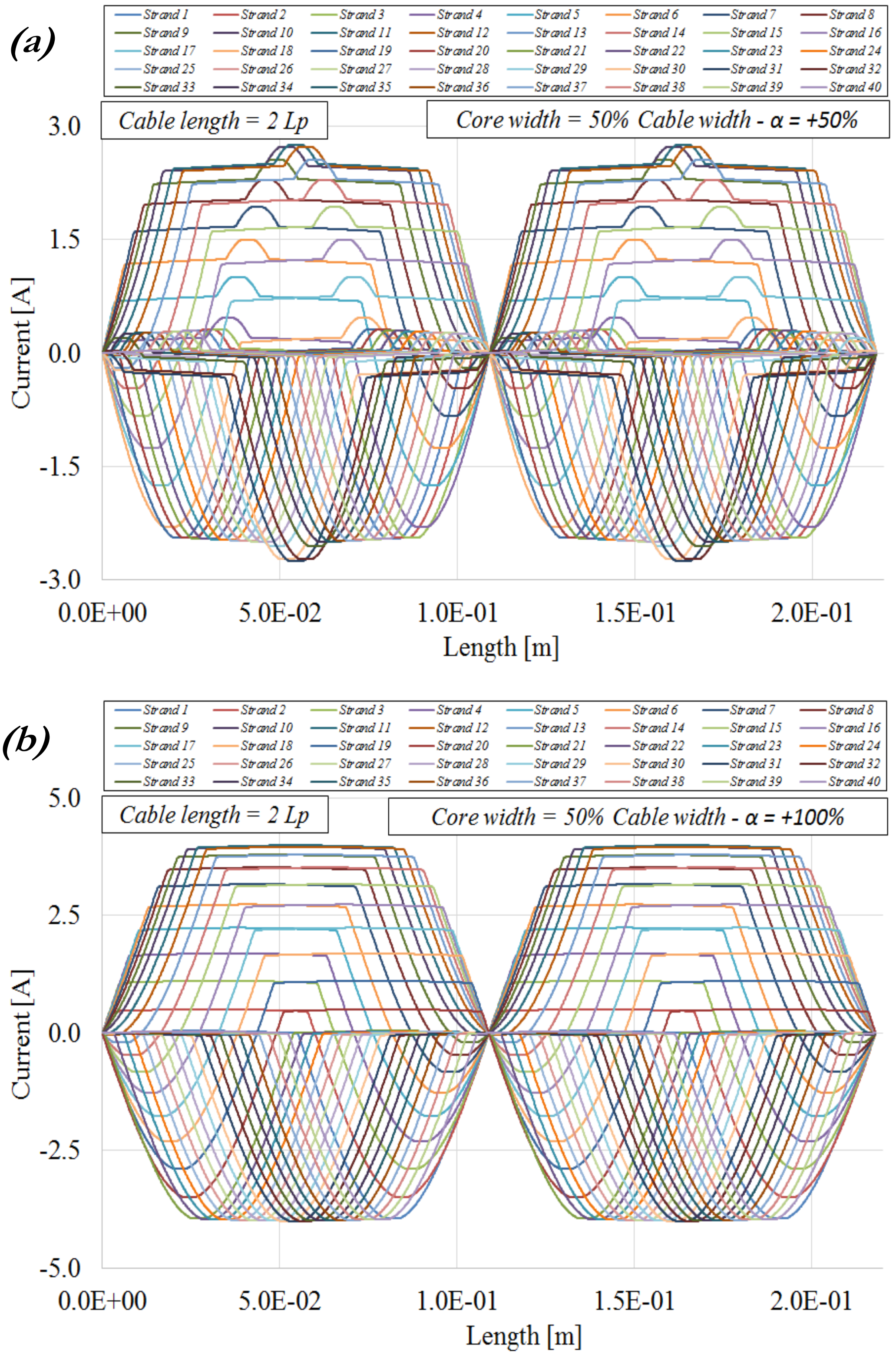

*Fig 88. Induced coupling currents distribution along the cable width, for a 40 strand Rutherford cable, considering a cable length of two twist pitches and with core width equal to 50% of the cable width. α set equal to (a) +50% and (b) +100%.*

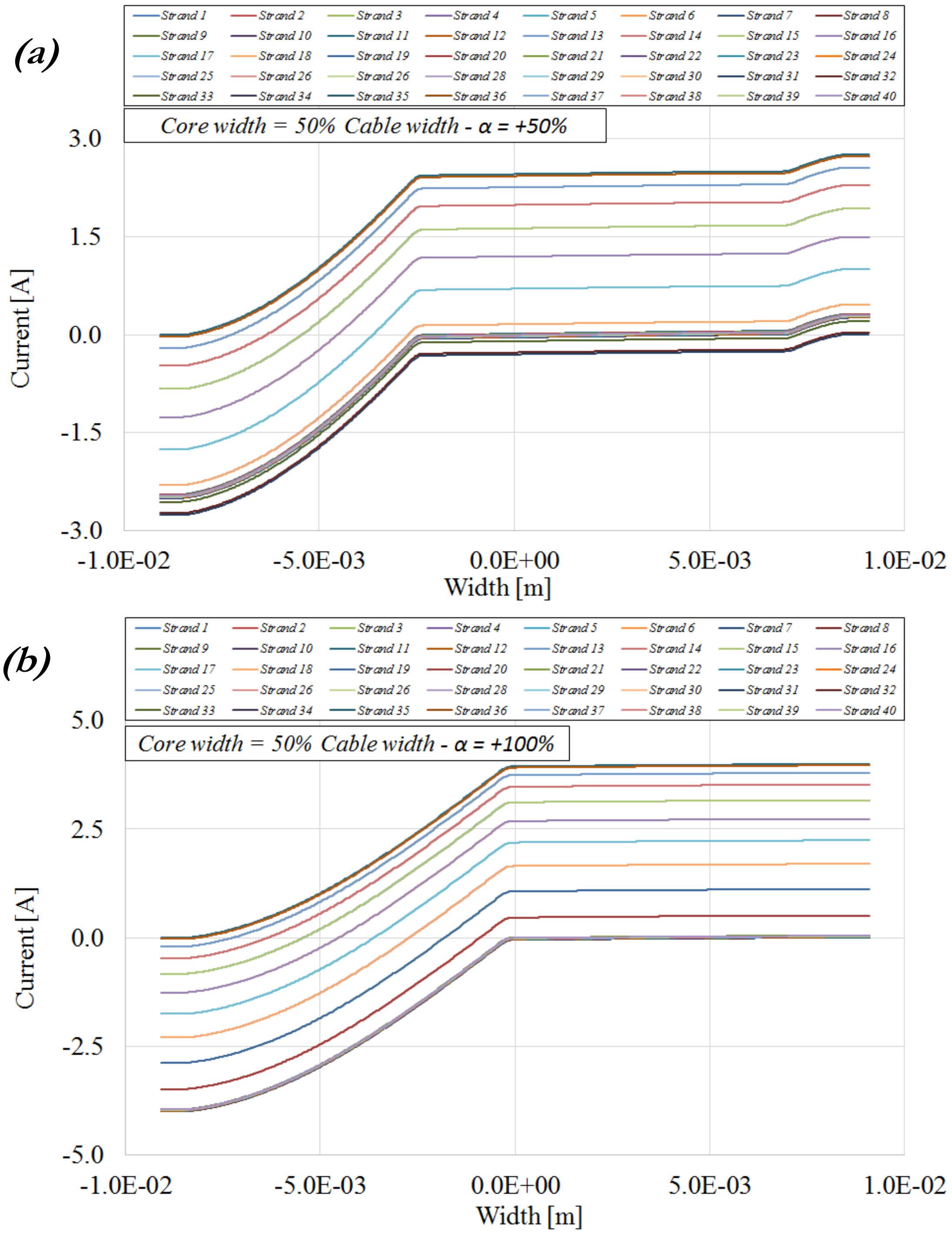

*Fig 89. Induced coupling currents distribution along the cable width, for a 40 strand Rutherford cable, with core width equal to 50% of the cable width. α set equal to (a) +50% and (b) +100%.*

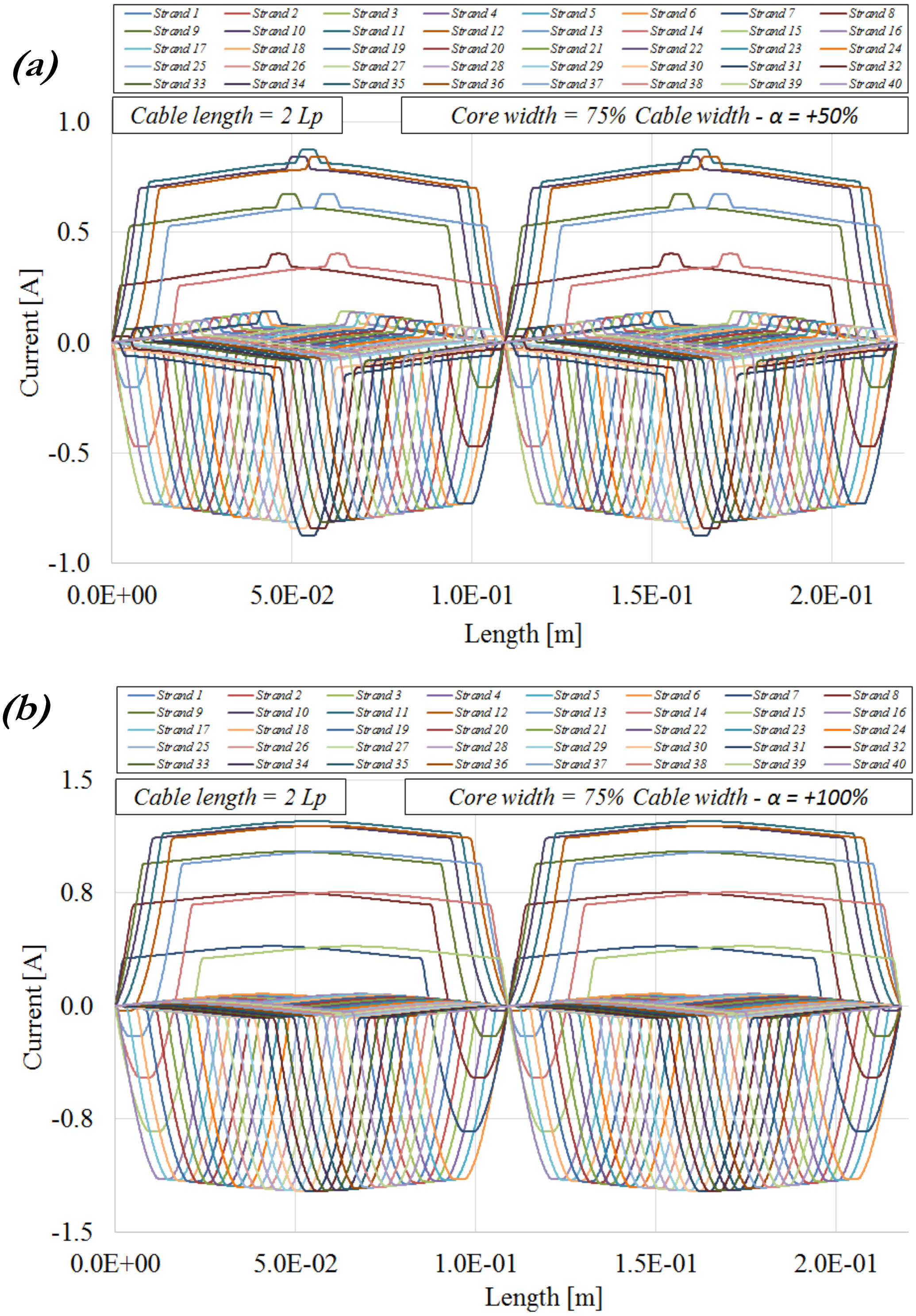

*Fig 90. Induced coupling currents distribution along the cable length, for a 40 strand Rutherford cable, considering a cable length of two twist pitches and with core width equal to 75% of the cable width. α set equal to (a) +50% and (b) +100%.*

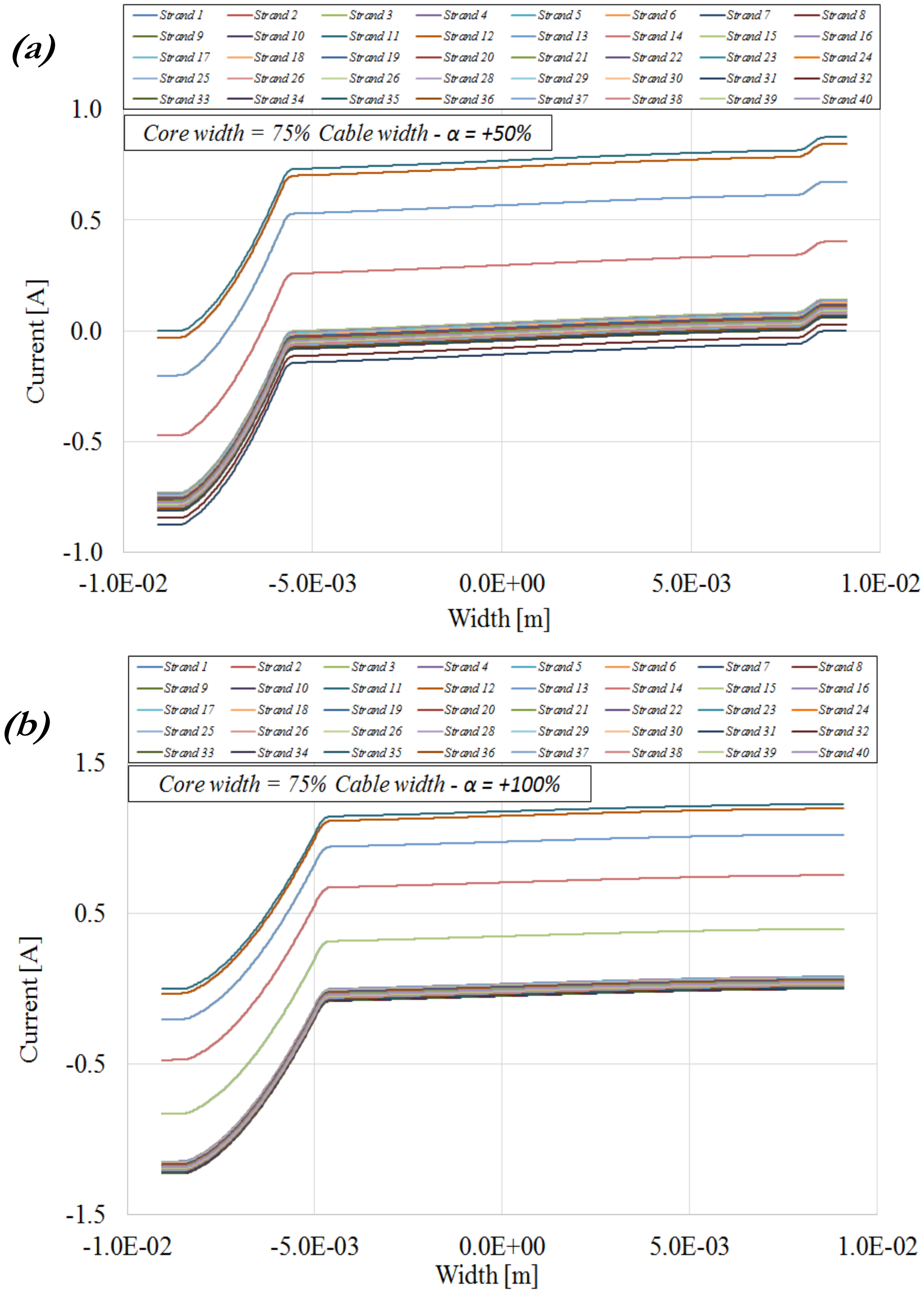

*Fig 91. Induced coupling currents distribution along the cable width, for a 40 strand Rutherford cable, with core width equal to 75% of the cable width. α set equal to (a) +50% and (b) +100%.*

In Fig. 92 - 94 losses distributions along the cable length are shown, while in Fig. 93 – 95 the same distributions are displayed along the cable width. In Fig. 92 – 93 cables with core width equal to 50% of the cable width are simulated, while in Fig. 94 – 95 cables width core width equal to 75% of the cable width are simulated. For all figures, the reference (a) represents a core shifted of value α = +50%, while reference (b) represents a core shifted of value α = +100%. It is useful to compare these charts with those referred to the uncored case (Fig. 56 – 58) and the centered core cases (Fig. 86 – 87). As for centered results, the more relevant comparisons are those referred to the cable width: from these charts, it is easier to estimate the effect of the core.

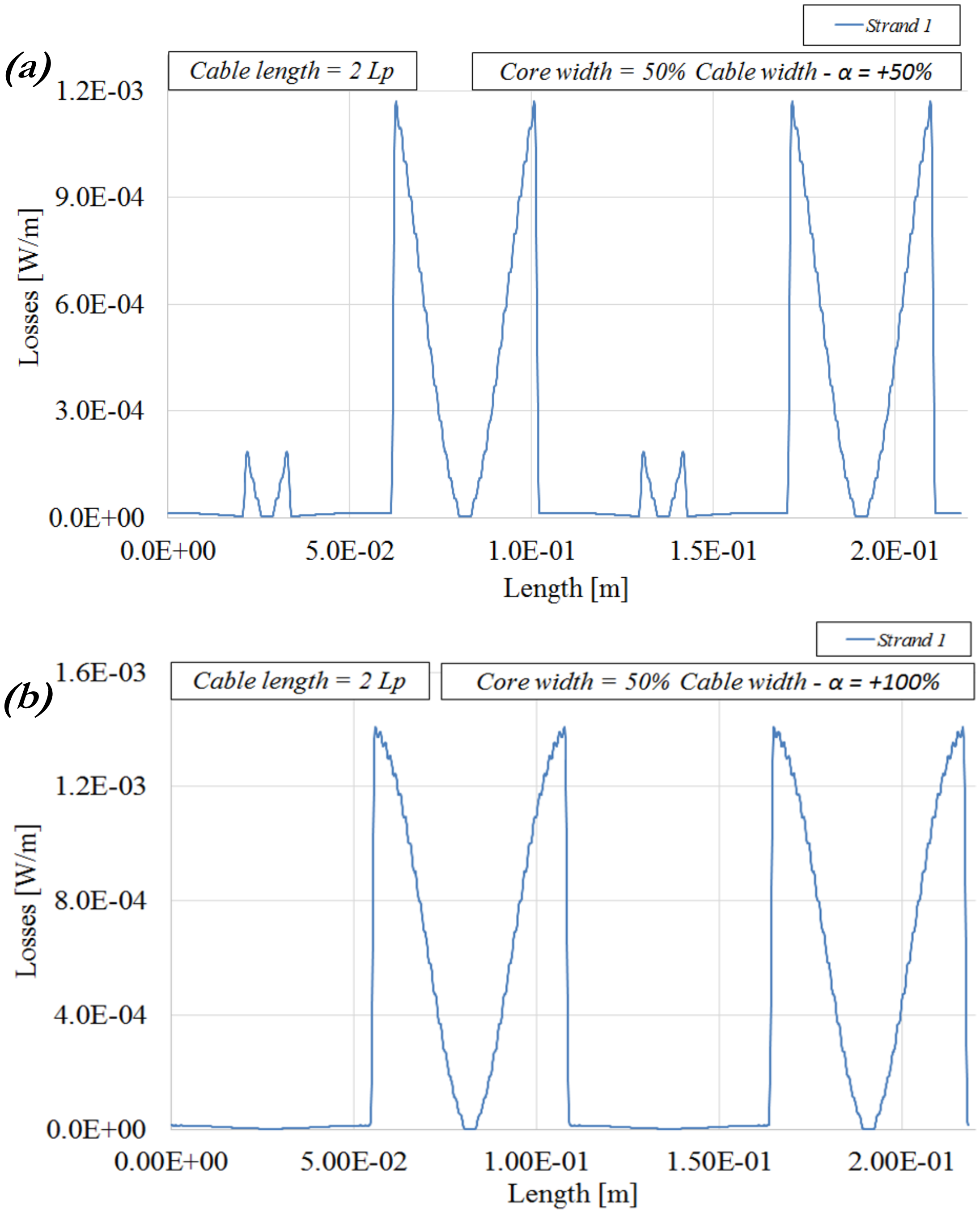

*Fig 92. Losses distribution along the cable length, for one single strand of a 40 strand Rutherford cable, considering a cable length of two twist pitches and with core width equal to 50% of the cable width. α set equal to (a) +50% and (b) +100%.*

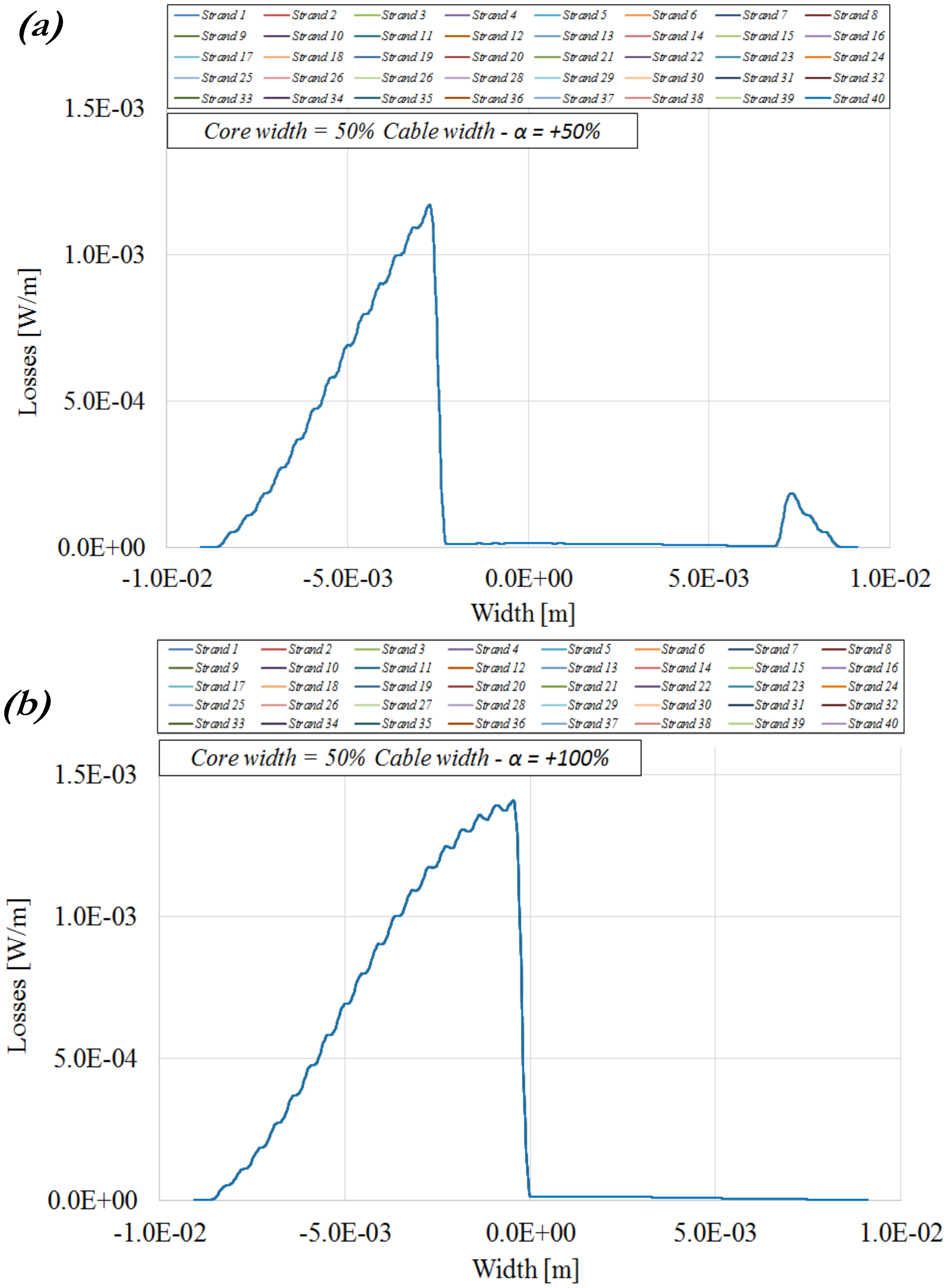

*Fig 93. Losses distribution along the cable width, for a 40 strand Rutherford cable, with core width equal to 50% of the cable width. α set equal to (a) +50% and (b) +100%.*

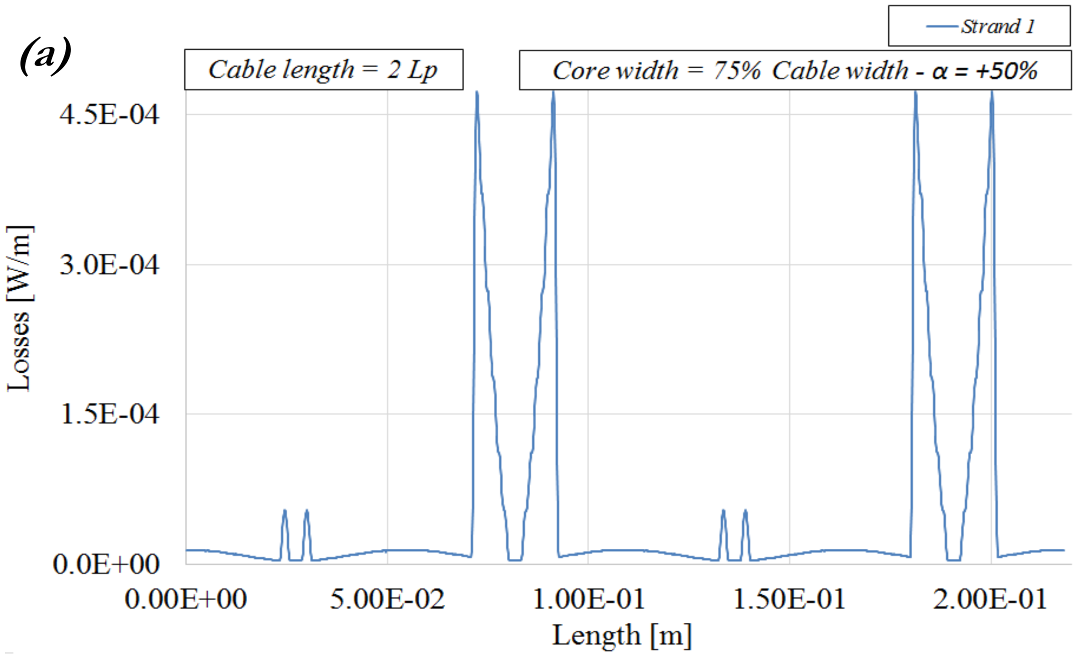

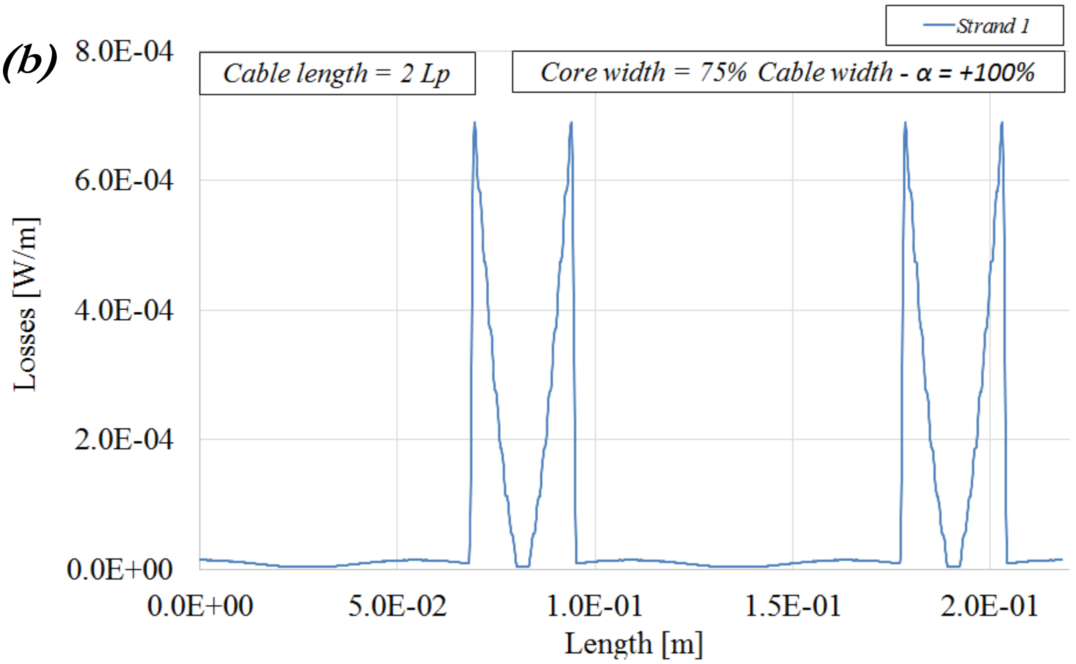

*Fig 94. Losses distribution along the cable length, for one single strand of a 40 strand Rutherford cable, considering a cable length of two twist pitches and with core width equal to 75% of the cable width. α set equal to (a) +50% and (b) +100%.*

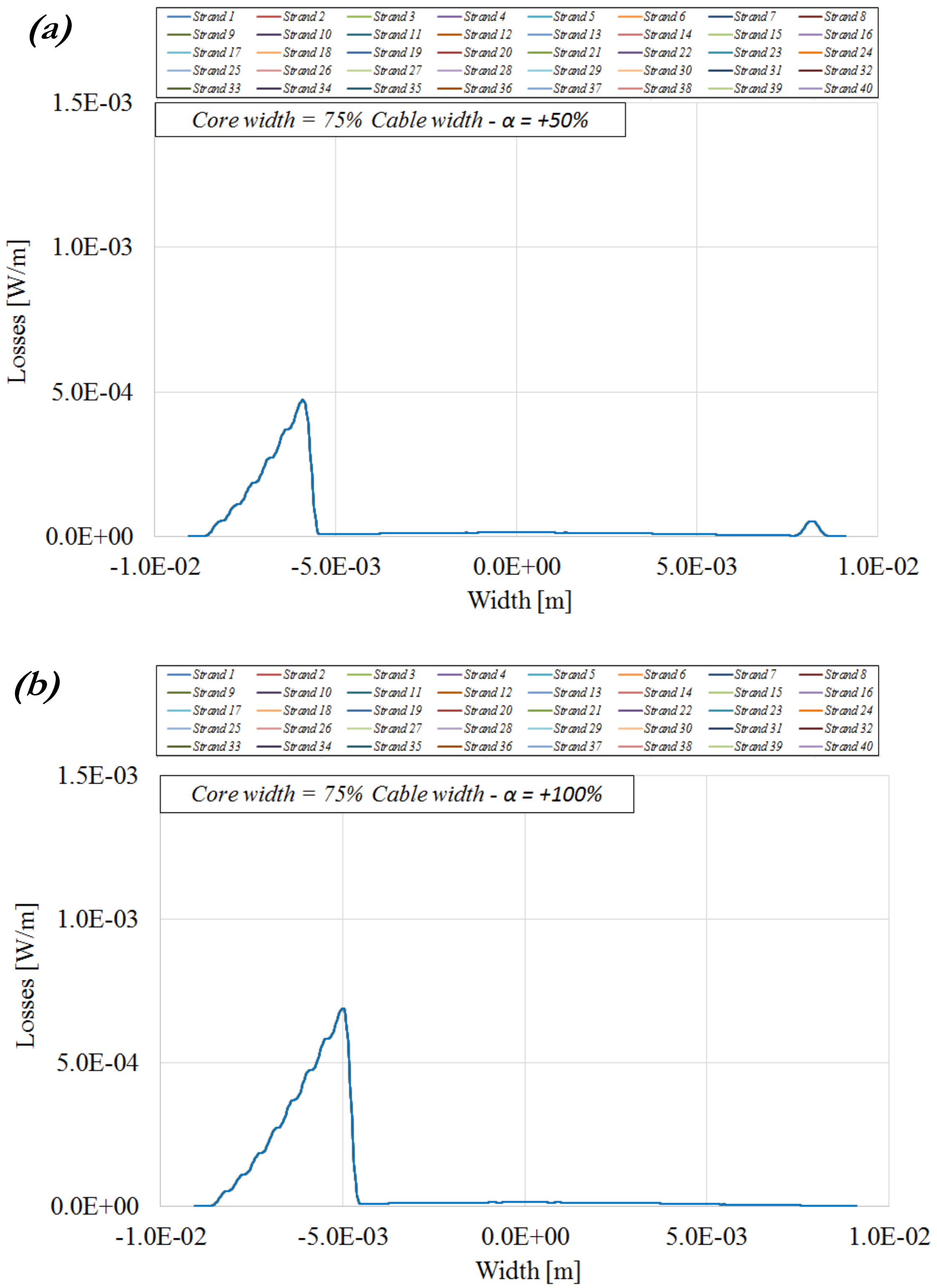

*Fig 95. Losses distribution along the cable width, for a 40 strand Rutherford cable, with core width equal to 75% of the cable width. α set equal to (a) +50% and (b) +100%.*

Shifting the core, the loss function is “cut” in a non-symmetrical way: while the cable side section covered by the core has the same width (equal to the width of the core), the impact on losses distribution is not the same compared to the case of centered core. Shifting the core, its effect to "cut" the loss function is applied to areas nearer to the cable sides, while on the other hand, areas closer to the cable center remain uncovered. In terms of “core power”, this produces a negative effect since the losses distribution has a Gaussian trend: in fact, shifting the core means to reduce the loss function in areas with low or negligible values, causing instead an increase in areas affected by the higher values (the center of the cable/Gaussian). The worst cases are precisely when the shifting of the core reaches its maximum values (α = ± 100%). Al this reasoning, obviously, has the same impact on total losses, which are the integral of the loss distribution.

Finally, all charts for losses along the cable width are compared in Fig. 96, considering all width and α values tested. Greater are the values of core width and α, and lower is the effect of the core to reduce losses. This represents a physical explanation of conclusion already reported in Chapter 5.2.1. It is possible to conclude that great care should be taken to ensure that the core is centrally positioned within the width of the cable, especially when wide and particularly resistive cores are involved.

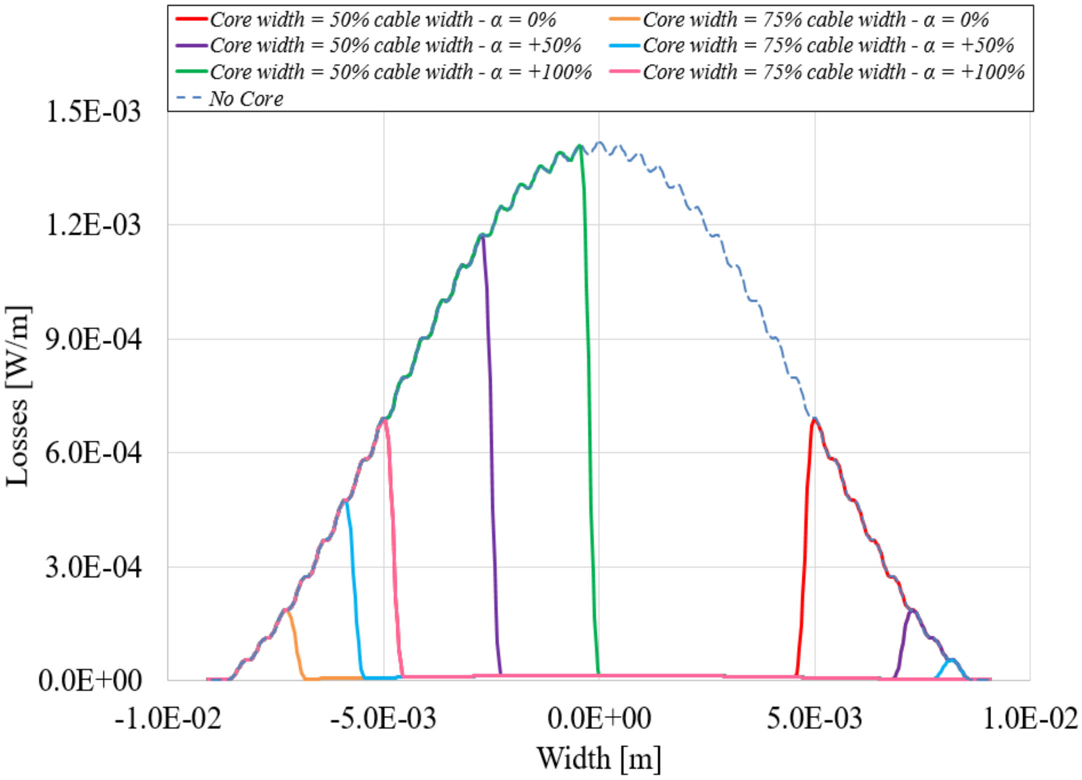

*Fig 96. Losses distribution along the cable width, for a 40 strand Rutherford cable, considering different core width and α values. Such distributions are the same for all strands, since all functions are superimposed.*

# Conclusions

The aim of this work is the analysis of the distribution of *interstrand coupling currents* and their relative losses, induced in Rutherford cables for particle accelerators by electrodynamic transients. This work is carried out by means of a continuum model where elements of the conductance matrix are not considered uniform along the cable length, in order to reach the proper level of detail required to simulate short-range coupling currents. This model is implemented in the software THEA for the calculation of current distributions and losses. Special attention is given in illustrating the theoretical principles according to which the functions of conductance, inductance and induced voltage are implemented in the code.

Simulations are performed considering the characteristics of the *$Nb_3Sn$* Rutherford cable used in low-β quadrupoles (*MQXF*) for the *High-Luminosity* project of LHC. The transient considered is a time-varying magnetic field applied normal to the cable main face. A constant ramp rate is assumed for simplicity. However, the model implemented can simulate transients in cables, regardless of the cable geometry and properties, and of the conditions of the magnetic field.

A convergence study is performed to assess the minimum number of mesh elements to reach convergence. The result of this study is that 250 elements per twist pitch are sufficient to reach convergence. The model developed is validated comparing results with analytical formulae, obtaining an excellent agreement.

The dependence of losses on main system parameters is studied. Significant dependence of losses on *$R_c$* is found. Particular attention is given to the choice of the cable length and boundary conditions, leading to the following conclusions. By appropriately selecting the minimum length of the cable sample and the boundary conditions of the system, the model is effective in simulating long cables and, at the same time, allowing comparisons with results obtained experimentally on real samples. Setting boundary conditions of zero current, a cable sample of a length equal to one twist pitch allows to obtain the desired results; if equipotential boundary conditions are set, longer cable sample are needed to achieve convergence. Moreover, for sufficiently long cables and considering cable sections distant enough from the boundaries, losses distribution is independent of the choice of boundary conditions.

Then, one of the main technical strategies to reduce losses is studied: the insertion of a resistive core within the cable. The self-consistency of the model including the stainless steel core is proved. The effectiveness of the core is demonstrated, and the impact of the core main parameters is analysed. Wide cores are more effective in reducing losses, as well as more resistive cores. Moreover, a condition for the size of the core is deduced: it is not fundamental that the core has a width equal to the cable width, since losses at cable sides have negligible values. Therefore, even smaller cores are acceptable.

Particular attention is given to study the influence of the core positioning within the cable, simulating situations where the core is shifted from the central position. It appears that any shift from the central position reduces the effect of the core on losses, proportionally to the extent of the shift. Therefore, it is concluded that special attention should be given to ensure that a core is inserted in central position, especially for particularly wide and resistive cores.

Finally, both the uncored and the cored model here presented, can be considered as useful predictive tools to simulate the distribution of *interstrand coupling currents* and the corresponding losses within Rutherford cables subjected to a time-varying magnetic field. Models allow to simulate the conditions of long cables with an adequate level of detail and to compare results with experiments performed on real samples.

As a perspective, the electromagnetic model developed can be coupled with the thermo-hydraulic domain, already implemented in THEA, for a multi-physic analysis of transients, that may be relevant for the study of quench.
Another interesting development could be the search of analytical formulae for losses calculation considering a resistive core, to use as a benchmark for numerical codes and for direct assessment of the core impact in the design phase of Rutherford cables.

# *Bibliography*

[1] E. Felcini,M. Breschi and L. Bottura, *“Analysis of the Stability Margin of the High Luminosity LHC Superconducting Cables with a Multi-Strand Model”*, Master Thesis, University of Bologna, Italy, 2016.

[2] A.P. Verweij , *"Electrodynamics of Superconducting Cables in Accelerator Magnets"*, PhD Dissertation, University of Twente, The Netherlands, 1995.

[3] A.P. Verweij and H.H.J. ten Kate, *“Super coupling currents in Rutherford type of cables due to longitudinal nonhomogeneities of dB/dt”*, IEEE Transactions on Applied Superconductivity, Vol.5 Issue 2 pp. 404–407, June 1995.

[4] A.A. Akhmetov, *“Network models of superconducting cables and the results of the matrix approach to their description”*, Physica C 310, pp. 309–315, 1998.

[5] A. Devred and T. Ogitsu, *“Influence of eddy currents in superconducting particle accelerator magnets using Rutherford-type cables”*, CAS - CERN Accelerator School: Superconductivity in Particle Accelerators pp. 93-122, Hamburg, Germany, May 1995.

[6] A.A. Akhmetov, A. Devred and T. Ogitsu, *“Periodicity of Crossover Currents in a Rutherford Type Cable Subjected to a Time Dependent Magnetic Field”*, Journal of Applied Physics 75, pp. 3176-3183, September 1993.

[7] A.A. Akhmetov, L. Bottura, M. Breschi and P. L. Ribani, *“A theoretical investigation on current imbalance in flat two-layer superconducting cables”*, Cryogenics, Vol.40 Issue 8, pp. 627-635, August 2000.

[8] A.A. Akhmetov, L. Bottura and M. Breschi, *“A continuum model for current distribution in Rutherford cables”,* IEEE Transactions on Applied Superconductivity, Vol.11 Issue 1 pp. 2138 - 2141, Mar 2001.

[9] L. Bottura, *“Modelling stability in superconducting cables”*, Physica C: Superconductivity, Vol.310 Issues 1–4 pp. 316–326, December 1998

[10] L. Bottura, M. Breschi and C. Rosso, *“Influence of contact conductance longitudinal variations on current distribution in multistrand cables”*, CRYO/03/033, December 2003.

[11] L. Bottura, *"CryoSoft code THEA v. 2.2"*, December 2013

[12] G. Willering, *"Stability of superconducting Rutherford cables for accelerator magnets",* PhD Dissertation, University of Twente, The Netherlands, 2009.

[13] A.A. Akhmetov, *"Compatibility of two basic models describing the a.c. loss and eddy currents in flat superconducting cables"*, Cryogenics, Vol. 40 Issue 7 pp. 445–457, January 2000.

[14] E. W. Collings *et al.*, *"AC Loss and Contact Resistance In Copper-Stabilized* $Nb_3Al$ *Rutherford Cables with and without a Stainless Steel Core"*, IEEE Transactions on Applied Superconductivity, Vol.10 Issue 1 pp. 1196-1199, March 2000.

[15] E.W. Collings *et al., "Effects of Core Type, Placement, and Width on the Estimated Interstrand Coupling Properties of XF-Type* $Nb_3Sn$ *Rutherford cables"*, IEEE Transactions on Applied Superconductivity, Vol.25 Issue 3, June 2015.

[16] V. Augelli, Notes from lectures *"Fisica degli Stati Condensati"*, University of Bari, Italy, 2015.

[17] V.Z. Kresin and S.A. Wolf, *"Fundamentals of Superconductivity"*, Ed. by Springer, June 1990.

[18] D. Van Delft and P. Kes, *"The discovery of superconductivity"*, Physics Today, Vol. 63 Issue 9 pp. 38-43, September 2010.

[19] M.E.G.Hadlow, J.A. Baylis and B. C. Lindley, *"Superconductivity and its applications to power engineering"*, Proceedings of the Institution of Electrical Engineers, Vol. 119 Issue 8 pp.1001-1032, August 1972.

[20] M. Breschi and A. Morandi, Notes from lectures "*Ingegneria dei sistemi superconduttivi*", University of Bologna, Italy, 2007.

[21] David R. Lide, *"Handbook of Chemistry and Physics 88th edition"*, Ed. by CRC Press, June 2007.

[22] R.H. Siemann, *"Uses of superconductivity in particle accelerators"*, SLAC Summer Institute on Particle Physics: Lepton Hadron Scattering pp. 21-46, Stanford, USA, August 1991.

[23] P. P. Granieri, *"Heat Transfer between the Superconducting Cables of the LHC Accelerator Magnets and the Superfluid Helium Bath",* PhD Dissertation, Ecole

Polythechnique Fèdèrale de Lausanne, Suisse, 2012.

[24] N. Sammut, "*The Field Description for the LHC*", Engineering Specification, EDMS: LHC-CES-0012, CERN - Geneva, Switzerland, May 2008.

[25] *http://home.cern*.

[26] O.S. Brüning *et al., "LHC Design Report Vol.1: The LHC Main Ring"*, Report n° CERN-2004-003-V-1, CERN - Geneva, Switzerland, June 2004.

[27] G. Apollinari, *"High-field Magnet Development toward the High Luminosity LHC"*, 5th International Particle Accelerator Conference, Dresden, Germany, June 2014.

[28] L. Bottura and L. Rossi, *"Superconducting Magnets for Particle Accelerators*", IEEE Transactions on Nuclear Science, Vol. 63 Issue 2 pp. 751-776, April 2016.

[29] American Magnetics Inc. 2012, *"Conductor Phenomena"*, company website.

[30] A. Bevilaqua, *"Stability Analysis of the LHC superconducting cables with a Multi-Strand model"*, Internal CERN Report, February 2015.

[31] G. Deferne *et al*., *"Measurement of LHC Superconducting Dipole and Quadrupole Magnets in Ramp Rate Conditions"*, CERN presentation, August 2007.

[32] E.W. Collings *et al*., *" Suppression and Control of Coupling Currents in Stabrite-Coated Rutherford Cable with cores of various materials and thickness",* IEEE Transactions on Applied Superconductivity, Vol. 7 Issue 2 pp. 962-966, June 1997.

[33] B. Auchmann, R. de Maria and S. Russenschuck, *"Comparative Study of inter-strand coupling current models for accelerator magnets",* 10th European Particle Accelerator Conference, Edinburgh, UK, June 2006.

[34] E.W Collings *et al*., *"Coupling Loss, Interstrand Contact Resistance, and Magnetization of Nb3Sn Rutherford cables with cores of Mg-O Tape and S-Glass ribbon"*, IEEE Transactions on Applied Superconductivity, Vol. 21 Issue 3 pp. 2367-2371, June 2011.

[35] W.M. Rapper, *"Thermal stability of Nb$_3$Sn Rutherford cables for accelerator magnets",* PhD Dissertation, University of Twente, The Netherlands, 2014.

[36] L. Bottura, *"Cable stability",* CERN Yellow Report CERN-2014-005, pp. 401-451, May 2014.

[37] G.H. Morgan, *"Eddy currents in flat metal-filled superconducting braids",* Journal of Applied Physics, Vol. 44 Issue 7 pp. 3319-3322, August 1973.

[38] F. Grover, *"Inductance Calculations"*, Ed. by Dover Publications, New York: Mineola, 2004.

[39] M. Calvi, M. Breschi, and P.L. Ribani, *"Analysis of the inductance coefficients in multistrand cables: analytical, numerical and experimental results",* IEEE Transaction on applied superconductivity, Vol. 15 Issue 3 pp. 3797-3807, September 2005.

[40] V.E. Sytnikov et *al., "Coupling losses in superconducting transposed conductors located in changing magnetic fields"*, Cryogenics, Vol. 29 Issue 9 pp. 926-930, September 1989.

[41] V.E. Sytnikov, *"Minimisation of coupling losses in multiwire superconducting cables"*, IEEE Transactions on Magnetics, Vol. 27 Issue 2 pp. 2491-2493, March 1991.

[42] V.E. Sytnikov et *al., "Study on transverse resistance and coupling losses in superconducting cables"*, IEEE Transactions on Magnetics, Vol. 27 Issue 2 pp. 2494-2498, March 1991.

[43] G. Ries and S. Takacs, *"Coupling losses in finite length of superconducting cables and in long cables partially in magnetic field"*, IEEE Transactions on Magnetics, Vol. 17 Issue 5 pp. 2281-2284, September 1981.

[44] E.W Collings *et al., "Influence of strand surface condition on interstrand contact resistance and coupling loss in NbTi-wound Rutherford cables"*, Cryogenics, Vol. 39 Issue 3 pp. 197–208, March 1999.

[45] E.W Collings *et al., "Core-suppressed AC loss and strand-moderated contact resistance in a* $Nb_3Sn$ *Rutherford cable",* Cryogenics, Vol. 39 Issue 1 pp. 1–12, January 1999.

[47] E.W Collings *et al., "Coupling current control in stabrite-coated NbTi Rutherford by varying the width of a stainless steel core"*, Advances in Cryogenic Engineering Materials, Vol. 46 Issue 1 pp. 1043-1047, 2000.

[47] E.W Collings *et al., "AC Loss of $Nb_3Sn$-based Rutherford Cables with internally and externally added Cu", IEEE Transactions on Applied Auperconductivity"*, Vol. 13 Issue 2 pp. 2376-2379, June 2003.

[48] J.D. Adam *et al*., *"Rutherford Cables with Anisotropic Transverse Resistance",* IEEE Transactions on Applied Superconductivity*,* Vol. 7 Issue 2 pp. 958-961, June 1997.

[49] E. Barzi *et al*., *"$Nb_3Sn$ RRP Strand and Rutherford Cable Development for a 15 T Dipole Demonstrator"*, IEEE Transactions on Applied Superconductivity, Vol. 26 Issue. 4 Art.n° 4804305, June 2016.

[50] E.W Collings *et al., "Coupling- and Persistent-Current Magnetizations of $Nb_3Sn$ Rutherford Cables With Cores of Stainless Steel and Woven Glass-Fiber Tape Measured by Pick-Up Coil Magnetometry"*, Ieee Transactions on Applied Superconductivity, Vol. 23 Issue. 3 Art.n° 4702305, June 2013.

[51] M. Breschi *et al.,* "*Quench propagation and stability analysis of Rutherford resistive core cables"*, Cryogenics, Vol. 46 Issues 7–8 pp. 606–614, July–August 2006

[52] M Calvi *et al*., "*Analytical Model of Thermoelectrical Behavior in Superconductive Resistive Cored Cables"*, IEEE Transactions on Applied Superconductivity, Vol. 16 Issue 2 pp. 1208-1211, June 2006.

[53] ] M Coccoli *et al.,* "*Fabrication and Performance of Nb3Sn Rutherford-Type cable with Cu added as a separate component",* IEEE Transactions on Applied Superconductivity, Vol. 14 Issue 2 pp. 971-974, August 2004.

[54] E.W Collings *et al., "External Stabilization of $Nb_3Sn$ Rutherford Cables - AC losses and contact resistance"*, Advances in Cryogenic Engineering: Proceedings of the International Cryogenic Materials Conference - /CMC, Vol. 48 pp. 1153-1160, May 2002

[55] E.W Collings *et al., "Influence of a Stainless Steel Core on Coupling Loss, ICR and Magnetization of a Nb3Sn Rutherford cable",* IEEE Transactions on Applied Superconductivity, Vol. 18 Issue 2 pp. 1301-1304, June 2008.

[56] E.W Collings *et al.,* "*Effect of Core Width, Placement, and Condition on Calorimetrically measured AC loss and ICR of SS-Cored Nb3Sn Rutherford Cables",* IEEE Transactions on Applied Superconductivity, Vol. 18 Issue 2 pp. 1370-1373, June 2008.